

X-ray spectroscopy of hot white dwarfs

Dissertation
zur Erlangung des Grades eines
Doktors der Naturwissenschaften
der Mathematisch-Naturwissenschaftlichen Fakultät
der Eberhard Karls Universität Tübingen

vorgelegt von

Jens Adamczak

aus Marburg
2010

Selbstverlegt von: J. Adamczak, Melanchthonstrasse 25, 72074 Tübingen
Tag der mündlichen Prüfung: 11. 10. 2010
Dekan: Prof. Dr. W. Rosenstiel
1. Berichterstatter: Prof. Dr. K. Werner
2. Berichterstatterin: Dr. S. Schuh

Erweiterte deutsche Zusammenfassung

Adamczak, Jens

Röntgenspektroskopie heißer weißer Zwerge

Spektroskopische Röntgenbeobachtungen von zwei heißen weißen Zwergen wurden vom *Chandra* Satelliten aufgenommen und ausgewertet. Das erste Objekt ist ein weißer Zwerg der Spektralklasse DA, dessen Atmosphäre fast ausschließlich aus Wasserstoff besteht. Im Gegensatz dazu finden sich in der Atmosphäre des zweiten Objekts, eines PG 1159 Sterns, keine signifikanten Mengen an Wasserstoff. Die Gegensätzlichkeit der beiden Objekte liegt in ihrer unterschiedlichen Entwicklungsgeschichte begründet.

Weißer Zwerge stellen die letzte Stufe der Sternentwicklung von Sternen mit geringer und mittlerer Masse dar ($\lesssim 8\text{--}10M_{\odot}$). Sie bestehen aus einem Kern aus Kohlenstoff und Sauerstoff und darüber liegenden Schalen mit Helium und Wasserstoff. Die große Gravitationskraft dieser Objekte bewirkt ein Absinken der schweren Elemente aus der Atmosphäre, sodass diese praktisch nur aus einem Element besteht. Im Falle der DA Spektralklasse ist dies Wasserstoff, der als leichtestes Element auf allen anderen schwimmt. Ist die Temperatur groß genug ($> 30\,000\text{ K}$), ist der Wasserstoff fast vollständig ionisiert, was eine deutliche Verringerung der Opazität zur Folge hat. Röntgenstrahlung aus heißen, tiefen, photosphärischen Schichten kann von der Oberfläche entweichen und von Röntgensatelliten detektiert werden. Da nur eine geringe Anzahl von heißen weißen Zwergen bei Himmelsdurchmusterungen im Röntgenbereich gefunden wurde, wurde klar, dass die Atmosphären dieser Objekte durch den radiativen Auftrieb von schweren Elementen und die damit verbundene Zunahme der Opazität verunreinigt werden. Dieser Mechanismus hängt stark von der Temperatur ab. Deshalb sind nur wenige DA weiße Zwerge mit Temperaturen oberhalb von $60\,000\text{ K}$ als Röntgenstrahler bekannt. Um Spektren von diesen und vergleichbaren Sterne zu analysieren, werden Modellatmosphären verwendet, die die Häufigkeiten der einzelnen Elemente selbstkonsistent für jeden Tiefenpunkt berechnen. Diese Berechnungen beruhen auf der Annahme, dass sich gravitative und radiative Kräfte in jeder Tiefe im Gleichgewicht befinden. Das Ergebnis ist eine chemische Schichtung, die von zwei Parametern bestimmt wird, der Effektivtemperatur T_{eff} und der Oberflächenschwerebeschleunigung g . Der Gesamtflußverlauf von Spektren von DA weißen Zwergen, die im extremen Ultraviolett (EUV) aufgenommen wurden, kann mit Modellatmosphären, die eine solche Schichtung beschreiben, reproduziert werden. Die Auflösung der vorliegenden EUV Spektren ist jedoch zu gering, um einzelne Spektrallinien zu identifizieren. Deshalb werden zur Bestimmung der Gesamtmetallizität Model-

le mit einer homogenen Verteilung der Elemente in der Atmosphäre verwendet, die ein Häufigkeitsmuster besitzen, das dem des weißen Zwergs G 191-B2B entspricht, für den detaillierte Untersuchungen existieren. Die Metallizität erhält man dann durch Skalieren des spezifischen Musters. Ist die Metallizität des gesuchten Objektes größer als die von G 191-B2B, kann dies zum Beispiel durch Akkretion erklärt werden. Die Gründe für die in einigen Objekten gefundene geringere Metallizität sind derzeit noch ungeklärt und sollen in dieser Arbeit untersucht werden.

Der heiße weiße Zwerg LB 1919 besitzt eine ungewöhnlich geringe Häufigkeit an schweren Elementen. Eine relative Skalierung der Metallizität bezogen auf G 191-B2B führt zu einer Opazität, die zu groß ist, um passende Modellatmosphären mit einer homogenen Verteilung der Elemente zu erzeugen. Geschichtete Modelle, die die Häufigkeiten der vermuteten Elemente selbstkonsistent berechnen scheitern ebenso. Speziell das mit dem *Extreme Ultraviolet Explorer (EUVE)* aufgenommene Spektrum von LB 1919 kann auf diese Weise nicht reproduziert werden. Viele Spektrallinien besonders der hohen Ionisationsstufen von Elementen wie Eisen und Nickel befinden sich im Röntgenwellenlängenbereich und sind der Schlüssel zur Erklärung der ungewöhnlichen Metallarmut. Beobachtungen von einzelnen weißen Zwergen im Röntgenbereich sind selten. Detaillierte Untersuchungen dieser Objekte in diesem Wellenlängenbereich wurden bisher nicht vorgenommen. Deshalb betritt die vorgestellte Analyse in dieser Arbeit Neuland.

Die Untersuchung eines *Chandra* Spektrums von LB 1919 zeigt keine Anzeichen für das Vorhandensein von Fe und Ni in der Atmosphäre dieses Sterns. Zur weiteren Analyse wurden zusätzliche Beobachtungen in anderen Wellenlängenbereichen untersucht. In den LB 1919 Spektren des *Far Ultraviolet Spectroscopic Explorer* wurden die Spektrallinien von verschiedenen Elementen identifiziert und deren Häufigkeiten mit Anpassungen von homogenen Modellen bestimmt. Eine Bestimmung der Temperatur durch Anpassung von Modellatmosphären an die Lyman Wasserstofflinien im Ultraviolet deutet darauf hin, dass LB 1919 um etwa 10 000 K kälter ist als bisher angenommen. Unter der Berücksichtigung nur derjenigen Elemente, die im *FUSE* Bereich identifiziert wurden, wurde die Analyse auf Beobachtungen im EUV Bereich, dem optischen Wellenlängenbereich und ein weiteres Mal dem Röntgenbereich ausgeweitet. Die Ergebnisse, die die homogenen Modelle liefern, werden dabei verglichen mit berechneten geschichteten Atmosphären, die die selben Elemente enthalten, um eine Aussage über die Tauglichkeit beider Arten von Modellen in Bezug auf DA weiße Zwerge machen zu können. Der Verzicht auf nicht identifizierte Elemente wie Fe und Ni ist dabei von entscheidender Bedeutung, um eine gute Reproduktion der Spektren zu erreichen. Diese Elemente fehlen offenbar völlig in der Atmosphäre von LB 1919. Der größere Erfolg der geschichteten Modelle bei der Reproduktion der spektralen Energieverteilung der beobachteten Spektren speziell im EUV Bereich, deutet darauf

hin, dass das Gleichgewicht zwischen gravitativen und radiativen Kräften gegeben ist. Das heißt, dass unerwartete, das Gleichgewicht störende, Prozesse wie Konvektion oder Massenverlust ausgeschlossen werden können und dass der Grund für den Metallmangel von LB 1919 und vergleichbaren Sternen in einem früheren Entwicklungsstadium zu suchen ist. Über diesen Grund kann bisher nur spekuliert werden.

Während die DA weißen Zwerge das Endprodukt einer konventionellen Sternentwicklung darstellen, entstehen die wasserstoffarmen PG 1159 Sterne durch einen späten thermischen Puls, der für die ungewöhnliche chemische Zusammensetzung verantwortlich ist. Dabei wird Material aus dem Inneren des Sterns an die Oberfläche befördert und der restliche Wasserstoff verbrannt oder verdünnt. PG 1159 Sterne sind ebenfalls in der Lage, beobachtbare Röntgenstrahlung zu emittieren. Einige dieser Sterne pulsieren und definieren den GW Virginis (GW Vir) Instabilitätsstreifen im *Hertzsprung-Russell-Diagramm (HRD)*. Die Position der blauen Kante des Streifens ist festgelegt durch ein Pulsator/Nicht-Pulsator Paar von spektroskopischen Zwillingsternen. Die Untersuchung des temperatursensitiven weichen Röntgenbereichs des nicht-pulsierenden Sterns PG 1520+525 ermöglicht es, die Effektivtemperatur mit einer Präzision zu bestimmen, die nicht durch Analyse von Beobachtungen im ultravioletten Bereich allein erreicht werden kann. Das Ergebnis ist insbesondere hilfreich, um Pulsationsmodelle zu verfeinern, die die Position des Instabilitätsstreifens in Abhängigkeit von T_{eff} und $\log g$ voraussagen.

Abstract

Adamczak, Jens

X-ray spectroscopy of hot white dwarfs

X-ray spectra of two hot white dwarfs observed by the *Chandra* satellite have been analyzed. The first is a white dwarf of spectral class DA with an almost pure hydrogen atmosphere. Contrary to that, the atmosphere of the second object, a PG 1159 star, is basically hydrogen free. The reason for the different composition can be found in the differing evolution of these objects.

White dwarfs are the final stage of evolution of low and intermediate mass stars ($\lesssim 8-10M_{\odot}$). They consist of a carbon/oxygen core with surrounding layers of helium and hydrogen. Their atmospheres are characterized by a quasi mono-elemental composition that results from gravitational settling of heavy elements. In the case of the DA spectral class the lightest element, hydrogen, floats on top of the others. In hot DAs the temperature is high enough ($>30\,000\text{ K}$) to almost completely ionize the hydrogen, thus, the opacity in the atmosphere is strongly reduced. Soft X-ray radiation coming from hot, deep, photospheric layers can be emitted from these objects and it was detected in the X-ray survey of the *ROSAT* telescope. The small number of detected WDs, however, lead to the conclusion that the atmospheres can be polluted by the opacity of heavy elements by radiative levitation. The strong dependence of this mechanism on the effective temperature results in only a few detected DA white dwarfs with temperatures above $60\,000\text{ K}$ in the X-ray range. In order to analyze the spectra of these stars model atmospheres are used that calculate the abundances of the elements self-consistently at each depth of the atmosphere. These models are based on the assumption of an equilibrium of radiative and gravitational forces at each depth point. The result is a chemical stratification that is defined by only two free parameters, the effective temperature T_{eff} and the surface gravity g . The spectral energy distribution (SED) of extreme ultraviolet (EUV) spectra of most DA white dwarfs can be described by such a stratification. The resolution of available EUV spectra, however, is too low to identify individual lines. In order to determine the metallicity of an object, therefore, models assuming a homogeneous mixture of elements in the atmosphere are used with an abundance pattern similar to that of the well studied white dwarf G 191-B2B. The actual metallicity of the object is then derived from scaling this specific pattern. An observed metallicity larger than predicted can for example be explained by accretion. The reasons for the lower metallicities in some objects are still unclear and are investigated in this thesis.

The hot DA white dwarf LB 1919 shows an untypically low abundance of heavy

elements. A metallicity scaled relative to the one of G 191-B2B results in a too high opacity to reproduce the *Extreme Ultraviolet Explorer (EUVE)* spectrum of LB 1919 with a homogeneously mixed atmosphere and the stratified models fail as well. Many spectral lines of high ionization stages of the heavy elements iron and nickel are located in the X-ray wavelength range. These lines are the key to the explanation of the unusual metal poorness. X-ray observations of single white dwarfs are scarce and no detailed investigations of these objects exist. Therefore, the analysis presented in this work is breaking new ground.

The investigated *Chandra* spectrum of LB 1919 shows no evidence for the occurrence of Fe and Ni in the atmosphere of this star. For a further analysis additional observations in different wavelength ranges were considered. Using spectra of the *Far Ultraviolet Spectroscopic Explorer (FUSE)* various elements were identified and their abundances were determined with models that assume a homogeneously mixture of elements in the atmosphere. A temperature determination with model fits on the Lyman hydrogen lines in the ultraviolet shows that LB 1919 is around 10 000 K cooler than assumed. Considering only those elements that have been identified in the *FUSE* spectra of LB 1919 the analysis was extended to the EUV, the optical, and again the soft X-ray range. The results from the investigation with the homogeneously mixed models are always compared to calculations with stratified atmospheres with the same elements in order to make a statement about the suitability of both kinds of models for these type of stars. The restriction to the few elements that were found in the UV spectra turns out to be the crucial point in order to achieve a good fit quality. Obviously, some heavy elements like Fe and Ni are completely missing in the atmosphere of LB 1919. The greater success of the stratified model atmospheres in reproducing the SED of the observed spectra, especially in the EUV range, indicates that the equilibrium between gravitational and radiative forces is in good order. Therefore, unexpected and disturbing mechanisms like convection or mass-loss can be excluded. This suggests that the cause for the metal deficiency of LB 1919 and comparable stars has to be found in an earlier evolutionary state and is subject of speculation.

Contrary to the DA white dwarfs, the PG 1159 stars undergo an unconventional development. Their evolution is characterized by a late thermal pulse that defines their unusual chemical composition. This pulse causes matter to be dredged up from the interior and results in a burning or dilution of the residual hydrogen. PG 1159 stars are also capable of emitting detectable amounts of X-ray radiation. Some of these stars pulsate and define the GW Virginis (GW Vir) instability strip in the *Hertzsprung Russell Diagram (HRD)*. The position of the blue edge of this strip can be constrained by a pulsator/non-pulsator pair of spectroscopically very similar stars. The investigation of the temperature sensitive soft X-ray range of the non-pulsating star PG 1520+525 makes it possible to determine the effective tem-

perature with a precision that cannot be achieved by the analysis of observations in the UV alone. The result is especially helpful for the refinement of pulsational models that predict the position of the instability strip in dependence of T_{eff} and $\log g$.

Contents

1	Introduction	1
1.1	Outline	2
2	White dwarfs	5
2.1	Stellar evolution	5
2.2	Characteristics	7
2.3	Radiative Levitation	9
2.4	Metal poor white dwarfs	12
2.4.1	Mass loss	14
2.4.2	Accretion	15
2.4.3	Convection	16
2.4.4	Rotation	17
2.5	LB 1919	17
2.6	PG 1159 stars	18
2.7	PG 1520+525	20
3	X-ray observations	23
3.1	Basic problem	23
3.2	<i>ROSAT</i>	24
3.3	<i>EUVE</i>	26
3.4	<i>Chandra</i>	27
4	Model atmospheres	29
4.1	Radiative transfer	29
4.2	Atomic data	33
4.3	Stratified atmospheres	33

5	Tests and implementations	35
5.1	Frequency grid	35
5.2	Convergence criterion	36
5.3	New atomic data	37
5.3.1	Iron	37
5.3.2	Nickel	39
5.4	NGRT code	39
5.4.1	Bound-free transitions	40
5.4.2	Bound-bound transitions	44
5.5	Model atoms	47
5.6	Germanium model atom	49
6	Analysis of LB 1919 and GD 246	53
6.1	Previous investigations (LB 1919)	53
6.2	<i>Chandra</i> observation (LB 1919)	54
6.3	Comparison with observation (LB 1919)	55
6.3.1	Homogeneous models	55
6.3.2	Stratified models	57
6.4	Previous investigations (GD 246)	58
6.5	Comparison with observation (GD 246)	59
6.5.1	Homogeneous models	59
6.5.2	Stratified models	61
6.6	<i>FUSE</i> analysis (LB 1919)	62
6.6.1	Parameter checkup	62
6.6.2	Elements and abundances	63
6.7	<i>FUSE</i> analysis (GD 246)	67
6.7.1	Parameter checkup	67
6.7.2	Elements and abundances	68
6.8	Optical constraint	73
6.9	<i>EUVE</i> analysis	74
6.9.1	LB 1919	74
6.9.2	GD 246	79
6.9.3	Column density determination	86
6.10	<i>Chandra</i> analysis (LB 1919)	91
6.10.1	Homogeneous models	91
6.10.2	Stratified models	95
6.11	<i>Chandra</i> analysis GD 246	95
6.11.1	Homogeneous models	95
6.11.2	Stratified models	97
6.12	Final remarks	98

7	Analysis of PG 1520+525	101
7.1	Previous investigations	101
7.2	<i>Chandra</i> analysis	102
8	Discussion	111
8.1	LB 1919	111
8.2	PG 1520+525	116
	Bibliography	119
A	<i>Chandra</i> plots	125
B	<i>FUSE</i> plots	139
C	<i>UVES</i> plots	155
D	Model atoms plots	159
	Acknowledgements	161
	Curriculum vitae	163
	Lebenslauf	165

List of Figures

2.1	Evolution of solar-mass star in HRD	6
2.2	White dwarf interior	10
2.3	Equilibrium distributions of N	12
2.4	Born again scenario	19
5.1	New Kurucz iron lines	38
5.2	New Kurucz iron lines in spectrum	39
5.3	New Kurucz lines in spectrum. Detailed.	40
5.4	Abundances modified bf-transition	42
5.5	Abundances oxygen, different bf-transitions	43
5.6	Modified bb- and bf-transitions, occupation numbers Fe	45
5.7	Effect of modified bb transition on flux	46
5.8	Effect of large number of lines on abundances	47
5.9	Grotrian diagram Ge IV	49
5.10	Ge IV in LTE and NLTE	51
6.1	Model flux processing	55
6.2	LB1919 iron abundances	56
6.3	LB1919 homogeneous and stratified models	57
6.4	GD246 iron lines	60
6.5	GD246 homogeneous and stratified models	61
6.6	LB1919 Lyman line fit	63
6.7	LB1919 carbon triplet	64
6.8	LB1919 phosphorus and silicon lines	65
6.9	LB1919 sulfur and silicon lines	67
6.10	GD 246 phosphorus, silicon and sulfur lines	69
6.11	GD 246 Ge IV line	70
6.12	Balmer fit for LB 1919 and GD 246	73
6.13	LB 1919 failure to match <i>EUVE</i> spectrum	75
6.14	LB 1919 <i>EUVE</i> plot, varying T_{eff} and $\log g$	77
6.15	LB 1919 <i>EUVE</i> plot without oxygen	78
6.16	LB 1919 <i>FUSE</i> , <i>EUVE</i> modified diffusion abundances	79
6.17	GD 246 <i>EUVE</i> plot, varying $\log g$ and included elements	81

6.18	GD246 model spectrum with extreme line blanketing	82
6.19	GD246 Effect of reduced opacity for formal solution	83
6.20	GD246: Effect of additional opacity by nitrogen	85
6.21	GD246 Deviation plot	87
6.22	GD246 <i>EUVE</i> best fit models	88
6.23	LB1919 Deviation plot	89
6.24	LB1919 <i>EUVE</i> best fit models	90
6.25	Occupation Probability Formalism	92
6.26	LB 1919 <i>Chandra</i> spectrum Si abundance	93
6.27	LB 1919 <i>Chandra</i> best fit models	94
6.28	GD246 comparison <i>Chandra</i> and <i>EUVE</i> spectrum	96
6.29	GD 246 <i>Chandra</i> best fit models	97
7.1	PG 1520+525 column density determination	103
7.2	PG 1520+525 T_{eff} overview	104
7.3	PG 1520+525 lines	105
7.4	PG 1520+525 Mg abundance	106
7.5	PG 1520+525 Mg resonances	107
7.6	PG 1520+525 instability strip	109
8.1	LB 1919 evolutionary tracks	113
8.2	LB 1919 position in Galaxy	114
A.1	<i>Chandra</i> models LB 1919 homogeneous	126
A.2	<i>Chandra</i> models LB 1919 stratified	127
A.3	<i>Chandra</i> models LB 1919 $\log g = 8.5$	128
A.4	<i>Chandra</i> models GD 246 homogeneous	129
A.5	<i>Chandra</i> models GD 246 stratified	130
A.6	GD 246 <i>Chandra</i> iron abundance	131
A.7	GD 246 <i>Chandra</i> model different $\log g$	132
A.8	<i>Chandra</i> models LB 1919 elements homogeneous	133
A.9	<i>Chandra</i> models LB 1919 elements stratified	134
A.10	<i>Chandra</i> models GD 246 elements homogeneous	135
A.11	<i>Chandra</i> models GD 246 elements stratified	136
A.12	<i>Chandra</i> models GD 246 elements homogeneous	137
A.13	<i>Chandra</i> models GD 246 elements stratified	138
B.1	LB 1919 C III triplet homogeneous	140
B.2	LB 1919 C III triplet stratified	141
B.3	GD 246 C III triplet homogeneous/stratified	142
B.4	LB 1919 O VI line homogeneous/stratified	143
B.5	GD 246 O VI line homogeneous/stratified	144
B.6	LB 1919 P V and Si IV line homogeneous/stratified	145
B.7	GD 246 P V and Si IV line homogeneous/stratified	146

B.8	LB 1919 Si III triplet homogeneous/stratified	147
B.9	LB 1919 S IV triplet homogeneous/stratified	148
B.10	LB 1919 S VI doublet homogeneous/stratified	149
B.11	GD 246 S VI doublet homogeneous/stratified	150
B.12	GD 246 Ge IV line homogeneous/stratified	151
B.13	LB1919 C III triplet detail	152
B.14	LB1919 Si IV line detail	152
B.15	GD 246 Si IV line detail	152
B.16	LB1919 P V line detail	153
B.17	GD246 P V line detail	153
B.18	GD 246 P V line detail	153
B.19	LB 1919 S IV triplet detail	154
B.20	GD 246 S VI line detail	154
B.21	GD 246 Ge IV line detail	154
C.1	UVES plot of LB 1919	156
C.2	UVES plot of GD 246	157
D.1	Line profiles big model atoms	160
D.2	Abundances with small model atoms	160

List of Tables

5.1	Model atoms	48
5.2	Ge IV model atom	50
6.1	GD 246 Parameter	59
6.2	Abundances of elements LB 1919 and GD 246	72
7.1	PG 1520+525 model atoms	102
7.2	Parameter PG 1520+525	108

CHAPTER 1

Introduction

Stars are born in star forming regions out of dust and interstellar matter and spend most of their lives by exhausting their main energy source, hydrogen. Depending on their mass, their further development is characterized by mass-loss, thermal pulses and flashes, contractions and explosions. The properties and the specific evolution of the stars may vary but they all have in common that they will end in a final configuration as stellar remnants.

One of these final configurations is that of a white dwarf. White dwarfs mark the final stage in the life of stars of low or intermediate mass. They consist of a carbon/oxygen core with layers of helium and hydrogen around it. With no more energy gained by fusion processes in their core, they cool into faintness in the course of time. Even though, nowadays, the physics of white dwarf stars can be described quite accurately, there are still interesting questions to answer. What is the reason for a metal deficiency in some of the hot white dwarfs? Are unexpected mechanisms like convection or mass-loss working in their atmospheres? How suitable are stratified model atmospheres in reproducing the observed flux, and what constrains the pulsations in some of the hydrogen deficient PG 1159 stars?

The investigation of white dwarf spectra is the key to the answers of these and other questions and the aim of this thesis. The dealing with the late stages of stellar evolution means to learn something about the life of the stars in general. This can be achieved by comparing the final result of the development of the star with the predictions from evolutionary theories. In this context the class of the metal poor white dwarfs is investigated closely in the following chapters. For that purpose LB 1919 is taken, a hot white dwarf of spectral class DA (see chapter 2) with a bright appearance in the X-ray wavelength range. X-ray observations of single white dwarfs are rare and almost no investigations exist, thus, this work represents pioneering work in this field of astronomical research. The concentration on the X-ray regime is necessary because many spectral lines, especially of high ionization stages of iron and nickel, are located exclusively at these wavelengths. The investigation of these lines is crucial in order to find a reason for the metal poor

composition of LB 1919 and other comparable stars that seem to contradict theoretical predictions. Spectra observed in other wavelength ranges are considered and analyzed as well in order to obtain additional information and constraints on the photospheric properties of LB 1919.

In addition to that, another class of objects is investigated. The X-ray spectrum of the hot non-pulsating PG 1159 star PG 1520+525 is analyzed and the results are compared to the properties of a pulsating spectroscopic twin star in order to constrain the occurrence of the pulsations in dependence of effective temperature and surface gravity.

1.1 Outline

The structure of this work is the following. In the next chapter the theoretical background of white dwarf stars is explained. Their properties and evolution are described and mechanisms like diffusion and radiative levitation, which occur in their atmospheres, are discussed. In particular, the already mentioned class of metal poor white dwarfs and the hydrogen deficient class of PG 1159 stars are introduced and related to the scientific context of this thesis. The third chapter presents the observational methods for spectroscopic X-ray observations that are the foundation of all further analysis. The focus lies on the characteristics of white dwarf X-ray and Extreme Ultraviolet (EUV) observations with the *Chandra* and *EUVE* satellites. The actual instrumental setup of the specific telescopes is mentioned briefly and reduced to the essential informations. The next chapter (4) is dedicated to the model atmospheres that are used for the investigation of the observed spectra. They can be divided into atmospheres with a homogeneous mixture of elements and stratified models with different abundances at each depth of the atmosphere. The underlying assumptions are presented and reconsidered. Chapter 5 deals with test calculations and implementations in the model atmosphere code, with the aim to refine the following analysis of the program stars.

The actual analysis of the metal poor white dwarf LB 1919 is described in detail in chapter 6. The chapter itself is divided into different sections to account for the different wavelength ranges that were considered. Besides *Chandra* X-ray observations, spectra in the EUV, UV, and optical range were analyzed in order to obtain a consistent picture of the star's behavior. In chapter 7 the PG 1159 star PG 1520+525 is analyzed in the wider context of a constraint for pulsational models. For this purpose a detailed effective temperature determination considering the temperature sensitive soft X-ray *Chandra* range is performed. Details about this specific topic can be found in chapter 2 and chapter 7 itself. The results of the analysis of LB 1919 and PG 1520+525 are discussed in the last chapter (8) in

which the final conclusions are drawn.

CHAPTER 2

White dwarfs

The first star classified as a white dwarf (WD) was 40 Eridani B, a component of the triple star system 40 Eridani. The name white dwarf refers to the high effective temperature that causes the white color of the object and its small radius. It soon turned out that white dwarfs mark the final stage of the life of a star and that their composition and physical properties depend strongly on their former development and determine their further evolution. Some of the physical properties of a star can be deduced by its position in the *Hertzsprung-Russell diagram (HRD)*, in which the luminosity of the star is plotted versus its effective temperature. The different luminosities observed for stars with identical temperatures can be attributed to their diverse surface areas. Since the different phases in the life of a star are strongly characterized by processes of expansion and contraction, stellar evolution can be described in a demonstrative way with the aid of the HRD. A detailed overview describing the physics of white dwarf stars can be found in Koester & Chanmugam (1990). In the following, only some information about white dwarfs that is important for the framework of this research project is presented.

2.1 *Stellar evolution*

Stars form out of interstellar matter (ISM). At the onset of star formation a homogeneous cloud of gas and dust becomes gravitationally unstable and collapses once its mass exceeds the critical Jeans mass (Kippenhahn & Weigert 1994). When the temperature in the interior is high enough to burn the lightest element, hydrogen, the star moves to the main sequence (MS), i.e. a sequence of chemically homogeneous models with different masses and central hydrogen burning in the HRD. The development prior to the main sequence (pre-main sequence, PMS, evolution, Palla 2001) will not be discussed here. For a star of $1 M_{\odot}$ the following steps take place in its evolution. After the star has fused all hydrogen to helium in its inner region, hydrogen is still burning in a shell around the core. The shift of the hydrogen burning zone towards the outer regions of the star causes an expansion of its enve-

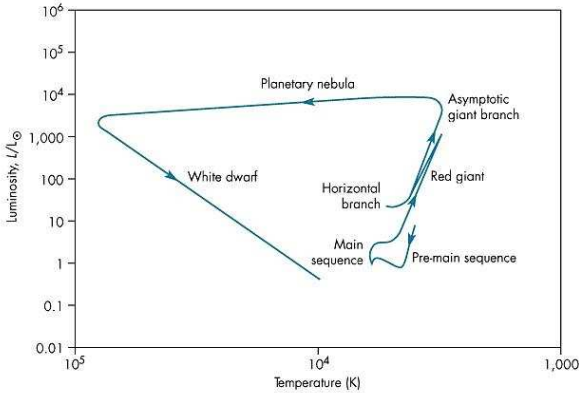


Figure 2.1: Evolution of a solar-mass star in the HRD. The final stage of its evolution is the white dwarf cooling track. Picture taken from Zijlstra (2002).

lope. The surface of the star increases and the luminosity becomes higher. The star leaves the main sequence in the *HRD* and enters the so-called giant branch. The core contracts until the temperature in the central region is high enough to start the burning of helium to carbon in the triple-alpha process, a moment often referred to as *helium flash*. As carbon is accumulating in the core, oxygen can be produced by collisions between carbon and helium nuclei (Richmond 2007). Once helium is burned, the stellar envelope expands again leading the star to the asymptotic giant branch (AGB) in the HRD.

For stars with high masses, i.e. larger than $8\text{--}10 M_{\odot}$ ¹, a similar evolution can then take place repeatedly. The burning in the interior will consume all of the available fuel leading to another core contraction and the ignition of the next element. The whole procedure causes the star to enter and leave the AGB multiple times, producing heavier elements up to iron. The process then stops, because the fusion of iron requires more energy than is released.

Stars of low and intermediate mass, i.e. up to a mass of $\sim 8 M_{\odot}$, can not produce elements heavier than carbon and oxygen through fusion of elements in the core. Any more complex element found in these stars has either already been present in the matter, out of which the star was born, or is produced in the *s*-process in the AGB phase. This process is a slow neutron-capture reaction with a subsequent radioactive decay of the unstable neutron-rich isotopes (Boothroyd 2006). Even

¹One solar mass $1M_{\odot} = 1,989 \cdot 10^{30}$ kg

though a small amount of heavier elements might be present in these stars, they consist mainly out of a carbon/oxygen core and shells of helium and hydrogen around it. In this composition they face the final stage of their evolution.

With no more radiation pressure to counteract the gravitational forces, the core collapses until the electrons in the core matter are so close that they produce degeneracy pressure, which is strong enough to stop further contraction. This pressure is a result of the quantum mechanical Pauli principle. Two fermions, in this case electrons, are not allowed to occupy the same quantum state simultaneously. As the stars contract, they expel their envelope and lose a certain fraction of their mass. The amount of mass loss of an AGB star increases in principle with its metallicity (Groenewegen et al. 1995). However, an exact determination is difficult, since the description of the responsible mechanisms is complicated and the mass loss rate of a star cannot for the moment be calculated from first principles (Olofsson 2001). The remnant of the star in some cases illuminates the ejected envelope and becomes a central star of a planetary nebula.

At the beginning of this phase the stars produce their energy output by burning hydrogen or helium in a shell and move in the *HRD* to higher temperatures while keeping a constant luminosity. When no more hydrogen can be burned, their luminosity begins to decrease. Because they lost most of their H envelope, those stars basically consist of an exhausted core of degenerate carbon and oxygen (Kwok 2005). Since energy sources are no longer available, the star enters the white dwarf cooling track in the *HRD* and usually remains there for the rest of its life.

For stars with larger initial masses, i.e. larger than $8\text{--}10 M_{\odot}$, the post AGB evolution is different. Because of the big mass, the gravitational forces are strong enough to compress the core matter further, once the energy production via fusion ceases. This results in either a neutron star (van Kerkwijk 2004), or in a black hole (Czerny & Nikolajuk 2009).

2.2 Characteristics

As described above, the evolution of white dwarf stars is nowadays quite well understood. The understanding is good enough to make them a useful tool in different areas of astronomical research. White dwarfs are for instance used to determine the age of the Galaxy (Wood 1992). There are mainly four reasons that make them excellent chronometers. They are common in the Universe, they are a homogeneous class of objects, they are physically relatively simple, and finally, their further evolution is a basic cooling process. In the following these four reasons will be discussed briefly.

White dwarfs are common in the universe. Since white dwarfs mark the end-point of stars with a wide range of mass ($0.7\text{--}8 M_{\odot}$), it is believed that around 97 percent of all stars born in the Galaxy end up as white dwarfs (Fontaine et al. 2001). As they are typical representatives, studying white dwarfs can therefore yield information about life and evolution of the bulk of stars.

White dwarfs are a homogeneous class of objects. Due to their evolution, white dwarfs exhibit a very narrow distribution of mass. The two defining equations for the structure of a white dwarf with assumed zero temperature are the equation of hydrostatic equilibrium,

$$\frac{dP}{dr} = -\frac{Gm\rho}{r^2}, \quad (2.1)$$

and the equation of mass conservation,

$$\frac{dm}{dr} = 4\pi r^2 \rho. \quad (2.2)$$

Here, m is the mass inside a sphere with the radius r , which is 0 at the center of the star. Together with the knowledge of the equation of state, i.e. the dependence of the pressure P on the density ρ and the chemical composition μ_e , $P = P(\rho, \mu_e)$, this set of equations describes the interior of the star adequately, as shown by (Chandrasekhar 1939). Accordingly, the equations can be reformulated into a second-order differential equation for a dimensionless function with two parameters. These parameters are the chemical composition μ_e and the central density ρ_c . Out of the numerical solution for a given μ_e , a mass radius relation of the star is derived (Chandrasekhar 1935). In the limit $\rho_c \rightarrow \infty$, the radius of the star becomes zero and the Chandrasekhar limiting mass for the object is derived as $5.826/\mu_e^2 M_{\odot}$, depending only on the chemical composition. Any object with a slightly higher mass would collapse into a singularity. Refinements including a more realistic equation of state (Salpeter 1961) as well as corrections at finite temperature (Kovetz & Shaviv 1970), do not affect the basic principles. Thus, the masses of white dwarfs are defined very clearly with an observed average around $0.6 M_{\odot}$ with 60 percent falling in an interval around $0.1 M_{\odot}$ (see for example Weidemann & Koester 1984 for white dwarfs with a pure hydrogen atmosphere).

White dwarfs are physically relatively simple. They possess high surface gravities and slow rotation rates. Even though magnetic white dwarfs are known with field strengths ranging up to 10^9 Gauss, the majority of single white dwarfs has low magnetic fields (Wickramasinghe & Ferrario 2000). Compared to other stars, white dwarfs can therefore be very well described by basic physics.

The further evolution of white dwarfs is a basic cooling problem. After the burning of elements in the interior of a white dwarf stops, the star starts losing

energy E continuously.

$$\Delta E = \Delta U_{\text{th}} + \Delta E_{\text{grav}} \quad (2.3)$$

This corresponds to a change in gravitational energy E_{grav} and a contraction of the star. Half of the energy released is radiated away and supplies the luminosity the other half increases the inner energy of the white dwarf. Due to the small radius of the star and the scaling of the gravitational energy with $\Delta R/R$, this change in radius is rather unobservable. The thermal energy U_{th} , and with it the temperature of the star, decreases. Thus, the behavior of a white dwarf described by equation 2.3 is often referred to as cooling. It should be noted however that while the thermal energy of the ions decreases, the energy of the electrons and with it the internal energy of the the star is increasing as in every other star (Koester & Chanmugam 1990). A radius of a typical white dwarf is roughly about the size of the Earth ($\sim 10000\text{km}$), but it is much denser with surface gravities around $\sim 10^8 \text{ cm s}^{-2}$. Neglecting the gravitational energy release and the emission of neutrinos leads then to a description of the cooling as the further evolution of the white dwarf (Mestel 1952, Mestel & Ruderman 1967). The cooling time of a white dwarf can be deduced following Koester & Chanmugam (1990) as

$$t = \frac{10^8}{A} \left(\frac{M}{M_{\odot}} \right)^{0.609} \left(\frac{L}{L_{\odot}} \right)^{-0.609} \text{ yr.} \quad (2.4)$$

With the atomic mass number A , mass of the star M and its luminosity L . Thus, the future life of a white dwarf does only depend on its mass and luminosity.

To achieve accurate result for age measurements of stellar populations, the exact knowledge of WD parameters and their cooling sequences is necessary. The parameters depend at least slightly on the metallicity in the white dwarf photosphere, since effective temperature and surface gravity are usually determined by adjusting models to the Balmer lines in observed spectra. The required profiles of these hydrogen lines depends on metal opacities. Given that the metallicity is in turn a function of the white dwarf parameters (see section 2.4), the understanding of the physical processes constraining the metal abundances is crucial.

2.3 Radiative Levitation

In general, white dwarfs can be separated into two spectroscopic sequences: the DA and non-DA spectral class. The class of DA WDs is characterized by strong hydrogen lines and no visible helium components. The non-DA WDs are dominated by helium. Absorption features of He II and He I define the spectral classes

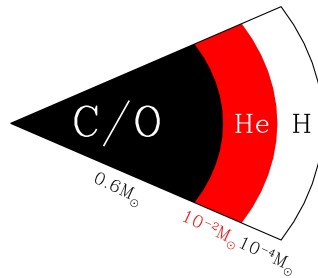


Figure 2.2: The interior of a white dwarf star. The degenerate core of carbon and oxygen is surrounded by shells of helium and hydrogen. Picture taken from Napiwotzki (2010).

of the DO and DB white dwarfs (McCook & Sion 1999). WDs with combined properties are often denoted as DAO and DAB stars respectively. In the case of the DA white dwarfs the atmosphere exhibits a quasi mono-elemental composition. Hydrogen as the lightest element is floating on top of the others, thus no He lines can be detected in the spectra. The reason for those pure atmospheres are diffusion processes initiated by the high surface gravity of the star. Figure 2.2 shows a cut through such a white dwarf, where the helium layer is clearly separated from the overlying hydrogen due to the diffusion processes.

The hydrogen in the atmospheres of hot DAs with temperatures $>30\,000\text{ K}$ is almost completely ionized and the opacity is strongly reduced. After the detection of soft X-rays with the *Astronomical Netherlands Satellite (ANS)* coming from Sirius (Mewe et al. 1975a,b), it was suggested that hot white dwarfs are capable of emitting detectable amounts of thermal X-ray radiation originating from the deep, hot, photospheric layers (Shipman 1976). Model atmosphere calculations of hydrogen-rich white dwarfs revealed that the X-ray luminosity² of these stars is indeed comparable to those of most observed discrete soft X-ray sources (Wesemael 1978). The *ROSAT* satellite did the first all-sky survey with imaging X-ray and extreme ultraviolet (EUV) telescopes and made a detailed study of selected X-ray and EUV sources possible. However, compared to the estimated amount of over 5 000 X-ray emitting hot white dwarfs, the small number of less than 200, which were actually found, was remarkable. The emission of X-rays in these hot objects was recognized to be the exception and not the expected rule. Obviously, the atmospheres of most of the hot white dwarfs must be enriched with additional absorbers, which block the emergent flux (Kahn et al. 1984). The *Extreme UI-*

²The X-ray luminosity is derived from the radius R of the star and by integrating the Eddington flux H_ν over the X-ray frequency range, $L_x = 4\pi R^2 \cdot \int_{X\text{-ray}} H_\nu d\nu$.

traviolet Explorer EUVE, launched in 1992, confirmed this result and revealed that heavy elements are the origin of the missing opacity. The enormously large number of absorption lines of elements like iron and nickel can therefore provide an opacity that is large enough to determine strongly the observed EUV *spectral energy distribution (SED)* of the hot white dwarfs.

The diffusion time scale in the atmosphere is always much shorter than the evolutionary time scale (Fontaine & Michaud 1979). Therefore, permanent physical processes must define the content of the absorber in the photosphere and the SED of the star. Vauclair et al. (1979) described for the first time mechanisms capable of polluting a pure hydrogen atmosphere with ions of heavier elements. They found that these elements can generally absorb enough momentum from the radiation field to counteract the gravitational settling and that traces of carbon, nitrogen, and oxygen, as well as silicon, can levitate through bound-bound absorption at the surface of hot WDs (Morvan et al. 1986; Vauclair 1987). The exact amount of specific elements at the different depths of the atmosphere and the degree of pollution depend therefore on the so-called radiative levitation. Elements can be kept in outer layers of the atmosphere by a strong radiation pressure. Because of the shortness of the diffusion time scale the arrangement of the elements in the envelope of a white dwarf can be treated as an equilibrium condition in the modeling (Vauclair 1989). In the following years the picture of radiative levitation in hot white dwarf atmospheres was refined.

Chayer et al. (1989) pointed out that the idea of a strict equilibrium between radiative forces and gravitational settling may be insufficient. Therefore, the observational pattern of heavy elements in hot DAs can not be explained by a simple application of the radiative support theory only and other mechanisms must be involved. Further motivation for radiative force calculations came from the discovery of iron absorption lines in hot DAs. In this context calculations of Fontaine & Wesemael (1991) demonstrated for the first time that radiative levitation can indeed account for detectable traces of iron in hot DA atmospheres. A systematic approach to describe the abundances was presented with the so-called equilibrium radiative levitation theory (Chayer et al. 1995a). In this concept, the abundances of trace elements in the envelope are calculated by equating the local effective gravity with the derived radiative acceleration at a certain depth of the envelope. The envelope consists of pure H or He depending on the regarded type of white dwarf. The result is an equilibrium distribution of an element in terms of depth. Integrating the distribution over depth corresponds to the total supply of the regarded element, which is maintained against settling. The shape of this distribution is therefore characteristic for each element. Figure 2.3 shows such a distribution for the trace element nitrogen. The depth is measured in terms of the logarithm of the mass fraction M above the point of interest r , $\log(1 - M(r)/M(R) = \log(\Delta M/M)$,

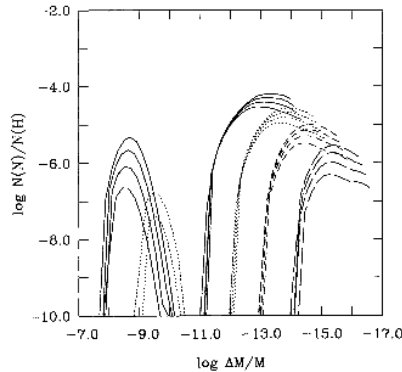


Figure 2.3: Calculated equilibrium distributions of N taken from Chayer et al. (1995a). Shown is the dependence of the abundance of N, levitating in the envelope of a DA white dwarf model, on the surface gravity. For the gravities $\log g = 7.0$ (solid curve), $\log g = 7.5$ (dotted curve) and $\log g = 8.0$ (dashed curve), four temperatures were calculated. These are from top to bottom: $T_{\text{eff}} = 65\,000\text{ K}$, $60\,000\text{ K}$, $55\,000\text{ K}$, and $50\,000\text{ K}$.

the bigger the mass fraction, the lower the depth. The abundances are given as the logarithm of the number of the trace element relative to hydrogen. Based on the described method, improved radiative levitation calculations were presented with a focus on reported or potential presence of traces of astrophysically important heavy elements in the atmospheres of hot white dwarfs (Chayer et al. 1995b).

Additionally to the elements treated so far, the importance of the identification of nickel was discussed (Werner & Dreizler 1994). The reason was the consideration that relative abundances of various pollutants may provide information as to the roles of radiative levitation and possible competing processes (Chayer et al. 1994). With their large number of transitions, the iron group elements can by all means provide substantial EUV opacity and therefore play a key role in understanding the EUV spectra.

2.4 Metal poor white dwarfs

What can be learned from radiative levitation calculation is that metal abundances increase with increasing effective temperature. Only a few DA white dwarfs with $T_{\text{eff}} > 60\,000\text{ K}$ possess atmospheres with a low enough opacity to emit radiation coming from deeper layers. Therefore, just a small amount of these stars can be

detected at all, which explains the result of the *ROSAT* survey.

In order to predict the vertical stratification of the metal abundances in the DA atmospheres, self-consistent models have been developed (Dreizler 1999b). Contrary to the equilibrium radiative levitation theory, these models are not restricted to approximations that are formally valid only in *local thermodynamic equilibrium* (*LTE*) and large optical depths. In these self-consistent models the abundances of the elements at each depth are calculated under consideration of the atmospheric structure and its interaction with the elements. Compared to homogenous models, in the stratified models the surface abundances of the elements are no longer free parameters. They are calculated on physical grounds (see chapter 4). Thus, only the effective temperature and the surface gravity of the star have to be adjusted in order to reproduce the observed spectra.

In general, a good agreement between calculated models and observed spectra is achieved, even though in some cases discrepancies can be found (Dreizler 1999a). Only in some cases a solution for the deviations between models and observations of the DA white dwarfs can be found. If the observed abundances of the elements in the atmosphere are larger than modeled, processes like accretion or accretion from interstellar/circumstellar matter are possible explanations. For observed photospheric abundances that are smaller than computed, however, up to now no suitable explanation is available. This is quite remarkable, since the photospheric composition of a WD is strongly determined by its previous development and the metal poor white dwarfs do not fit in any accepted evolution scenario.

Examples of hot DAs found with *ROSAT* with a metal free atmosphere or at least very low abundances found are HZ 43, MCT 0027-6341, and LB 1919. These stars do not show any significant absorption features in the EUV and X-ray wavelength range, even though they possess high effective temperatures ($T_{\text{eff}} = 49\,000\text{ K}$, $64\,000\text{ K}$, and $69\,000\text{ K}$). These objects yield information for the understanding of the class of the metal poor hot DA white dwarfs. They were observed in the extreme ultraviolet region and analyzed, but as for all objects observed by *EUVE*, the resolution of their spectra was too low to identify lines of individual species.

The metallicity of DAs, which are too faint to be analyzed directly, can be specified by being compared to the metallicity of the bright, metal rich, and well studied white dwarf G 191-B2B (Wolff et al. 1998a). The spectra of the other DA white dwarfs are then reproduced by scaling the specific abundance pattern of G 191-B2B. In the case of the metal poor white dwarfs, however, the spectra can not be described by models that possess a homogeneous mixture of elements with an abundance scaled relative to G 191-B2B in the atmosphere, nor can they be described by a stratified model, which includes radiative levitation. The failure to match the *EUVE* spectra with both kinds of models might indicate an abundance pattern, which is not similar to that of G 191-B2B. Another possibility is a stratification,

which deviates from the one predicted by radiative levitation. This would mean that the equilibrium between gravitational forces and radiative pressure in the atmosphere is currently disturbed. There are in general four mechanisms possible to interfere. These are mass loss, accretion, convection and rotational mixing.

2.4.1 Mass loss

Because spectra of DA white dwarf stars are characterized by no visible He lines, the He abundances of hot DAs is sometimes determined assuming that this element provides a huge amount of the opacity in the EUV spectral range. The flux deficiencies in that wavelength range, typical for DAs with $T_{\text{eff}} > 40\,000$ K, can be explained either by the presence of heavy elements in the atmosphere or by a stratified atmosphere consisting of an outer hydrogen layer on top of a helium distribution (Vennes 1992; Koester 1989).

A stratified atmosphere as derived by radiative levitation calculations however can not explain the presence of He in DAO white dwarfs with $T_{\text{eff}} > 60\,000$ K, i.e. stars much hotter than most DA stars. The predicted abundances are too low by at least a factor of ten (Vennes et al. 1988). A possible explanation lies in the evolution of the stars. Thus, most WDs enter the cooling sequence as He-rich objects with only minor traces of hydrogen. In the course of time, gravitational settling sets in and causes the H to float up resulting in a stratified atmosphere.

A closer look on the He line profiles of DAOs white dwarfs, however, suggests that their atmospheres can more likely be regarded to be chemically homogeneous (Bergeron et al. 1994). The change in the helium abundance in hot white dwarfs and along with it the transformation from He rich stars into DA or DAO stars is therefore not solely caused by gravitational settling effects.

Unglaub & Bues (1994) pointed out the influence of diffusion and mass-loss on the helium abundance in hot white dwarfs and analyzed the effect of mass loss on a stratified atmosphere. They investigated the processes responsible for the transformation of a He-rich WD with $T_{\text{eff}} = 80\,000$ K and $\log g = 7.0$ into a hydrogen-rich one by diffusion. For an original number ratio of H/He = 10^{-4} , or larger, in an outer layer of $10^{-7} M_{\star}^3$, in the absence of mass loss the star would transform into a DAO WD with an ultrathin H-layer in not more than 10 000 yr. After 100 000 yr the surface composition would be very similar to the one predicted by diffusion calculations for a thick hydrogen layer. The transformation back into a DO WD depends then on the possible mass loss of the star. If a DA or DAO WD with a stratified atmosphere is losing mass for example in the form of a weak wind of $\dot{M} = 10^{-16} M_{\star} \text{yr}^{-1}$, it will transform back into a DO within 5 000 yr.

Thus, a DO WD with a hydrogen number fraction of 10^{-4} , or lower, will not

³Here, M_{\star} denotes the mass of the modeled star

transform into a DAO or DA star if at least a weak wind is present. Consequently, for stars with a mass-loss rate above a critical limit of $\dot{M} = 10^{-16} M_{\star} \text{yr}^{-1}$, a stratified atmosphere originating from ordinary diffusion processes cannot exist. The exact value of the mass-loss rate is therefore of importance in order to determine if a star can maintain a stable stratified atmosphere.

An estimation of the mass-loss rate can be obtained by the formula of Blöcker (1995)

$$\frac{\dot{M}}{M_{\odot}} = 1.29 \cdot 10^{-15} \frac{L}{L_{\odot}}^{1.86}, \quad (2.5)$$

which gives a result in yr^{-1} . This relation was derived for the progenitor of the white dwarfs, i.e. the central stars of planetary nebulae. The mass loss in this phase strongly constrains the properties of the WD and as seen in equation 2.5 it depends solely on the luminosity L of the star. An additional increase in the mass-loss rate can be expected by a higher metallicity according to Abbott (1982), nevertheless, a possible perturbation of the equilibrium between radiative and gravitational forces is more likely, the higher the luminosity of the object is.

2.4.2 Accretion

White dwarfs are capable of accreting mass on their way through the ISM (Koester 1976; Wesemael 1979; Michaud & Fontaine 1979). The ISM itself can be divided into different phases. One phase is the so-called hot phase, i.e. a local bubble of hot coronal gas in the *local interstellar medium LISM* (Cox & Reynolds 1987). Another phase consists of the warm ISM and cold clouds. The existence of DOs with cool He atmospheres on the order of $T_{\text{eff}} \sim 50000 \text{K}$ requires a very low rate of accretion of the ISM material onto the surface of the white dwarf (MacDonald & Vennes 1991). It is so low that it has to be many orders of magnitude less than even the smallest accretion rates expected from the hot phase of the interstellar medium. A possible explanation is a WD stellar wind responsible for preventing hydrogen from being accreted and for polluting the He atmosphere. Further evidence for the existence of such winds was provided by studies of metals in hot white dwarfs, such as the discrepancies between predicted and observed carbon abundances for Feige 24 and PG 1034+001 (Chayer et al. 1987). The observation of accreted heavy elements over time in the atmosphere of white dwarfs is in principle possible, if the downward diffusion is counteracted by a suitable process like levitation (Bruhweiler & Kondo 1983). For a theoretical description of accretion mechanisms MacDonald (1992) developed two dynamical models for the shock structure formed by an interaction between the WD wind and the flow of interstellar material. These can be used to find limits on properties of winds that

are capable of preventing the accretion from the ISM. These models are in principle a generalization of solar wind interaction models with local ISM and include effects of gravity. They are based on models for supersonic motion of the Sun through ISM. Some of these models are more appropriate to the warm and cold ISM phases (Baranov et al. 1970), some are adapted to the hot phase, e.g. the spherically symmetric model of Parker (1961). The results show that mass loss rates as low as $10^{-21} M_{\odot} \text{yr}^{-1}$ can already prevent accretion from the hot phase of the ISM. For the cold phase, the necessary rate is higher ($3 \cdot 10^{-18} M_{\odot} \text{yr}^{-1}$).

2.4.3 Convection

The occurrence of convection in the atmosphere of a star is related to the conditions of the matter in it. Assuming an atmosphere in radiative equilibrium the question to ask is, whether an element of material, when displaced from its original position, experiences forces that tend to move it further in the direction of its displacement (Mihalas 1970). In that case, the atmosphere is unstable against mass motion and convection will occur. The basic criterion for the stability against convection traces back to Karl Schwarzschild. Under the condition that the movement of the element is slow, it remains in pressure equilibrium with its surroundings. Furthermore, the process has to be regarded as adiabatic, i.e. the element does not exchange energy with its surroundings. Instability originates, if the change in density of the element $(\Delta\rho)_E$, due to the lower pressure at the new position, is less than the density gradient of the radiative surroundings $(\Delta\rho)_R$. The element then experiences a buoyancy force and continues to rise. The criterion can be written as

$$(\Delta\rho)_E = \left(\frac{d\rho}{dr}\right)_A \Delta r < (\Delta\rho)_R = \left(\frac{d\rho}{dr}\right)_R \Delta r, \quad (2.6)$$

where the index A denotes the adiabatic nature of the element. This can be expressed in terms of temperature T and pressure p in the region,

$$\nabla_R \equiv \left(\frac{d \ln T}{d \ln p}\right)_R > \frac{\Gamma - 1}{\Gamma} = \left(\frac{d \ln T}{d \ln p}\right)_A \equiv \nabla_A. \quad (2.7)$$

Since the gas in a stellar atmosphere in general consists out of many different elements and ions, $\nabla_A = (\Gamma - 1)/\Gamma$ cannot be described by the heat capacity ratio for a perfect monoatomic gas $\gamma = (C_p/C_v) = 5/3$. Indeed some effects can lower the value for ∇_A in a normal gas and affect the critical value for ∇_R . Thus, while for a perfect monoatomic gas ∇_A amounts to 0.4, in an area with pure radiation pressure and $\Gamma = 4/3$ it is as low as $\nabla_A = 0.25$. For conditions, where hydrogen is ionizing, important in stellar atmospheres, Γ is around 1.1 and $\nabla_A = 0.1$.

The results suggest that convection can be expected to occur in zones, where hydrogen is ionizing.

2.4.4 Rotation

The rotation of a star would lead to a mixing of the atmosphere. The rotation of a WD is a remnant of the initial angular momentum of the progenitor star, processed by several stages of stellar evolution (Kawaler 2003). Rotation can have a significant influence on the structure of a WD. It was for instances shown that a rotation of about 2 000 km/s of a WD could in general increase the maximum mass of a WD by about 5% (Roxburgh 1965). However, the majority of the observed and investigated white dwarfs is compatible with no rotation or with an at least very small one (Heber et al. 1997; Koester et al. 1999).

2.5 LB 1919

LB 1919, also known as WD 1056+516, RE J1059+512, RX J1059.2+5124, EUVE J1059+51.4, and RBS 927, is a representative of the class of the metal poor DA WDs and the X-ray brightest star known in this class. Furthermore, it is the hottest of 90 DAs found in the *EUVE* all sky survey (Vennes et al. 1997). It is located in the milky way at coordinates RA: 10 59 16.43 and Dec: 51 24 43.2 (J2000). Despite all previous investigations (see section 6.1 for more information), the chemical composition of LB 1919 is as yet unknown. As for all metal poor white dwarfs, the *EUVE* spectrum of LB 1919 could not be described by scaled abundances. The stratified models that are based on the mechanism of radiative levitation, did not provide a satisfying result either.

The intermediate aim of the analysis following in chapter 6 is to find out, if the metals in the atmosphere of LB 1919 are in general stratified or homogeneously mixed. A reasonable answer to this question depends on the elements that can be found and their abundances. For many atoms, especially iron group elements, an abundance determination can only be reached with observations in the UV and X-ray range, where most of the important lines are located. An analysis of the strengths of iron and nickel and other lines in a *Chandra* spectrum with appropriate model atmospheres should give then strong hints about the composition of the atmosphere. The reason is the fact that different parts of the spectrum of a star originate from different depths in the atmosphere. Shorter wavelengths can therefore expose deeper atmospheric layers. This is the key feature of the Wien tail of the spectrum, i.e. the shape of the spectrum at substantially short wavelengths, which lies in the EUV and X-ray wavelength range. As a consequence, lines of different ionization stages of the same elements can probe different temperature layers. The *Chandra* spectra are determined by both the metal abundances and their depth dependence. Thus, an analysis of the exact composition could answer the open questions for the metal poor WDs.

If the atmosphere of the star is stratified, then it is in equilibrium between diffusion and radiative levitation and no other processes are currently at work. The low observed metallicity would then probably be a consequence of processes attributed to an earlier evolutionary state. This could for example be a wind, which is driven by radiation and acts selectively on metals.

If the elements in the atmosphere are on the other hand homogeneously mixed, then one of the previously described processes must be involved. Regarding the properties of LB 1919 as a white dwarf, these processes are however not likely to occur. To prevent a destruction of a stratification of the elements in LB 1919 a critical mass loss should not be exceeded (see subsection 2.4.1). The mass loss itself depends on the luminosity L , which in turn depends on T_{eff} and the radius R of the star via $L = 4\pi R^2 \sigma T_{\text{eff}}^4$. Assuming an earth-like radius for the white dwarf, the effective temperature turns out to be the determining factor. For hot white dwarfs the luminosity exceeds the solar one leading to a higher mass loss rate. For the expected temperature of LB 1919, in the range between 50–70 kK, the mass loss will drop gradually below the critical limit ($\dot{M}_{70000} \sim 10^{-15} M_{\odot} \text{yr}^{-1}$, $\dot{M}_{50000} \sim 10^{-16} M_{\odot} \text{yr}^{-1}$). These mass loss rates are on the other hand sufficiently high to prevent accretion of interstellar material onto the surface since only a mass loss of $> 3 \cdot 10^{-18} M_{\odot} \text{yr}^{-1}$ is necessary (see subsection 2.4.2). A strong rotation of LB 1919 is very unlikely according to subsection 2.4.4 and the analysis in chapter 6 will show if the spectra exhibit any hints on rotational broadening of the spectral lines. Convection occurs in hydrogen ionization zones. For the atmosphere of LB 1919 with its high effective temperature, however, hydrogen is already almost completely ionized, so that no such disturbance should be expected. In fact, convection in DA white dwarf atmospheres becomes only relevant at temperatures around 11–13 kK (Bergeron et al. 1995; Montgomery & Kupka 2004).

Since all four processes are unlikely, the occurrence of one of them in LB 1919 would be a contradiction to the expectations from theory. The specific abundances of the elements that can be found would provide further hints to determine which mechanisms are actually involved. A lack of iron, for example, would indicate a depletion by the radiatively driven winds. In addition to the determination of surface compositions in the metal poor WDs and the acting processes in their atmospheres, the results of the analysis will therefore also test fundamental astrophysical theories of accretion and mass loss.

2.6 PG 1159 stars

Even though strictly speaking not all of them are white dwarfs, PG 1159 stars mark the transition between the post-AGB evolution and the WD cooling sequence and

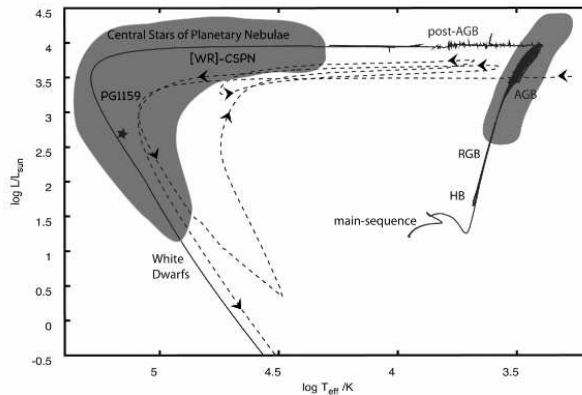


Figure 2.4: Evolutionary track of a $2 M_{\odot}$ star for a normal post-AGB evolution (solid line) and a born-again evolution (dashed line). The second one, triggered by a VLTP is shifted for clarity. Picture taken from Werner & Herwig (2006).

shall be introduced in the following.

PG 1159 stars, named after the prototype PG 1159-035, are hydrogen deficient objects with a wide range of T_{eff} and $\log g$. The spectra of PG 1159 stars show a broad absorption trough caused by the He II line at 4686 \AA and the neighboring C IV lines. In hot PG 1159 stars also lines of O VI and Ne VII can be found. To describe the different characteristics of the PG 1159 stars, three spectral subclasses have been defined (Werner 1992). Stars of spectral subclass A (absorption) show pure absorptions in the trough. Subclass E (emission) is defined by emission cores in He II 4686 \AA , C IV 4659 \AA , and C IV 4647 \AA . The last subclass comprises the central stars of planetary nebulae with low gravity, hence, narrower absorption wings, and are labeled lgE (low gravity emission). They show emission in the He II 4686 \AA , C IV 4659 \AA , but the C IV 4647 \AA line is in absorption.

The characteristic surface composition of the PG 1159 stars is strongly coupled to their evolution. The hydrogen deficiency is most likely caused by a late helium-shell flash. A star in the post-AGB or white dwarf phase can re-ignite the helium burning in a shell. The star would then transform back towards lower effective temperatures and is *reborn* as an AGB star. An evolutionary track for a star with a mass of $2 M_{\odot}$ undergoing a born-again evolution is seen in figure 2.4. The star is re-entering the AGB twice, leading to a total of three AGB phases. During the flash that causes the return to the AGB, the envelope of the star is dredged up and mixed. As a result, hydrogen is burned and the surface composition changes. It

becomes similar to that of the previous intershell layer. This region between the H- and He-burning shells of the AGB star is rich in He, C, and O and determines the characteristics of the PG 1159 stars. This means that PG 1159 atmospheres are almost completely made up of intershell matter thus providing a way to study its abundances directly and gain information about the physical processes leading to the specific composition (Werner & Herwig 2006). The abundances of the elements in the atmospheres of the PG 1159 stars vary much and can be explained by a different number of thermal pulses during the AGB phase. The relative He/C/O abundances can be found in the ranges He=0.30–0.85, C=0.13–0.60, and O=0.02–0.20 (mass fraction, see Werner et al. 2008b).

The helium-shell flash can occur at different times on either the horizontal part of the post-AGB track or late during the post-AGB evolution. It is then referred to as a late thermal pulse (LTP) or as a very late thermal pulse (VLTP). In the first case the born-again evolution follows a single loop and hydrogen becomes deficient by a dredge-up mixing. In the second case, the star follows a double loop as shown in figure 2.4 and hydrogen is ingested and burned in a surface layer.

Some PG 1159 stars are non-radial high-order gravity mode (*g*-mode) pulsators. They are known as GW Virginis (GW Vir) variables. The mechanism that drives the pulsation is the κ effect of carbon and oxygen (Starrfield et al. 1983, 1984). A recent overview over the pulsating PG 1159 stars currently known can be found in Quirion (2009). The pulsating stars define a certain region in the HRD - the so called GW Vir instability strip. The C/O driving mechanism works at temperatures around 100 000 K in layers very close to the surface of the star. A low helium abundance and almost no hydrogen are requirements for the operation of the mechanism. However, small trace amounts of hydrogen (up to 3 % of mass fraction) do not affect the stability of the *g*-modes (Saio 1996). The determined effective temperatures and gravities of the GW Vir stars suggest a narrow mass range around $0.6 M_{\odot}$. The cool end of the instability strip corresponds to the transition from the PG 1159 stars to the DO white dwarfs, thus a gravitational settling of the elements heavier than helium (Dreizler 1998).

Evolutionary models predict the location of the edges of the instability strip (Quirion et al. 2004; Gautschy et al. 2005). However, further empirical investigations are necessary in order to determine the exact position of the edge and constrain the models.

2.7 PG 1520+525

The PG 1159 star PG 1520+525 (WD 1520+525) is a non-pulsator and is located close to the pulsating PG 1159–035 in the $g - T_{\text{eff}}$ diagram. Together they define

the blue edge of the instability strip. To confirm the position of the strip, the temperature of PG 1520+525 has to be determined precisely. The temperature of PG 1159-035 has already been sufficiently constrained to $T_{\text{eff}} = 140\,000 \pm 5\,000\text{ K}$ (Jahn et al. 2007). A verification that PG 1520+525 is indeed hotter, however, is still missing. Optical investigations of its temperature indicate that this is most likely the case (Dreizler & Heber 1998). For a more precise determination the analysis of X-ray data is used (cf. chapter 7), since a strong sensitivity of the soft X-ray flux on T_{eff} variations is predicted.

CHAPTER 3

X-ray observations

The awareness that the deep photospheric layers of hot white dwarfs can emit detectable amounts of X-ray radiation directed the observational attention to the high energy wavelength range around $1 \text{ \AA} < \lambda < 100 \text{ \AA}$. The observations of this specific wavelength range have always posed great challenges on the instrumental setup. Since the Earth's atmosphere is opaque for X-ray radiation due to photoabsorption by the ions N_2 , O_2 , and O , observations could only be realized by moving the instruments into space. The scientific advantages brought about by the observation of the X-ray regime, however, outweigh the problems by far. Many elements in the atmospheres of hot white dwarfs have no strong lines in ultraviolet or optical wavelengths and can only be detected in the EUV or X-ray regions.

Most of the X-ray emitting white dwarfs are of spectral type DA but also a few non-DA and H-deficient central stars of planetary nebulae (PG 1159 stars) have been found. The thermal radiation of those objects can be detected in the soft X-ray wavelength range ($30 \text{ \AA} < \lambda < 100 \text{ \AA}$) and the EUV region ($100 \text{ \AA} < \lambda < 700 \text{ \AA}$). The transition between these regions is not exactly defined and the wavelengths observed by different instruments like *EUVE* or *Chandra* overlap and ideally should be considered simultaneously. Depending on the different scientific objectives and technological possibilities, the developed X-ray instruments for the observation of white dwarfs are based on various concepts. The observations of the first X-ray space observatories *Einstein* and *EXOSAT* were mostly photometric. For the high resolution spectroscopy necessary to identify white dwarf spectral features, however, X-ray telescopes like *Chandra* and *XMM Newton* are used.

3.1 Basic problem

In the first half of the last century it was believed that observations in the soft X-ray and EUV regime were impossible to achieve, since the electron binding energies of most elements are in the same range as the energies of the photons in the EUV band (100–1 000 \AA). As a result, not only the Earth's atmosphere with an ab-

sorption depth of $\approx 130\text{km}$ is impenetrable for radiation in that wavelength range (Barstow & Holberg 2003). The absorption by interstellar gas causes a problem that cannot be resolved by moving the observatories into space. The mean free path τ of a photon in the ISM is mainly determined by the neutral hydrogen density $N(\text{H})$ and the hydrogen absorption cross-section σ_{H} , $\tau = 1/(N(\text{H})\sigma_{\text{H}})$. With the knowledge of the hydrogen density of that time, Aller (1959) concluded that the neutral hydrogen in the solar system and in the interstellar space will cause serious problems and that there is almost no hope of getting any observations of the Lyman lines in emission-line rich stars. After a re-examination of the interstellar medium with more recent values of the relevant cross-sections and abundances with respect to soft X-ray and EUV radiation, a significant transparency in the EUV range along at least some lines of sight was found (Cruddace et al. 1974). In the following it was confirmed that the ISM does not exhibit a uniform distribution as assumed previously and that the much lower values for the hydrogen density in some regions makes it possible to see soft X-ray and EUV sources in distances of a few hundred parsecs. However, the number of detectable sources decreases at longer wavelengths.

3.2 ROSAT

The primary scientific objective of the *Röntgensatellit* (ROSAT) launched in 1990 was to perform the first all-sky survey with an imaging X-ray telescope leading to a sensitivity improvement by several orders of magnitude compared with previous surveys (Aschenbach et al. 1981). It was a three-axis stabilized satellite designed for both scanning and pointed observations (Barstow & Holberg 2003). For the detection of X-ray sources in the sky survey an 80 cm Wolter Type I Mirror assembly and a position-sensitive proportional counter (PSPC) were used (Hasinger 1985). In addition to that, a Wide Field Camera (WFC) was installed to image the sky in four wavebands by use of selected filters, two of which were exclusively used for pointed observations (Barstow 1989). The WFC consisted of a grazing incidence telescope built of a set of three Wolter-Schwarzschild Type I gold-coated aluminium mirrors and a microchannel plate (MCP) in the focal plane.

The ability to observe hot white dwarfs was quantified by convolving model WD spectra with the instrument response for the different bandpass. The three bands for the survey are the PSPC band ($44\text{\AA} < \lambda < 80\text{\AA}$) and the two bands of the WFC ($60\text{\AA} < \lambda < 140\text{\AA}$ for the C/Lexan/B band and $112\text{\AA} < \lambda < 200\text{\AA}$ for the Be/Lexan band). Furthermore, a minimum detectable temperature limit can be estimated as a function of absorbing column density. To predict the expected number of white dwarfs found in the survey, knowledge of their space density and EUV and X-ray

luminosity has to be considered. According to Fleming et al. (1986) white dwarfs are homogeneously distributed in the Galactic disk with a scale height of 250 pc. Their luminosity depends on the stellar temperature. Taking the relative number of hot white dwarfs, this leads to a number of 5500 DA white dwarfs expected to be detected in the PSPC band and approximately half the number (2200) in the C/Lexan/B bandpass of the WFC (Barstow 1989).

The results of the *ROSAT* observations showed a ratio of $\approx 1:1$ instead of the expected 2:1. This can not be explained by an interstellar absorption effect. A higher interstellar absorption would decrease the number of WD found with the WFC relative to the number found in the PSPC (Barstow et al. 1992). The solution can be found in the homogeneous WD atmosphere models and the ratio of He and H of 10^{-4} assumed by Barstow (1989) for the estimation. The low number of PSPC detections was an evidence for the presence of additional opacity in the DA white dwarf atmospheres (Barstow et al. 1993, cf. also section 2.3).

The overall number of hot white dwarfs found in the *ROSAT* all sky survey amounts to 175. They can be divided into DA white dwarfs (161), PG 1159 stars (8), DO (3), and DAO (3) stars (Fleming et al. 1996). The relative number of X-ray emitting white dwarfs with respect to the overall WD population is as low as 10%. In addition to the improved observations of numerous known white dwarfs, 69 previously unknown white dwarfs were discovered in the *ROSAT* WFC survey (Mason et al. 1995). Hard X-ray emission ($\lambda < 25 \text{ \AA}$) can be found for 6 single white dwarfs (O'Dwyer et al. 2003; Chu et al. 2004b and Chu et al. 2004a). The nature of this emission, however, is only speculative. Recent investigations indicate that the idea of a photospheric origin (Werner et al. 2008a) cannot be maintained (Werner priv. comm.). An overview of the stellar parameters of the observed white dwarfs can be found in Marsh et al. (1997a,b).

In comparison to the DA white dwarfs the helium-rich DO white dwarfs have to be much hotter to emit soft X-ray radiation. The additional opacity of carbon and oxygen in PG 1159 stars is increasing the temperature, which is necessary for a detection, further. Consequently, only 8 objects were detected in the *ROSAT* PSPC survey. Amongst others, these are the GW Vir variable RX J2117.1+3412 and the non-pulsator PG 1520+525. The first one is a very hot ($T_{\text{eff}} = 170000 \text{ K}$) central star of a planetary nebula and was used for asteroseismology (Córscico et al. 2007). The second one, PG 1520+525, constrains the position of the GW Vir instability strip together with the pulsating PG 1159 prototype PG 1159-035 (cf. subsection 2.7).

3.3 EUVE

Two years after the successful launch of *ROSAT*, the *Extreme Ultraviolet Explorer* (*EUVE*) was placed into space. The primary purpose was to survey the sky for extreme ultraviolet radiation of astronomical sources (Bowyer & Malina 1991). A total of 5 instruments was available for scientific research, four imaging systems and a three-channel EUV spectrometer.

In the first phase of the mission the imaging instruments were used to accomplish a complete sky survey. Contrary to *ROSAT* the observations were concentrated on the longer wavelengths. The all-sky survey was therefore conveyed in four bands 70–180 Å, 170–250 Å, 400–600 Å, and 500–700 Å (Miller 1997). The telescopes used were three single grazing incidence mirrors, two of a Wolter-Schwarzschild Type I design and one of Wolter-Schwarzschild Type II. The detectors were of two-dimensional microchannel plate type. After the first 6 months of the survey a pointed observation period with the spectrometer followed. The spectrometer covers the wavelength range of 70–760 Å and is divided into three channels: short (SW) 70–190 Å, medium (MW) 140–380 Å, and long (LW) 280–760 Å.

Of the 734 sources in the second *EUVE* source catalog (Bowyer et al. 1996) 105 were identified as hot white dwarfs. As for *ROSAT* the majority of the white dwarfs found with *EUVE* are of spectral type DA, while only a few DO white dwarfs were detected. The analysis of white dwarf *EUVE* spectra demonstrated clearly the important role of metals in explaining the EUV opacity problem (Dupuis 2002). The spectral resolving power of the *EUVE* spectrometer is $\lambda/\Delta\lambda \approx 200$ and therefore too low to identify spectral lines or absorption edges of individual species. Especially the blanketing of numerous Fe and Ni lines with unknown wavelengths cannot be resolved. However, many of the observed white dwarf spectra have a characteristic shape caused by heavy element opacities.

Thanks to the *EUVE* observations, a better understanding concerning the surface composition of hot white dwarfs in general could be achieved. The results of *EUVE* observations made clear that the model for a DA atmosphere consisting of a thin hydrogen layer floating on top of an underlying helium mantle cannot be the last word on the subject (Fontaine & Wesemael 1997). None of the *EUVE* spectra clearly showed the characteristics that are typical for a stratified H/He atmosphere. In cases where He I and He II edges were detected interstellar absorption provided a suitable explanation (Dupuis et al. 1995). The *EUVE* white dwarf population shows a mass distribution in accordance with the *ROSAT* results. A mass spectrum with a narrow peak around $0.56 M_{\odot}$ and a high number of ultra-massive white dwarfs with $M \geq 1.1 M_{\odot}$, which are possibly examples of O/Ne/Mg core white dwarfs (Vennes et al. 1997).

3.4 *Chandra*

The *Chandra* X-ray Observatory was built by the *National Aeronautics and Space Agency (NASA)* and launched in 1999 (Tomlin 1999). It reached orbit in July and began observing in October. The scientific objectives include deep sky surveys and a detailed spectroscopy of plasmas. It contains a Wolter-Type I high-resolution telescope. It has a high-resolution X-ray mirror system with less than 0.5 arcsec spatial resolution (Trümper & Hasinger 2008) and two imaging detector systems. It is furthermore equipped with two different insertable gratings, the low energy transmission grating (LETG) and the high energy transmission grating (HETG) to allow high resolution spectroscopy. The transmission gratings used in various satellite missions consist of a grating ring filled with small grating elements. The LETG was designed and fabricated by the Space Research Institute of the Netherlands (SRON) and the Max-Planck-Institut für extraterrestrische Physik (MPE in Garching, Germany). It is optimized for a wavelength range between 6 and 154 Å. The highest resolving power ($\Delta\lambda/\lambda$) exceeds 2000 at 150 Å. The primary readout for the LETG spectrum is done by the spectroscopy detector of the High-Resolution Camera (HRC) (Weisskopf et al. 2000). The HETG consists of two sets of gratings, the medium energy grating (MEG) and the high energy grating (HEG). It is optimized for medium and high energies, corresponding to wavelengths around 2.5–31 Å (MEG) and 1.2–15.5 Å (HEG).

Among the diverse science targets of *Chandra* are supernova ejecta, X-ray emissions of galaxies, active galactic nuclei (AGN) and quasars (Murray 2001). However, not many *Chandra* observations of isolated hot white dwarfs exist. Only a handful of LETG spectra of these objects were investigated at all. Two of the detected white dwarfs could already be matched by a pure hydrogen model atmospheres in the course of the *EXOSAT* observations. These are HZ 43 and Sirius B (Paerels et al. 1988; Heise et al. 1988). In contrast to the predictions from radiative levitation theory (cf. section 2.3), the atmospheres of these stars are metal free despite their hot temperatures ($T_{\text{eff}} \cong 51\,000\text{K}$ in the case of HZ 43, Beuermann et al. 2007). The spectrum of the hot DA LB 1919 is likewise metal poor. Since LB 1919 is the X-ray brightest star known in the class of the hot metal poor DA white dwarfs, it is predestined for a closer investigation (see chapter 6).

In the LETG *Chandra* spectrum of GD 246 for the first time individual spectral lines of iron could be identified in a soft X-ray spectrum of a DA white dwarf star (Vennes & Dupuis 2002). This case demonstrates clearly the advantage of the superior spectral resolution of *Chandra* compared to *EUVE*. Since GD 246 shows the influence of metal opacities on the flux in the *Chandra* wavelength range and possesses stellar parameters comparable to LB 1919, it is an ideal candidate for a comparison (see chapter 6).

Model atmospheres

The improvement in stellar atmosphere calculations over the last three decades provides nowadays the possibility to analyze spectra containing a large number of elements and line transitions. The construction of a stellar model atmosphere with its restrictions and assumptions about the relevant physical processes was described in numerous publications, for instance the basic treatment of the model-atmosphere problem in Mihalas (1982) or a more recent review of additional improvements in Hubeny et al. (2003). This chapter, therefore, only illustrates the important characteristics relevant for the analysis of the program stars in chapter 6. The following remarks hold for a plane parallel atmosphere in radiative, hydrostatic and statistical equilibrium. The justification of these simplifications in the context of the analysis of LB 1919 will be accounted for.

4.1 Radiative transfer

The emergent spectrum of a star is defined by the photons reaching the surface. On its way through the gas forming the atmosphere, a beam of the radiation field can interact with the matter in different ways resulting in an amplification or weakening of the beam's intensity, I . Thus, the equation of radiative transfer can be written as a dependence of opacity κ_ν and emissivity η_ν caused by the elements in the atmosphere along the way ds ,

$$\frac{dI_\nu}{ds} = -\kappa_\nu I_\nu + \eta_\nu. \quad (4.1)$$

The ratio of absorption and emission processes is described by the source function $S_\nu = \eta_\nu/\kappa_\nu$. The opacity for an atom with a lower state l and an upper state u is given by the cross-section σ of the transitions between the states and the level population n , $\kappa_{lu}(\nu) = \sigma_{lu}(\nu)n_l$. The cross-section includes a quantum mechanical correction term, the so-called oscillator strength, that marks the difference to the classical treatment. It can be regarded as an indicator of the line strength and

is important for the calculation of synthetic line profiles (cf. section 5.6). The formal solution of equation 4.1 gives the intensity in an optical depth τ_1 ¹ of the atmosphere. It can be calculated by

$$I(\tau_1, \mu, \nu) = I(\tau_2, \mu, \nu) \exp(-(\tau_2 - \tau_1)/\mu) + \mu^{-1} \int_{\tau_1}^{\tau_2} S_\nu(t) \exp(-(t - \tau_1)\mu) dt, \quad (4.2)$$

where the angle θ of the beam relative to the local outward normal is included as $\mu = 1/\cos\theta$. The integration limit τ_2 has to be adjusted with respect to the regarded problem. For a consideration of incoming radiation, i.e. $-1 \leq \mu \leq 0$, τ_2 is set to 0 together with a boundary condition that takes into account that the intensity vanishes at the surface $I(\tau_1 = 0, \mu, \nu) \equiv 0$. The more important outgoing radiation ($\mu \geq 0$) is analogously obtained by adjusting $\tau_2 = \infty$ with the boundary $\lim_{\tau \rightarrow \infty} I(\tau_1, \mu, \nu) \exp(-\tau_1/\mu) = 0$. The essential expression for the emergent intensity that is seen by an external observer at optical depth $\tau = 0$ can be derived in a similar way,

$$I(0, \mu, \nu) = \int_0^{\infty} S_\nu(t) \exp(-t/\mu) dt / \mu. \quad (4.3)$$

The source function depends on the opacity and the emissivity, hence on the abundances and the occupation numbers of atoms, ions, and electrons in the atmosphere. They in turn depend on the radiation field and the intensities in each optical depth. Therefore, a solution can in general only be found numerically. A solution approach used in the *PRO2* code of the *Tübingen Model Atmosphere Package TMAP* (Werner et al. 2010) is the Accelerated lambda iteration (Werner & Husfeld 1985).

Introducing the mean intensity $J_\nu = 1/2 \int_{-1}^1 d\mu I_\nu$, equation 4.2 can be expressed by means of an operator Λ_ν as

$$J_\nu = \Lambda_\nu S_\nu. \quad (4.4)$$

Splitting the operator in an exact Λ and approximate part Λ^* (Cannon 1973), equation 4.4 can be solved iteratively (Werner 1986)

$$J_\nu^{(i)} = \Lambda_\nu^* S_\nu^{(i)} + (\Lambda_\nu - \Lambda_\nu^*) S_\nu^{(i-1)}, \quad (4.5)$$

¹ $d\tau = -\kappa_\nu ds$

together with the constraint equations that guarantee for every iteration step i the radiative, hydrostatic, and statistical equilibrium conditions mentioned above. In fact, equation 4.5 can be incorporated in the constraint equations reducing the set of independent variables. The choice of the approximate lambda operator is arbitrary and does not influence the outcome of the procedure.

If a star is in radiative equilibrium as assumed in the calculations the energy absorbed and the energy emitted must be equal at all points in the atmosphere.

$$\int_0^{\infty} \kappa_{\nu}(S_{\nu} - J_{\nu})d\nu = 0 \quad (4.6)$$

The radiative equilibrium defines the temperature T at each depth of the atmosphere (Werner et al. 2003). It can be enforced by adjusting the temperature stratification, for instance by using the Unsöld-Lucy temperature correction (Lucy 1964, see also section 5.2). However, an atmosphere can only be regarded to be in radiative equilibrium, if the energy is transported predominantly by radiation, i.e. if convection does not play a major role. Following the Schwarzschild criterion for convection to occur, as described in subsection 2.4.3, in an atmosphere with almost complete ionization of hydrogen, convection can be ruled out. Consequently for a hot white dwarf like LB 1919 the assumption of radiative equilibrium is justified.

A star can in some cases be regarded to be in hydrostatic equilibrium. If so, the distribution of the static gas pressure dP/dm balances the gravitational force g (Mihalas 1982). The total pressure P consists of gas, radiation, and turbulent pressure. Therefore the equation of statistical equilibrium can be written as

$$\frac{d}{dm} \left(NkT + \frac{4\pi}{c} \int_0^{\infty} f_{\nu} J_{\nu} d\nu + \frac{1}{2} \rho v_{\text{turb}}^2 \right) = g, \quad (4.7)$$

with the turbulent velocity v_{turb} , the number density of particles N , and the variable Eddington factor f_{ν} . The presumption of hydrostatic equilibrium is valid only for static atmospheres. In the case of a moving atmosphere, significant winds or mass-loss, the computational techniques have to be adjusted (Hauschildt & Baron 1999). Winds driven by radiation depend on the surface gravity and the luminosity, hence, the effective temperature of the emitting object. The hotter a star is, the more likely they are to develop. The estimation of mass-loss for a compact hot object ($60000 \text{ K} < T_{\text{eff}} < 80000 \text{ K}$, $\log g \sim 7$) like LB 1919 reveal mass-loss rates that drop below 10^{-16} , a critical limit for the disturbance of the atmosphere (see Unglaub & Bues 1998 and subsection 2.4.1 for details). The atmospheric structure is not affected by such small wind components, making it reasonable to assume hydrostatic equilibrium.

The micro processes that cause transitions between two atomic states are described by the equations of statistical equilibrium. A system is in *local thermodynamical equilibrium (LTE)* if the equilibrium relations of statistical mechanics and thermodynamics at local values of temperature and density can be applied. In that case the distribution of the occupation numbers for the excited states in an atom can be given by the Saha-Boltzmann distribution. It includes the partition function

$$U_{jk}(T) \equiv \sum_i g_{ijk} \exp(-\chi_{ijk}/kT), \quad (4.8)$$

which has to be computed for each excited level i of ionization stage j of chemical species k . For elements with an only partially known term structure, approximations have to be made for the excitation energy χ_{ijk} or for the statistical weight g_{ijk} .

For a stellar atmosphere the simplification of LTE leads in many cases to unsatisfactory results, since the occupation numbers in the outer layers of the atmosphere are mainly determined by radiative rates. The state of the material in these regions is therefore not coupled to local conditions like temperature and density but depends on the non-local information that is contained in the radiation field. How much the occupation numbers deviate from a pure LTE condition can be expressed by the departure coefficients. They describe the difference between the actual population of the level and the population that would occur in local thermodynamic equilibrium at the same temperature and particle densities. The occupation numbers of the particles in the more realistic non-LTE atmosphere can be calculated using the rate equations, which describe the transitions between the atomic states in a precise way. In an equilibrium situation the rates P from state i to j and from state j to i are equal

$$n_i \sum_{j \neq i} P_{ij} - \sum_{j \neq i} n_j P_{ji} = 0. \quad (4.9)$$

The n_x denote the number density of atomic level x . The rates include radiative and collisional transitions, thus $P_{ij} = R_{ij} + C_{ij}$. The rates for every ionization stage and all chemical species define the grand rate matrix \mathbf{A} . The occupation numbers of all NLTE levels can be comprised in a vector $\mathbf{n} = (n_1, \dots, n_{NL})$, where NL denotes the number of NLTE levels per ion. They can then be calculated under assistance of the grand rate matrix considering charge conservation via $\mathbf{A}\mathbf{n}=\mathbf{b}$, with the inhomogeneity vector \mathbf{b} (Werner & Dreizler 1999).

4.2 Atomic data

The atomic data used in the calculations is compiled in the form of model atoms for each regarded element (cf. sections 5.5 and 5.6). For hydrogen with its manageable number of line transitions cross-sections can be calculated for each level individually, for example by using the photon cross-section for ionization by Seaton (1958). Other simple species can be treated in a similar way (Werner 1988). For the complex iron group elements, i.e. Ca to Zn with their large number of lines, however, only a statistical approach can be used in order to reduce computational time and memory. The *Iron Opacity Interface* *IRONIC* calculates cross-sections for all kinds of transitions as input for the stellar atmosphere codes (Rauch & Deetjen 2003). In this approach the number of levels is reduced by combining all energy levels of one ion into energy bands, which are treated as a single NLTE super-levels with averaged energy and statistical weight. The cross-sections for a transition between super-levels are then calculated by sampling all individual lines. The input for the calculations of the cross-sections is taken from external sources like Seaton et al. (1994) or Kurucz (2009) (see section 5.3 for a discussion of the latter).

4.3 Stratified atmospheres

Based on the radiative levitation theory of Chayer et al. (1995a,b) (see section 2.3) self consistent models describing an atmosphere stratified by radiative and gravitational forces can be calculated with the *Next Generation Radiative Transfer (NGRT)* code by Dreizler (1999b). A good overview of the details of the underlying diffusion physics can for instance be found in Vauclair & Vauclair (1982) and Koester & Chanmugam (1990) and the aspects related to the *NGRT* code were recapitulated by Landenberger-Schuh (2005). Accordingly, diffusion in an atmosphere occurs when gradients of concentration, temperature, or pressure are present. In a white dwarf atmosphere a large pressure gradient defines the diffusion velocity, whereas the effect of the temperature gradient can be neglected. The time scale of the diffusion process caused by the pressure gradient is therefore short (cf. section 2.3) and can be written as

$$\tau_D \approx \frac{C}{k_P} \frac{H_P^2}{D}, \quad (4.10)$$

with the concentration C , the diffusion coefficient D , the pressure gradient coefficient k_P and its typical scale height $H_P = -dr/d \ln P$, which is short for the large gradient. A solution of the defining equation for H_P under assumption of hydrostatic equilibrium and the ideal gas equation shows that the density for heavier

elements will fall off quicker along the direction of the negative pressure gradient than that of lighter ones. Therefore, the lightest element floats on top of the others. Because of the swiftness of the process, the atmosphere can be regarded to be in equilibrium even if radiative forces are counteracting the gravitational settling, as long as no other mechanisms have to be taken into account. The abundances of the element i can then be derived using the balance of gravitational, radiative, and electrical forces of the main constituent, i.e. hydrogen in the case of a DA white dwarf atmosphere, $m_H a_H = m_i a_i$. Further considerations lead to the result that a stable equilibrium requires the effective gravitational acceleration g_{eff} and the radiative acceleration g_{rad} on each element to cancel each other

$$g_{\text{eff}} = g_{\text{rad}}. \quad (4.11)$$

Since g_{rad} depends on the mass fraction ρ_i . This can be expressed as

$$\left(1 - \frac{A_H (Z_i^{\text{eff}} + 1)}{A_i (Z_H^{\text{eff}} + 1)} \right) g = \frac{1}{\rho_i} \frac{4\pi}{c} \int_0^{\infty} \kappa_{\nu,i} H_{\nu} d\nu, \quad (4.12)$$

with the atomic weights A_i , the mean electrical charges Z_i , the mass fraction of the element ρ_i , the frequency dependent mass absorption coefficient $\kappa_{\nu,i}$ and the Eddington flux H_{ν} . Equation 4.12 can only be fulfilled for fixed values of ρ_i . This implies a depth dependence of the solution or, in other words, a stratified atmosphere. Since equation 4.12 includes the opacity and the Eddington flux, the determined abundances are coupled to the atmospheric structure. Therefore, the models have to be calculated using an iterative scheme (Schuh 2000). Radiation field, density, temperature stratification and the occupation numbers of all atomic energy levels can be taken as input from an atmosphere calculated with *PRO2*. With a new stratification for the trace elements calculated by equation 4.12 the next iteration step can be computed.

Tests and implementations

In order to reproduce the observed spectra in the following chapter suitable and realistic model atmospheres are necessary. To achieve a maximum of accuracy, different refinements, for example the effect of additional iron lines in the atomic data set and a changed treatment of bound-bound and bound-free transitions in the calculations with the NGRT code were investigated. The description is based on the numerical techniques explained in the previous chapter. Furthermore, the choice of a suitable frequency grid and the implementation of a proper convergence criterion for the calculations with the diffusion code are discussed.

5.1 Frequency grid

The resolution of the model spectrum used to analyze the observations depends on the choice of a proper frequency grid with a sufficient number of frequency points for the calculations. In this work, normally for the time consuming calculation of the temperature structure and the occupation numbers of elements in the atmosphere, a frequency grid with a not too large number of frequency points, roughly around 30 000, is used. For the detailed calculation of the emergent fluxes defining the spectrum, i.e. the formal solution of the radiative-transport equation, a much finer grid is used. Its primary goal is to resolve the individual lines in the observation. Therefore, it is mostly oriented on the spectral resolution of the observing instrument.

However, in order to include the opacity that defines the spectral energy distribution (SED), a suitable model frequency grid, including enough lines is of importance. For iron and nickel, with their large number of lines, test computations could give information about the effect of changes in the frequency grid. The purpose of the tests is to find an optimization for the *Chandra* wavelength range. They include calculations based on grids with additional frequency points for the wavelength range 20–3 000 Å. The spacings vary from a constant grid spacing of 0.1 Å for the whole range and 31116 frequency points, to a grid with a narrower spacing for

the wavelength range with many spectral lines. It starts with 0.05 \AA ($20\text{--}90 \text{ \AA}$) and varies thereafter (0.02 \AA for $90\text{--}400 \text{ \AA}$, 0.05 \AA for $400\text{--}600 \text{ \AA}$ and 0.5 \AA for $600\text{--}3\,000 \text{ \AA}$) with a resulting number of 27077 frequency points in total.

The tests show, as expected, significant discrepancies in the number of lines resolved. For the shape of the SED though, both approaches are suitable since no strong changes can be found. For the calculation of the emergent flux used for line identification, the interval between two wavelength points should not exceed 0.005 \AA , which corresponds to the *Chandra* spectral resolution, or as later necessary, to the spectral resolutions of the *FUSE* and *EUVE* instruments. For the comparison with the observation, the instrument response and effects like Doppler broadening have to be taken into account.

5.2 Convergence criterion

For the calculation of a stratified model atmosphere with the *NGRT* code in most cases an already converged homogeneous start model calculated with *PRO2* was taken. The velocity and the accuracy of the convergence depends on the methods applied for radiative transfer and temperature correction as discussed in Dreizler (2003). In the case of *NGRT* a Feautrier method as well as short characteristics can be used. The condition of radiative equilibrium has to be satisfied. This can be achieved by adjusting the run of temperature with depth, for instance via a partial linearization against the temperature (Auer & Mihalas 1968) or by a complete linearization of all constraint equations for radiative, hydrostatic, and statistical equilibrium (Auer & Mihalas 1969). The preferred temperature correction, however, is the Unsöld-Lucy scheme generalized to NLTE conditions, since it provides a better achievement of the nominal effective temperature (Lucy 1964; Dreizler 2003). This is of importance when comparing models in temperature grids with small differences in T_{eff} in the following chapters.

The convergence of the homogeneous model is characterized by sufficiently small changes in temperature and occupation numbers compared to the previous iteration step. This is also the case for the part of the diffusion model that defines the structure of the atmosphere. A direct criterion for convergence of a whole stratified atmosphere however was yet missing. A possible candidate is the flux change as used by Landenberger-Schuh (2005). Due to the large CPU time necessary to calculate a model, a change of less than 5% was suggested by the author for the whole frequency interval. This change guarantees a stable result independent from the initial conditions in the start model and only a few individual lines are still affected by more iterations. For the detailed analysis of individual lines a new criterion was implemented as used in the *ACDC* code of *TMAP* (Nagel et al. 2004),

checking for small flux variations in specific wavelength ranges. Different levels of convergence can be reached corresponding to changes in relative flux of $1 \cdot 10^{-2}$, $5 \cdot 10^{-3}$, $1 \cdot 10^{-3}$ and $1 \cdot 10^{-4}$ respectively. A comparison of test calculations performed with this criterion shows that the deviation of the abundance stratification and consequently the effect on the flux on wavelength ranges outside the regarded interval is negligibly small.

5.3 New atomic data

5.3.1 Iron

The availability of new iron lines supplied by Kurucz (2009) offers a more complete identification of lines especially in the X-ray wavelength range. Moreover, the effect of additional opacity provided by an excess of iron lines can be studied circumstantially. The original technique to derive the line data for complex atoms and ions was already described in Kurucz (1991), evolving from earlier calculations by Cowan (1968). Accordingly, the line lists were derived by combining levels that have been observed with computed Hartree-Fock integrals for higher configurations. Compared to the original Kurucz data (1999), in the case of iron in the new data set (2009), mainly lines with small f -values were added. In general, lines with minor f -values are less likely to appear in the spectrum of a star. However, a large amount of lines located close to each other can account for a visible decrease in the flux.

Figure 5.1 shows a comparison between the old and new data set. The lines are divided into extensions .LIN and .POS. The former are calculated for the whole set of transitions between all theoretically considered levels. Since these lines are only predicted, they are not useful for a detailed comparison with observed spectra. They are however suitable for a calculation of the model structure of the atmosphere. The .POS are computed between levels confirmed by laboratory measurements, hence appearing at verified wavelengths. Thus, for an assured identification of iron lines in the spectrum especially the plus of .POS lines is of importance. The chance of detecting lines of specific ions in the spectra varies with the parameters of the star and the considered wavelength range. The detailed analysis of the X-ray spectrum of LB 1919 follows in the subsequent chapter. Nevertheless a first estimation of the importance of new iron lines can be presented. Calculated models containing hydrogen and iron in varying ionization stages for a chosen set of parameters for effective temperature and surface gravity provide a clear picture of the occurrence of the different iron ionization stages in the spectrum of the star. Of all iron ionization stages appearing in the X-ray wavelength range for intermediate temperatures around 50 000-70 000 K, Fe VI is the dominating one contributing

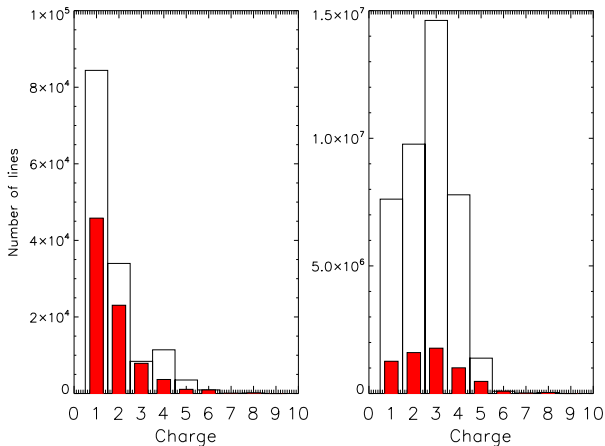


Figure 5.1: Comparison between the number of iron lines in the old (thin boxes) and new (thick boxes) data set. Left: .POS lines used for the calculation of the emergent fluxes only. Right: The whole amount of .LIN lines for the calculation of the model atmosphere.

most of the lines. A comparison of a model spectrum calculated with the old and the new iron line lists shows clearly the higher number of lines in the new list. For a comparison with an observed spectrum, however, scaling effects diminishing the absolute calculated values for the flux have to be taken into account. Thus, it is more important to see that the effect of additional lines can even contribute to significant features in the spectrum after convolving the model with the instrumental response of the observing instrument.

Figure 5.2 demonstrates the effect of additional lines used in the calculations. The top panels show the comparison between old line lists on the left and new line lists on the right appearing in a model spectrum calculated with hydrogen and iron with $T_{\text{eff}} = 57000 \text{ K}$ and $\log g = 7.90$ for the iron-line rich wavelength range $150\text{--}170 \text{ \AA}$. A significant amount of new lines is easily recognizable. The bottom panels illustrate the effect of the lines after convolving the model spectra with the instrumental response of the *Chandra* satellite. Despite their smaller f -values, the new lines obviously contribute due to their large number, which results in a strong absorption feature not visible in the atmosphere calculated with less lines.

This effect can be seen in figure 5.3, where a detailed view of the model spectrum calculated with the same parameters and the new set of Kurucz lines is shown covering a range of only 0.5 \AA . The labels indicate the positions of the .POS lines of the denoted ionization stage. Some lines are too weak to be visible in the spectrum. The large amount of iron lines at some locations however, produces the

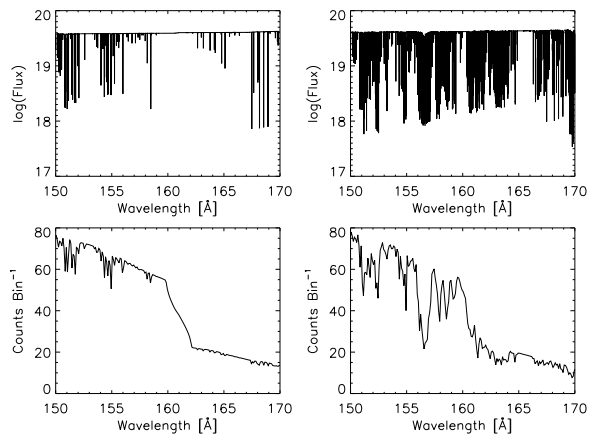


Figure 5.2: Comparison of model spectra calculated with the old line lists from Kurucz on the left with the new line lists (models with hydrogen and iron and the parameters $T_{\text{eff}} = 57000\text{K}$ and $\log g = 7.90$, top panels). The additional lines account for a significant decrease in flux even after convolving with the *Chandra LETG* instrumental response (bottom panels). Fluxes are in $\text{erg cm}^{-2} \text{Å}^{-1} \text{s}^{-1}$. The bin size is 0.1Å .

features visible in the spectrum especially around 156.85Å .

5.3.2 Nickel

The newly calculated data set for nickel is of less importance for the regarded X-ray range. This is due to the fact that the change in the number of lines between the old and new data set is comparably small. Consequently only a few more .LIN lines can be found in the X-ray range. More importantly, no X-ray .POS line is present in both new and old data sets. Furthermore, the SED of the flux in the regarded region is not influenced by the use of additional lines. While this holds for the considered wavelength range the effect on different regions can not be easily estimated. Therefore, using the new Ni data provides a way to account for any unseen opacity.

5.4 NGRT code

The code for the *Next Generation Radiative Transfer* as described in chapter 4 computes stratified abundances of elements in the atmosphere in a self-consistent way. The results provide in general a good agreement especially when analyzing

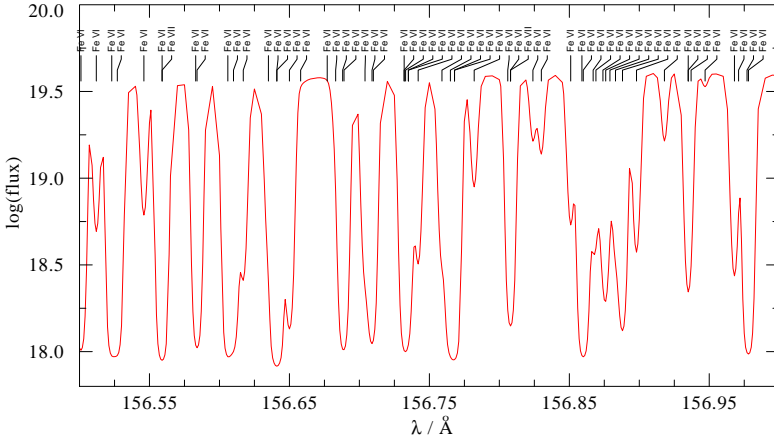


Figure 5.3: Many weak lines contributing to a significant decrease in flux. The model spectrum is calculated with $T_{\text{eff}} = 57000\text{K}$, $\log g = 7.90$, hydrogen and new Kurucz data for iron. The flux is in $\text{erg cm}^{-2} \text{Å}^{-1} \text{s}^{-1}$.

the SED of observed spectra. However, the fitting of specific spectral lines of individual species turned out to be the weak point in the calculations (Schuh 2000, see also chapter 6). Among the possible reasons is the neglect to include fine structure splitting of the levels in the model atoms used. For the calculation of a model atmosphere this would result in a large enhancement of the number of levels in the model atom, hence, an increase of CPU time. Furthermore, in the case of an atmosphere with a homogeneous mixture of elements, possible effects are insignificant. The energies of the splitted levels are close to each other. This allows to keep the levels combined and to deal with combined transitions during the calculation of the model atmosphere structure (Dreizler 1999b). The calculated radiation pressure in a stratified atmosphere on the other hand might be underestimated, since the self absorption in a combined level is higher than in the case of split transitions. This might lead to a systematic underestimation of the abundances.

Other problems tackled in order to refine the calculations with *NGRT*, concern the calculation of bound-free and bound-bound transitions.

5.4.1 Bound-free transitions

Photoionization of an atom or ion takes place when the photon energy exceeds the ionization energy of the electron. The primary assumption for the calculation of a bound-free (bf) transition in *NGRT* is that the photon momentum is transferred completely to the ion, keeping the electron out of consideration. As a consequence,

the calculated radiative acceleration of the remaining ion might be overestimated. To account for this, a correction according to Gonzalez et al. (1995) was implemented and tested. Therein the authors presented their calculations for the contributions of bound-bound and bound-free transitions to the radiative acceleration in stellar envelopes.

Accordingly, the radiative force on a particle of element A , with the ionic charge i for a bound-bound or bound-free transition j , caused by photons in the frequency range $(\nu, \nu + d\nu)$ is

$$F_{\nu}^{ij} d\nu = \frac{dp_{\nu}}{dt} = \sigma_{ij}(\nu) \frac{\mathcal{F}_{\nu}}{c} d\nu, \quad (5.1)$$

with the net momentum dp_{ν} , transported by the radiation flux \mathcal{F}_{ν} . In the case of the bound-bound transition the cross-section can be written using the oscillator strength f_{ij} and the line absorption profile $\phi_{ij}(\nu)$ as

$$\sigma_{ij}(\nu) = \frac{\pi e^2}{m_e c} f_{ij} \phi_{ij}(\nu). \quad (5.2)$$

As mentioned above, in the case of a bound-free transition, the momentum of the photon causing an ionization of ion A^i is not completely transferred to ion A^{i+1} . A part of it is taken away by the ejected electron. Thus, a correction factor f_{ion} has to be introduced, describing the fraction of the momentum transferred to the ion A^{i+1} .

The correction factor can be expressed in terms of the frequency ν of the photon, the threshold frequency ν_0 necessary to eject the electron and a variable factor a_1 .

$$f_{\text{ion}} = 1 - \frac{4}{3} \frac{(\nu - \nu_0)}{\nu} a_1. \quad (5.3)$$

For testing purposes the quantum calculation of Sommerfeld (1939) was taken and applied to the code. With his value of $a_1 = 6/5$, f_{ion} becomes

$$f_{\text{ion}} = 1 - \frac{8}{5} \frac{h\nu - \chi}{h\nu}, \quad (5.4)$$

with the frequency of the ionizing photon ν and the ionization energy threshold χ . An interesting result of formula 5.4 was already stated by Michaud (1970). For certain frequencies the electron can be ejected with more momentum than brought in by the photon ($f_{\text{elec}} = 1 - f_{\text{ion}} > 1$). As a consequence, the ion will be pushed back in the atmosphere by the photoionization. Thus, including a detailed bound-free absorption calculation can lead to both either higher or lower outward directed radiative forces on an ion.

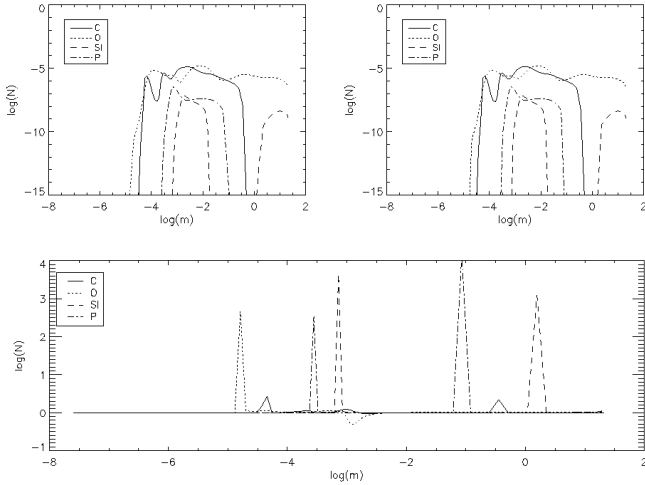


Figure 5.4: Top panels: Abundances over depth in a calculation of a model with H, C, O, Si, P and $T_{\text{eff}} = 54000\text{K}$, $\log g = 8.2$ with the whole momentum transferred to the ion in a bound-free transition (left). Only a part of the momentum is transferred to the ion, calculated with formula 5.4 (right). The difference between the two panels is shown in the bottom panel. No significant differences can be recognized. The peaks for larger differences rather correspond to a shift of the abundance pattern on the m axis. Mass m in g .

It should be noted that the value for a_1 was initially calculated for the hydrogen fundamental state. Therefore, the accuracy of the formula cannot be guaranteed for transitions between ions with large electron numbers. Nevertheless, it provides a good way of testing if any effects are to be expected at all. Moreover, calculations of Seaton (1995) for the states 2s, 3s, 2p, 3p and 3d, show a frequency dependence of the a_n but also reveal that for the weighted mean values for a state of principal quantum number n , the fraction of the total absorbed momentum, which is transferred to the electron is always smaller than that for the ground state. Newer calculations for one-electron systems (Massacrier 1996) and lithium ions Li I and Li II (Massacrier & El-Murr 1996) deviate clearly from the basic formula. However, the largest contributions to the bound-free force can be well approximated by using formula 5.4 for all bound-free absorptions (Richer et al. 1997).

To test the effect of the modified bound-free transitions, two types of models were calculated. One set of models includes the elements hydrogen, oxygen, silicon and phosphorus. In addition to that, models with hydrogen and iron were computed, in order to investigate the effect on iron with its large number of ab-

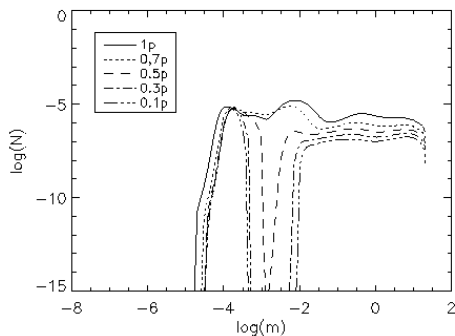


Figure 5.5: The oxygen abundances over depth in a model with H,C,O,Si and P, calculated with $T_{\text{eff}} = 54000\text{K}$ and $\log g = 8.2$. The abundance is shown for different percentages of transferred momentum to the ion in bf-transitions.

sorption lines separately.

For the first set of models the atmosphere calculations with $T_{\text{eff}} = 54000\text{K}$ and $\log g = 8.20$ show that the abundances of C, O, Si and P are not affected in a significant way by the modified bound-free transitions. The comparison between abundances at each depth of the atmospheres calculated with old and new bf-transitions reveal only minor, almost non-existent deviations (figure 5.4). Since the correction factor in formula 5.4 depends on the frequency, it is intuitively not clear how large the expected scaling effects are on the radiative forces.

To see if a modified treatment of the photoionization can have an impact on the abundances at all, different calculations have been carried out assuming a constant factor of momentum p transferred to the ion and varying its value. The value is lowered in steps of 0.2 starting with a high percentage of transferred momentum ($0.7p$). The result for $0.7p$ appears to be similar to the calculations with formula 5.4, only the abundances of oxygen and carbon are slightly affected, both species with very detailed model atoms. Lowering the transferred momentum to $0.5p$ leads to a large decrease in the abundance of oxygen at depths around $\log m = -3$. A momentum of $0.3p$ and $0.1p$ transferred decreases the abundance of oxygen in that region further and broadens the minimum to neighboring depths. This is illustrated in figure 5.5, where the abundances of oxygen in models calculated with different momentum transferred to the ion are depicted.

The other elements in the model are not strongly affected. The different ioniza-

tion stages of oxygen behave in a similar way. It can therefore be concluded that the modification of the photoionization affects the element as a whole. Furthermore, it is remarkable that only the abundance of one element, oxygen, is changed in a relevant way, while the other elements do not show a significant alteration.

In the newly computed models with hydrogen and iron, the relative number of iron ions in the atmosphere is not significantly changed. Especially in the regions $-2 < \log m < 0$, important for the line formation, the result is comparable to the old atmospheres. More important than the change of abundances with depth is therefore the possible effect on the emergent flux. The emergent flux resulting from the formal solution of the equation of radiative transfer for the X-ray wavelength range with its many iron lines shows very small differences. For flux values in the order of $10^{19} \text{ erg cm}^{-2} \text{ \AA}^{-1} \text{ s}^{-1}$ they are around $10^{15} \text{ erg cm}^{-2} \text{ \AA}^{-1} \text{ s}^{-1}$. For strong line features they add up to under 0.5%, for regions closer to the continuum they are even lower. For lines of other elements than iron the situation is similar. A closer look on the oxygen and carbon lines in the *FUSE* spectral range shows that they are as well not affected by bf-transitions modified with formula 5.4.

Obviously a modified treatment of the bound-free transitions in the model atmosphere computation can be accomplished by using formula 5.4 for all bf-transitions in the calculations of the cross-sections. The effects of the modification on the emergent flux, important for the line identification of elements, can be regarded as minor. The most important contribution for the radiative acceleration stems from the transitions between two bound states (Richer et al. 1997).

5.4.2 Bound-bound transitions

Bound-bound (bb) transitions are those between atomic levels in an atom caused by the absorption and emission of radiation (Mihalas 1970). If the energy of the radiation is absorbed by the atom an electron is moved to a higher level and the atom is excited until the energy is released. In the original *NGRT* code the redistribution of transferred momentum over the ionization stages in bound-bound transitions was disregarded. In other words, the momentum in such a transition was completely transferred to the next higher ion. This treatment is based on the assumption that a possible ionization following the excitation of the ion takes place before the ion is deexcited by transferring momentum to other ions through collisions. Especially in very hot atmospheres this can not always be guaranteed. The high temperature corresponds to a high thermal velocity $v_{\text{th}} = \sqrt{3kT/m}$ ¹ which results in a small time between the collisions $\tau \sim l/v_{\text{th}}$ ². Therefore, for a realistic treatment the probabilities for an ionization process in an ion and for a collision

¹With the Boltzmann constant $k = 1,3806504(24) \cdot 10^{-23} \text{ J K}^{-1}$ and the mass of the atom m .

²Here the mean free path l depends on the particle density n and the cross-section σ , $l = (\sigma n)^{-1}$.

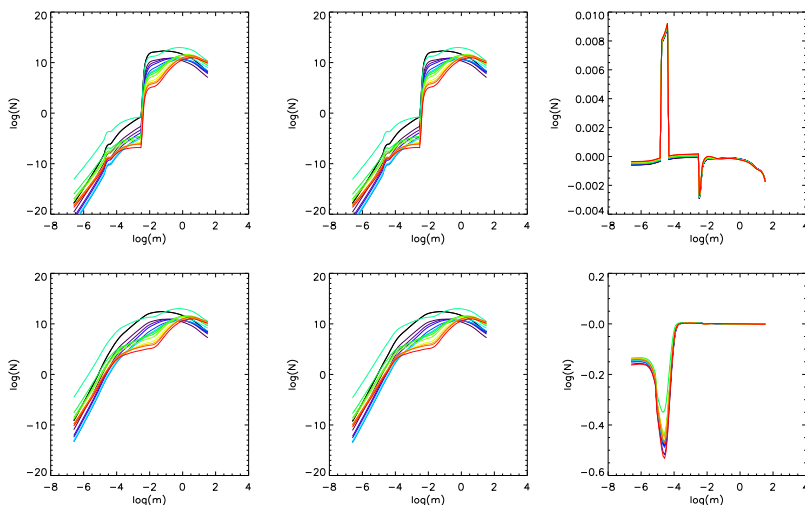


Figure 5.6: The effect of modified bound-bound and bound-free transitions on the occupation numbers of iron super levels in the atmosphere exemplarily shown for the bands of Fe V and Fe VI in a model with $T_{\text{eff}} = 56000\text{K}$ and $\log g = 7.9$. Starting with the top left and going clockwise, the plots show the following: 1. Model calculated with the original treatment of bb- and bf-transitions. 2. New treatment of bound-free transitions. 3. Difference between the first two. 4. New calculation of bound-bound transitions. 5. Both refinements are implemented. 6. Difference between the last two.

between two ions have to be determined precisely. In any event the momentum is either transferred to the next higher ion A^{i+1} or to the originally excited ion A^i .

As a first approach and to test the consequences, the calculation of the bb-transitions is modified to keep the whole momentum at the *lower* ion A^i .

The results for the first set of models resemble the investigation of the bound-free transitions. This time however phosphorus shows the greatest deviation. The abundances on both the inner and the outer part of the atmosphere are higher, while the intermediate regions again show only a slight difference.

For iron the behavior is similar. The structure of the distribution of the abundances is smoother than originally, leading to a higher number of ions at small depths. In figure 5.6 the influence of the modified treatment of both the bf- and bb-transitions on the occupation numbers of several iron levels can be seen. While the modified bf-transitions leave the occupation numbers almost unaltered, a modification of the bb-transition results in a recognizable change. The effect on the

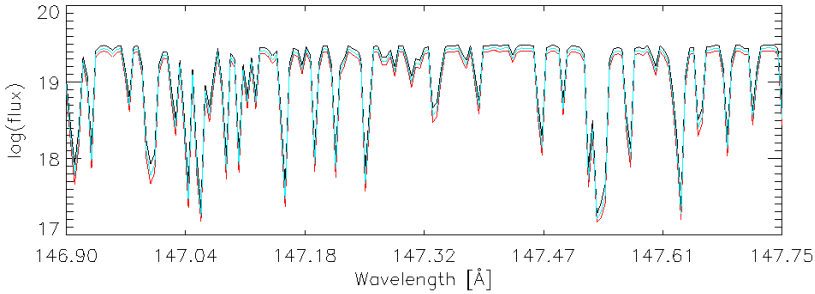


Figure 5.7: Effect of a modified treatment of bound-bound transitions on a model with hydrogen and iron and $T_{\text{eff}} = 56000\text{K}$, $\log g = 7.9$. A model with full momentum given to ionization stage A^i (black) is compared to a model with full momentum at stage A^{i+1} (red) and a model with half of the momentum attributed to each stage (blue). The new treatment of bound-free transitions is implemented in all three models.

emergent flux is larger than found for the modified bound-free transitions. The changes sum up to a mean deviation between the fluxes of under 15%, for particular line features they can however exceed this value. This deviation is not extremely higher than the original change in flux taken for the convergence criterion by Landenberger-Schuh (2005), even though it should be noted that the criterion allowed only a *maximum* flux change of 5%. Nevertheless, a significant influence on possible line identifications can not be recognized. Furthermore, the complete lack of any momentum transfer to the higher ionization stage is the maximum impact possible on the computed spectrum and is not very realistic.

For this reason as an additional test only half of the momentum transferred was kept at ion A^i . The other half was distributed to ion A^{i+1} . This is implemented by simply changing the treatment in the calculation for every second ion. Since the ions are virtually randomly chosen, this method can not be regarded as realistic. Nevertheless, it gives insight in the influence of the bb-transitions on the emergent flux.

The change reduces the difference with the *old* model further. In fact the discrepancies are lowered to at least half the deviation observed for a model with full momentum at ionization stage A^{i+1} . Figure 5.7 shows a comparison of three models calculated with different momentum attributed to the higher ionization stage A^{i+1} . Obviously an effect is mainly noticeable if the whole momentum is kept at the lower ionization stage. A reduced amount of momentum transferred to the lower stage does not result in an important change in the emergent flux. Therefore a more complex treatment of the rescaling over the ionization stages, as described

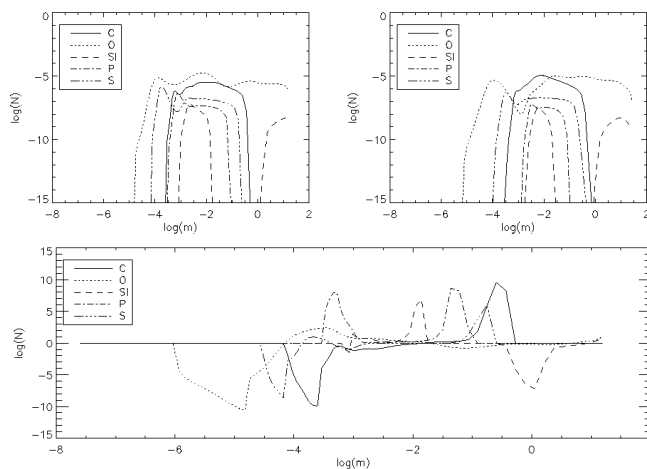


Figure 5.8: Top panels: Abundances in a model calculated with $T_{\text{eff}} = 54\,000\text{ K}$, $\log g = 8.2$ and elements H, C, O, Si, P, and S (left). Abundances of the elements calculated in a model with hydrogen and one single other species (right). Bottom panel: Differences between both top panels. All models calculated with $T_{\text{eff}} = 54\,000\text{ K}$ and $\log g = 8.2$.

above, may be considered unnecessary.

5.5 Model atoms

As described in the previous section, the self consistently calculated abundances of the elements at each depth depend on the momentum, which is transferred to the atom. Since the momentum can only be transferred via transitions between levels that are included in the atom, a detailed model atom with many bound-bound transitions is of importance. The higher the number of levels and transitions in the model atom is, the larger the computational time and memory required. Therefore, for computations with many elements in most cases the number of NLTE levels is restricted to the important ones. These are the basic levels of each ionization stage. For ionization stages with lines in the observed spectra more NLTE levels are calculated. Other levels are treated in LTE.

The effect of a varying number of lines and transitions on the radiative acceleration was tested for different atoms. For the elements C, O, Si, P and S models with hydrogen and one of the five elements, as well as a model including hydrogen and all elements simultaneously, were calculated. Whereas the number of levels

Table 5.1: Overview of the model atoms used for the calculations of the model with the elements H, C, O, Si, P, and S (small), and for the models with hydrogen and one single other element (big).

	H	C	O	Si	P	S
NLTE levels (small)	11	89	107	71	37	56
NLTE lines (small)	45	401	388	139	21	112
NLTE levels (big)	11	159	302	142	87	96
NLTE lines (big)	45	853	1561	165	21	222

treated in NLTE is limited for the model with all elements, for the models with the single atoms the maximum number of NLTE levels and transitions is used. The exact number of NLTE levels and transitions used is shown in table 5.1.

The effect on the abundances of the elements can be studied in figure 5.8. The abundances of the elements in the model atmosphere calculated with all elements and hydrogen with the small model atoms is seen on the left. The right panel shows the abundances of the elements in a model calculated with hydrogen and one specific element only, using big model atoms. Slight differences between both cases can be found, which are shown in the lower panel. The overall behavior of the abundances in each depth of the atmosphere, however, is almost identical. This means that the abundances are not much affected by including more NLTE levels for one element.

To rule out that possible interactions between the elements can be the cause for the differences, model atmospheres including H and one single other species with small element model atoms were calculated. These atmospheres show the same abundance profile as the atmospheres calculated with H and all other elements simultaneously (see figure D.2 in the appendix). A model atmosphere including H and a combination of two elements (Si,P), which makes use of the high number of NLTE levels and transitions for both elements, confirms this result and agrees with the previously calculated abundance profiles for Si and P in the models with these elements and only H with the big model atoms. The results in figure 5.8, however, show that for the biggest model atom used (O) with the largest number of levels, the biggest deviations can be found. Obviously, not only the relative number of levels treated in NLTE plays an important role, but also the absolute amount of levels available for the model atom is relevant.

A change in number of NLTE levels used in the diffusion calculations goes at the expense of a longer computational time. Therefore, including more NLTE levels is

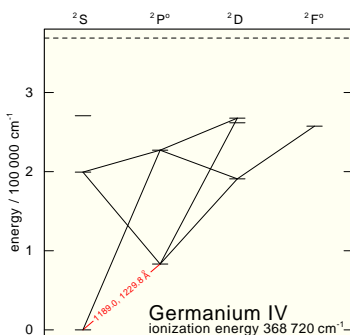


Figure 5.9: Grotrian diagram showing the considered transitions between the energy levels in the Ge IV ion. The 4s-4p transition that produces a doublet at 1189.03 \AA and 1229.84 \AA is marked.

only reasonable if an effect on the emergent fluxes and the line features of elements is expected. This effect, however, is minor. The tests show that only for Si and P recognizable differences can be found for features in the *FUSE* wavelength range (see figure D.1). The Si line gets stronger while the P line shows a weaker feature. This might explain the tendency of the diffusion model to produce too weak Si and too strong P lines in the analysis of *FUSE* spectra in chapter 6.

5.6 Germanium model atom

For the detailed analysis of the line features in the *FUSE* spectrum of the white dwarfs in chapter 6, suitable atomic data is necessary. For the most common elements in stellar atmospheres very detailed model atoms exist. They include confirmed level energies and oscillator strengths for transitions between the levels. This results in photon cross-sections, which are either calculated for each level individually or by combining all energy levels of one ion into several bands, as done for the line-rich iron group elements (cf. section 4.2). For the heavy elements beyond the iron group ($Z > 30$), however, not enough details of the occurring transitions are known yet.

An example of such a heavy atom is Ge. Lines of Ge IV have only recently been identified for the first time in a WD spectrum (Vennes et al. 2005). Due to the lack of data, a suitable model atom for the computations could only be derived approximately. For their LTE analysis Vennes et al. (2005) used the *SYNSPEC* code by Hubeny & Lanz (2000). It was modified to include partition functions and ionization energies from the *ATLAS9* code (Kurucz 1993) for the neutral, +1,

Table 5.2: Properties of the transitions in the GeIV model ion (first column). The 4s-4p transition used for the computation of the model structure is splitted for the calculation of the synthetic spectrum. The f -values are either taken from Chayer et al. (2005) or adapted from a CIV model ion.

Transition	f -value	Wavelength [\AA]	Source
4s-4p	$7.483 \cdot 10^{-1}$	1202.33	Chayer et al. (2005)
4s-4p(1/2)	$2.494 \cdot 10^{-1}$	1229.84	Chayer et al. (2005)
4s-4p(3/2)	$4.989 \cdot 10^{-1}$	1189.03	Chayer et al. (2005)
4s-5p	$2.142 \cdot 10^{-1}$	440.37	CIV
4p-5s	$1.275 \cdot 10^{-1}$	861.39	CIV
4p-4d	$1.012 \cdot 10^{-1}$	929.54	CIV
4p-5d	$5.125 \cdot 10^{-1}$	542.43	CIV
4d-4f	$3.648 \cdot 10^{-3}$	1498.32	CIV
5s-5p	$8.423 \cdot 10^{-1}$	3594.82	CIV
5p-5d	$1.443 \cdot 10^{-1}$	2472.43	CIV

and +2 ionization stages of germanium (Proffitt et al. 2001). For the next two higher ionizations stages of Ge the partition functions could only be approximated by the ground-state statistical weights. For cool atmospheres ($T_{\text{eff}} \leq 30000\text{K}$) the high-lying states are of less importance and the expected deviations are small. The higher the temperature, the more relevant these states become and the approximation becomes unreasonable.

In any event, the partition functions and the statistical weight approximation can only be used under LTE conditions. In chapter 6 the first NLTE analysis of Ge in a stellar atmosphere is described. The properties of the Ge atom are determined using a different approach. The newly modeled Ge atom used in these calculations is rather rudimental. The energies of the levels are taken from the *National Institute of Standard and Technology (NIST)* atomic spectra database (<http://physics.nist.gov/>). These level energies and the corresponding transitions in the GeIV ion are shown in a Grotrian diagram in figure 5.9.

The oscillator strength of the radiative bound-bound transition between the 4s and 4p levels is taken from Chayer et al. (2005). This transition is splitted for the calculation of the synthetic spectrum and corresponds to a doublet at 1189.03 \AA and 1229.84 \AA . The oscillator strengths of the other transitions are not known. Therefore, the f -values of the known transitions of the isoelectronic CIV ion are used instead. Table 5.2 gives an overview of the used f -values of the transitions and their sources. The most important transition between the 4s and 4p level has

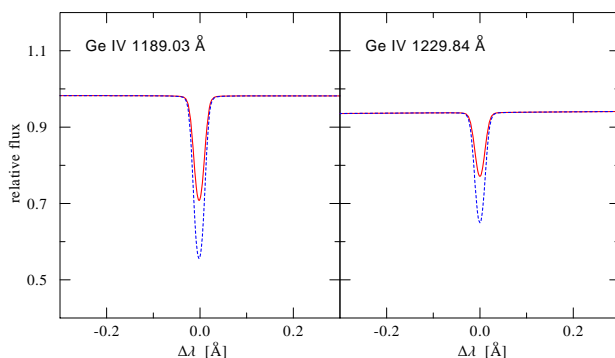


Figure 5.10: Ge IV line profiles from model atmospheres with H and Ge calculated with $T_{\text{eff}} = 57000\text{K}$ and $\log g = 7.6$. One model is computed with NLTE occupation numbers and the approximations mentioned in the text (solid line). The other model is forced into LTE by increase of the collisional rates (dotted line).

adequate f -values. The approach to adapt carbon f -values for germanium can be justified by the similar electron configuration and level energies of the two elements. However, it should be kept in mind that in a model calculated with a homogeneous mixture of elements, this approximate atom might produce line strengths that are either too weak or too strong compared to a more detailed model atom. Nevertheless, the calculations account for a NLTE condition and are more likely to reproduce realistic line strengths than a pure treatment of LTE. To check how big the difference between LTE and NLTE models are, the NLTE atmospheres can be forced into simulating a LTE condition. This is done by increasing the collisional rates. If they dominate over the radiative rates, i.e. the departure coefficients are close to unity, the atmospheric structure can be regarded to be in LTE.

The effect of NLTE can be seen in figure 5.10. The line strength is weaker than for the LTE model atmospheres. Obviously a Ge abundance determined by a fit to at least one line of the Ge IV doublet depends on the treatment of the statistical equilibrium. The resulting difference in the line strength corresponds to a change of a factor 2 in the abundance derived by a line fitting procedure. A deviation due to the approximate model atoms can be excluded, since they are implemented in both models. The relative line strengths of the LTE and NLTE models should therefore be realistic even if the absolute strength of the lines can still be imprecise. The identification of the component at 1189.03 \AA and the attempt to determine the Ge abundance in a WD spectrum with the model atom is described in section 6.7.

Analysis of LB 1919 and GD 246

In this chapter the analysis of the white dwarfs LB 1919 and GD 246 is described. For a better understanding of the development of the obtained results the chapter is structured in the following way. First, a brief overview of previous investigations of LB 1919 is given (section 6.1), followed by the analysis of the *Chandra* spectrum with homogeneous and stratified model atmospheres including hydrogen iron and nickel (section 6.3). The same is done for GD 246 (sections 6.4 and 6.5). In the following sections (6.6 and 6.7) the *FUSE* spectra of both stars are analyzed and elements and abundances identified. With the won information the *EUVE* spectra of both stars are analyzed (section 6.9). Finally, the *Chandra* spectra are investigated again with the knowledge of the composition of the atmospheres gained from the results of the prior analysis (sections 6.10 and 6.11).

6.1 Previous investigations (LB 1919)

LB 1919 has first been investigated by Vennes et al. (1997). They presented their effective temperature and surface gravity determinations for a sample of 90 hot white dwarfs detected in the *Extreme Ultraviolet Explorer (EUVE)* all-sky-survey. Effective temperature and surface gravity were constrained using Balmer line spectroscopy and pure-hydrogen model atmospheres. For the determination of the chemical composition EUV photometry and spectral synthesis with variable abundances of helium and heavy elements (C, N, O, S, Si, Fe) was used. While Vennes et al. (1997) obtained $T_{\text{eff}} = 68640\text{K}$ and $\log g = 8.08$, Finley et al. (1997) failed to determine the effective temperature by performing fits to the Balmer lines using their model atmospheres. Although LB 1919 appeared to have a normal gravity, Finley et al. (1997) discovered flat-bottomed Balmer line profiles and suggested orbital or rotational velocities of $\sim 1000\text{km s}^{-1}$ as a possible interpretation.

The next investigation of LB 1919 has been accomplished by Wolff et al. (1998a). They concentrated on a sample of 20 DA white dwarfs from the *EUVE* public archive. Since the spectral resolution of the *EUVE* instrument is too low to detect

individual metal lines, they chose the well studied DA G 191-B2B as reference object for the analysis of the other white dwarfs. Assuming the same relative abundances as for G 191-B2B and introducing a free scaling factor for the total amount of metals, they were able to reproduce the spectra of most of the considered DAs. For LB 1919 they determined a metallicity at least ten times smaller compared to that of G 191-B2B, assuming the values for T_{eff} and $\log g$ from Vennes et al. (1997).

Based on previous results, Landenberger-Schuh (2005) had performed an analysis of an EUV selected sample of hot DA white dwarfs using new model atmospheres, assuming equilibrium between gravitational and radiative forces in each depth of the atmosphere. The parameters in such a diffusion model are reduced to the effective temperature and the surface gravity and describe a chemically stratified atmospheric structure (see also chapters 2 and 4). In the case of LB 1919 the use of the new models however resulted in a worse fit compared to the analysis of Wolff et al. (1998a) with homogeneous models. The reason remained unexplained.

In general, a few processes could disturb the reached equilibrium (see also section 2.4), each of which not likely to occur in a hot DA white dwarf like LB 1919 though. Mass loss for instance would have the effect of homogenizing a stratification of chemical elements. For DAs cooler than 70 000 K, this phenomenon should not yet occur, since mass loss rates drop below a critical limit ($10^{-16} M_{\odot}/\text{yr}$, Unglaub & Bues 1994). Wind accretion for LB 1919 is prevented, instead a mass loss rate of $> 10^{-18} M_{\odot}/\text{yr}$ can be expected, following wind accretion calculations by MacDonald (1992). Due to its almost completely ionized hydrogen atmosphere, LB 1919 is convectively stable, so that a convective homogenization can be ruled out. A mixing via rotation at last can be regarded as very unlikely. WDs are in general very slow rotators and the analysis of a LB 1919 FUSE spectrum shows specifically deep and sharp Lyman line cores which exclude a high rotation rate.

6.2 Chandra observation (LB 1919)

A *Chandra* observation was proposed to clarify whether the distribution of metals in the atmosphere of LB 1919 is stratified or homogeneous. If the former is the case, the metals would be in a diffusion/levitation equilibrium, meaning that the low metallicity is a consequence of a process acting in an earlier evolutionary stage, which has depleted the metals in the hydrogen envelope. Homogeneous abundances on the other hand would suggest one of the before mentioned processes to be currently acting, contrary to expectations from theory. To identify lines of iron group elements, a *Chandra* observation with a 120 ks exposure time was performed on January 2nd 2006. Using the *Low Energy Transmission Grat-*

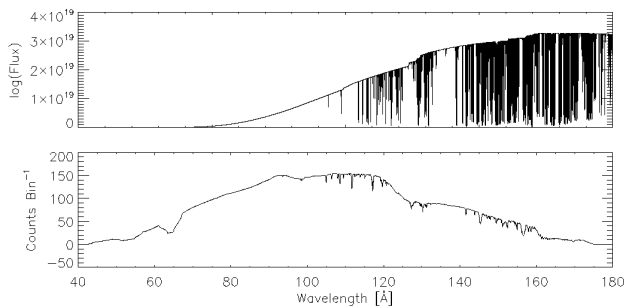


Figure 6.1: Calculated model flux (top) used to simulate the *Chandra* count rate spectrum (bottom). Model with $T_{\text{eff}} = 54000\text{K}$ and $\log g = 8.2$ and the elements hydrogen and iron. Flux is in $\text{erg cm}^{-2} \text{\AA}^{-1} \text{s}^{-1}$. The bin size 0.1\AA .

ing (*LETG*) in combination with the *High Resolution Camera spectroscopic array (HRC-S)* onboard the satellite, a spectrum in the wavelength range $5\text{--}140 \text{\AA}$ was obtained. The first attempt was to reproduce this spectrum with a model atmosphere calculated with a homogeneous mixture of elements. Since the composition of the LB 1919 atmosphere was not known yet, it was first concentrated on a basic hydrogen atmosphere and iron and nickel respectively were added to obtain detailed information about the population of ionization states of those elements.

6.3 Comparison with observation (LB 1919)

6.3.1 Homogeneous models

In the case of a homogeneous mixture of elements in the atmosphere the model structure of the atmosphere was computed with the *PRO2* code of *TMAP*. The emergent fluxes have then been calculated by performing a formal solution with detailed model atoms and frequency grids with the *line1_prof* code. For the stratified models the *NGRT* code was used (see chapter 4 for details). The flux has then been re-binned, convolved with the response file and multiplied with the effective area of the satellite to compare with the *Chandra* observation. The interstellar absorption applied to the model has been taken from Wolff et al. (1998a). Their value for the hydrogen and helium column density, i.e. the number of particles per cm^{-2} towards the star, is $N(\text{HI}) = 1.6 \cdot 10^{19} \text{cm}^{-2}$ and $\text{He I/HI} = 0.07$ respectively. Figure 6.1 shows the resulting model in counts per bin.

Even though the eye was the main instrument used for the comparison of ob-

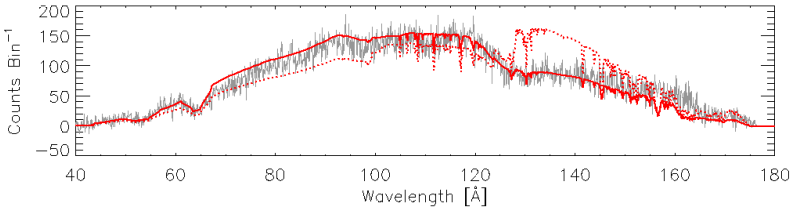


Figure 6.2: Attempt for the determination of Fe abundances in the *Chandra* spectrum of LB 1919 (thin line). Overplotted are homogeneous models with $T_{\text{eff}} = 54\,000\text{K}$, $\log g = 8.2$, hydrogen and different iron abundances in number ratios. Thick line: $\text{Fe}/\text{H} = 1.25 \cdot 10^{-6}$. Dotted line: $\text{Fe}/\text{H} = 1.25 \cdot 10^{-5}$.

served and computed spectra, a chi-square analysis was performed for a given wavelength range to help receive a better overall fit. The abundances in the following analysis are given in number ratio relative to hydrogen is not stated otherwise. As a first approach homogeneous models with hydrogen and iron in different ionization stages for a fixed abundance of $\text{Fe}/\text{H} = 1 \cdot 10^{-4}$ were calculated to check for the occurrence of Fe lines in the *Chandra* wavelength range. Later nickel was added to the calculations. While no lines of lower ionization stages (I–V) are visible in the *Chandra* range of the model spectrum and only a few from Fe VI and Ni VI, lines from Fe VII–VIII and Ni VII–VIII are clearly visible. However, compared to the observation, the strengths of the lines is far too large.

Therefore, the amount of iron and nickel was reduced gradually. Figure 6.2 shows a comparison between two models with hydrogen plus a varying abundance of iron. An iron abundance of $\text{Fe}/\text{H} = 1.25 \cdot 10^{-5}$ shows spectral line features that are obviously still too strong for the given values of T_{eff} and $\log g$. Furthermore, it is messing up the overall shape of the model spectrum. As a result the flux at lower wavelengths is depressed and increases at longer wavelengths. An amount of $\text{Fe}/\text{H} = 1.25 \cdot 10^{-6}$ gives a much better fit to the observation.

To study the behavior of the overall flux shape for a fixed amount of iron in detail, a grid of models was computed, according to the parameters determined by Vennes et al. (1997). This grid includes temperatures from $T_{\text{eff}} = 64\,000\text{K}$ up to $T_{\text{eff}} = 74\,000\text{K}$ in steps of $5\,000\text{K}$, while surface gravities range from $\log g = 7.9$ to $\log g = 8.5$ in 0.3 dex differences. The iron abundance was fixed to a value of $\text{Fe}/\text{H} = 1.25 \cdot 10^{-7}$. For the possible identification of iron lines only the .POS lines from the Kurucz database (Kurucz 2009) were used (see chapter 5). The overall shape of the flux is in good agreement with the observed spectrum for the temperatures in the grid ($T_{\text{eff}} = 64\text{--}74\text{ kK}$), yet the fit is best for $T_{\text{eff}} = 64\,000\text{K}$

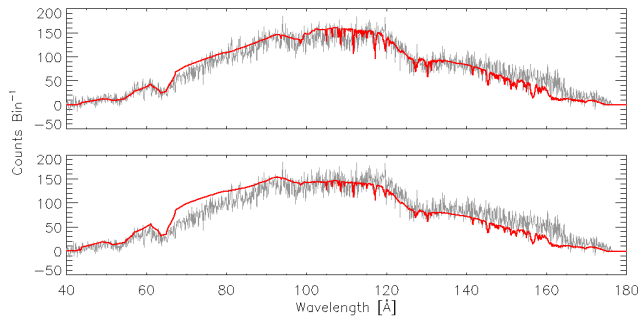


Figure 6.3: Top: Homogeneous model with $T_{\text{eff}} = 64000\text{K}$, $\log g = 7.9$ (thick line) plotted over the *Chandra* spectrum (thin line). Bottom: The same for a stratified model with $T_{\text{eff}} = 59000\text{K}$ and $\log g = 8.5$ (thick line).

indicating that the temperature of LB 1919 might be a little lower than expected. The models are more affected by a change in surface gravity at wavelengths lower than 80 \AA and are best for $\log g = 7.9$. Unlike this fitting of the overall shape, an identification of iron lines remains difficult if not impossible, since no clear line structure is visible in the observed spectra. An overview of the dependence of the fit quality on T_{eff} and $\log g$ can be found in figure A.1.

6.3.2 Stratified models

In comparison with the homogeneous models, the abundances of the trace elements in the stratified model atmospheres are calculated self-consistently. Thus, the only free parameters determining the behavior of the overall flux shape are the effective temperature and the surface gravity. However, compared to the models calculated with a homogeneously mixed atmosphere with the same temperature and $\log g$ parameters, the overall spectral shape is very different. For small surface gravities ($\log g = 7.9, 8.2$) and subsequently weaker gravitational forces, the theoretical flux deviates tremendously from the observations. This can be explained by a too large amount of iron levitating in the atmosphere (compare figure 6.2). The best fit in the assumed parameter range can therefore be achieved with the highest surface gravity of $\log g = 8.50$. The varying temperature has only a minor influence on the fit. However, similar to the homogeneous models, a temperature of $T_{\text{eff}} = 64000\text{K}$ results in a better fit. An even lower temperature of $T_{\text{eff}} = 59000\text{K}$ improves the fit further (see figure A.3). This temperature, however, lies outside the assumed grid. The comparison of the observed spectra with model fluxes, calculated with

varying iron abundances for different temperatures and $\log g$ in the homogeneously mixed case, implies that no or only a small amount of iron ($\text{Fe}/\text{H} < 1.25 \cdot 10^{-7}$) and other iron group elements is present in the atmosphere of LB 1919. An overview of the T_{eff} and $\log g$ dependence of the fit quality of the stratified models can again be found in the appendix (figure A.2). Smaller effective temperature ($< 69\,000\text{K}$) and surface gravities (< 8.5) result in a better fit for homogeneous atmospheres. Contrary to that, for the stratified models, high surface gravity (> 8.2) is necessary to achieve an acceptable agreement. Figure 6.3 demonstrates the different behavior of homogeneous and stratified models. Whereas the homogeneous model (top panel) is calculated with a relatively low surface gravity of $\log g = 7.9$, the stratified model (lower panel) needs a significantly higher value of $\log g = 8.5$ for a good agreement.

6.4 Previous investigations (GD 246)

To verify that the lack of iron lines in the *Chandra* spectrum of LB 1919 is indeed a special property of this specific star it was compared to a *Chandra* observation of the DA white dwarf GD 246 (also known as GSC 01164-01078, EUVEJ2312+107, REJ231219+104710, WD 2309+105). As for LB 1919 effective temperature and surface gravity of GD 246 have been determined by Vennes et al. (1997), who found $T_{\text{eff}} = 60\,100\text{K}$ and $\log g = 7.72$ by fitting Balmer lines with pure hydrogen model atmospheres. Subsequent investigations led to slightly different values based on fits of Balmer and Lyman lines using LTE and NLTE model atmospheres. Table 6.1 gives an overview of the published results. Noteworthy is the attempt of Schuh et al. (2002) who received their parameters by a fit of a stratified model atmosphere on an *EUVE* observation overall flux shape. In the most recent work, Koester et al. (2009) used improved model atmospheres including improved Balmer line broadening data and performed a χ^2 minimization based on the Levenberg-Marquardt algorithm (Press et al. 1992).

Vennes & Dupuis (2002) identified iron and nickel in several ionization stages in a LETG/HRC-S *Chandra* spectrum of GD 246. Their NLTE analysis of the complex of Fe VI/VII lines indicated an iron abundance of approximately $\text{Fe}/\text{H} = 3 \cdot 10^{-7}$, i.e. 1% solar. A small number of lines of trace metals could be identified in the *Far Ultraviolet Spectroscopic Explorer (FUSE)* and *Hubble Space Telescope (HST)* spectra of GD 246. Beside elements known to appear in white dwarfs like silicon, carbon and phosphorus, Vennes et al. (2005) identified for the first time lines of Ge IV in a *HST* observation with an abundance of $\log(\text{Ge}/\text{H}) = -8.6 \pm 0.2$. A nebular (*Inter Stellar Medium (ISM)* or circumstellar) origin could be excluded. Assuming similar ionization fractions of C IV and Ge IV and solar proportions, a

Table 6.1: GD 246 effective temperature and surface gravity as determined by previous analysis. Methods and authors are given in column 3 and 4 the composition of the model atmospheres in column 5.

T_{eff} [K]	$\log g$	Method	Authors	Atmospheres
60 100	7.72	LTE Balmer	Vennes et al. (1997)	pure H
58 700	7.81	LTE Balmer	Finley et al. (1997)	pure H
59 000	7.80	LTE <i>EUVE</i>	Wolff et al. (1998b)	H+metals
53 100	7.85	NLTE Balmer	Napiwotzki et al. (1999)	pure H
56 000	8.20	NLTE stratified <i>EUVE</i>	Schuh et al. (2002)	H+metals
52 000	7.90	NLTE Lyman+Balmer	Barstow et al. (2003a)	H+metals
51 300	7.91	NLTE Balmer	Barstow et al. (2003b)	H+metals
54 400	7.90	NLTE Balmer	Liebert et al. (2005)	pure H
57 007	7.82	NLTE Balmer	Koester et al. (2009)	pure H

scaled column density for germanium would result in a clearly undetectable equivalent width.

Different information on the values for hydrogen column densities can be found in the literature, ranging from a low value of $N(\text{HI}) = 1.3 \cdot 10^{19} \text{cm}^{-2}$ (Barstow et al. 1997, Oliveira et al. 2003), to $N(\text{HI}) = 1.8 \cdot 10^{19} \text{cm}^{-2}$ (Wolff et al. 1998a). An overview is given in Wolff et al. (1999). The quality of the agreement between observation and model depends on the interstellar absorption chosen (cf. section 6.11). A better fit for the *Chandra* spectrum can be achieved by a small value of the interstellar hydrogen column density. The following analysis uses therefore $N(\text{HI}) = 1.3 \cdot 10^{19} \text{cm}^{-2}$, $\text{He I}/\text{HI} = 0.05$ and $\text{He II}/\text{HI} = 0.026$.

6.5 Comparison with observation (GD 246)

6.5.1 Homogeneous models

Analogously to LB 1919, an analysis of a LETG/HRC-S *Chandra* spectrum of GD 246 was carried out. Contrary to LB 1919 in this case the spectrum shows a large amount of photospheric features so that the first approach with an atmosphere consisting of hydrogen and iron already leads to the identification of lines of several ionization stages. Thanks to the previous investigations elements and abundances, as well as effective temperature and surface gravity of GD 246, are known more concretely. Figure 6.4 shows the *Chandra* spectrum of GD 246 together with a model calculated with the $T_{\text{eff}} = 55\,000 \text{K}$ and $\log g = 7.9$. The model flux has

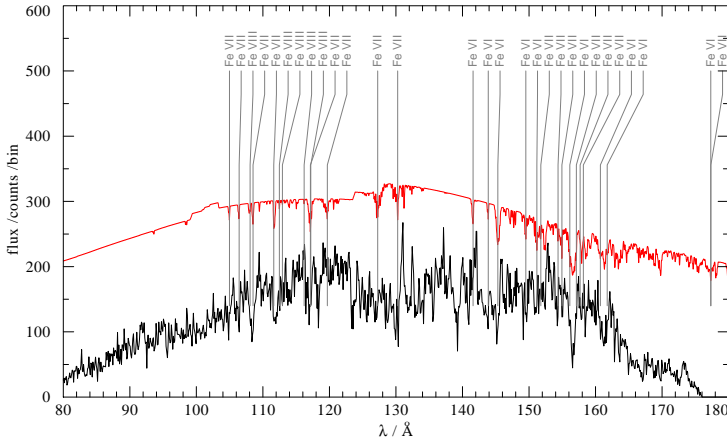


Figure 6.4: *Chandra* spectrum of GD 246 (thin line in counts per bin with a bin size of 0.1 \AA) with model spectrum (thick line in relative flux) with hydrogen and an iron abundance of $\text{Fe}/\text{H} = 1.25 \cdot 10^{-6}$, showing identified iron lines. Model spectrum calculated with $T_{\text{eff}} = 59000 \text{ K}$, $\log g = 7.9$ and shifted for clarification.

been convolved with the instrumental response and shifted to make the identification easier. Recognizable are iron lines in ionization stages VI, VII and VIII. The iron abundance in the model atmospheres can be as high as $\text{Fe}/\text{H} = 1.25 \cdot 10^{-6}$. A lower value (Vennes & Dupuis 2002) leads to a weaker line structure so that almost no Fe features are visible in the model spectra. Higher values, as noticed for LB 1919, derange the overall flux shape (see figure A.6). An abundance determination for Ni gives the same result. However, in this case only the SED of the flux can be taken as the abundance indicator, since no individual Ni features can be identified in the *Chandra* spectrum. A calculated grid of spectra around mean values for effective temperature and surface gravity considering the NLTE analysis in table 6.1¹, shows that the behaviour of this shape follows in general similar characteristics as the LB1919 flux shape. The grid includes the T_{eff} range from 52 000 K to 62 000 K with steps of 5 000 K and goes from $\log g = 7.6$ to 7.9 in 0.3 dex (see figure A.4 for a model overview). The fit suggests this time a higher temperature but is still comparable to the previous results. The surface gravity has to be lowered to a value of $\log g = 7.1$ to guarantee a smooth fit in the wavelength range lower than 100 \AA . This can be seen in the top panel of figure 6.5, where a model with $T_{\text{eff}} = 52000 \text{ K}$ and $\log g = 7.1$ is overplotted over the spectrum (see also figure A.7 for a comparison of homogeneous models with different $\log g$). A

¹The value of Koester et al. (2009) has not yet been published at that point and was not included.

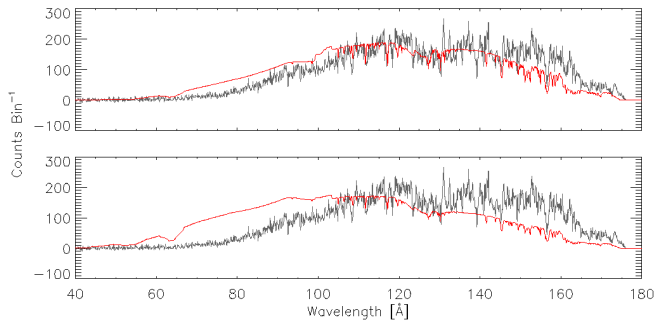


Figure 6.5: *Chandra* spectrum of GD 246 (thin lines) with overplotted best-fit model spectra (thick lines). Top: Homogeneous model with $T_{\text{eff}} = 52000\text{K}$, $\log g = 7.1$. Bottom: Stratified model with $T_{\text{eff}} = 52000\text{K}$ and $\log g = 8.2$. The models include only H and Fe.

higher $\log g$ increases the deviation. A $\log g$ as low as 7.1, however, deviates significantly from the assumed mean value of $\log g = 7.89$. This is unrealistic and not in accordance with the model grid.

6.5.2 Stratified models

For the homogeneous models increasing the effective temperature and decreasing the surface gravity leads to good results. In the case of a stratified atmosphere, a too low $\log g$ results in strong deviations from the observed flux in the higher wavelength ranges ($> 80\text{Å}$). Again a strong surface gravity ($\log g \sim 8.2$) is necessary to prevent iron from levitating in the atmosphere. An overview of the different models in the grid is shown in figure A.5. Not surprisingly, the highest value for $\log g$ so far determined was derived from an *EUVE* analysis with stratified models (Schuh et al. (2002) cf. table 6.1). Varying T_{eff} once again has a comparatively minor impact on the overall structure.

The large number of lines in the *Chandra* spectrum of GD 246 indicates the presence of numerous elements and ions along with an unknown opacity in wavelength ranges not observed by *Chandra*. The X-ray flux is produced in deeper layers and is radiated to the surface. Changes of opacity in intermediate layers therefore determine the actual amount of flux emitted and affect the shape of the emergent spectrum. While fitting the spectrum of LB 1919 with only hydrogen and iron works well, in the case of GD 246 a good agreement between observation and stratified models can hardly be achieved. Obviously a more complex composition of the atmosphere is needed to shift the flux maxima towards higher wavelengths.

Figure 6.5 shows the best fit homogeneous and stratified H/Fe models.

The results of the analysis of the *Chandra* spectra of LB 1919 and GD 246 with models including H and Fe/Ni yields some information about the photospheric properties of the stars. In the next sections the analysis is extended to the *FUSE* and *EUVE* wavelength range to gain additional knowledge. The *Chandra* analysis is then continued in the sections 6.10 and 6.11.

6.6 *FUSE* analysis (LB 1919)

6.6.1 Parameter checkup

Since the analysis of the *Chandra* spectrum of LB 1919 only reveals a lack of iron and nickel, additional hints for occurrence and abundances of other elements are necessary. In order to better reproduce the *Chandra* observation, we gather information about the composition of the atmosphere and check for a possible stratification or current disturbance by an analysis of a *FUSE* spectrum of LB 1919. For the comparison between models and observations the computed flux has been convolved with the spectral resolution of the *FUSE* instrument (0.05 \AA) and scaled to the continuum of the observation.

Before starting to enrich the model atmosphere with different elements and check for their presence in the observation, a checkup for temperature and surface gravity had to be carried out. Previous determinations of those values were rather rare and our preliminary *Chandra* analysis already indicated that the assumed values based on Vennes et al. (1997) might be worth a reconsideration in the given context. For this purpose a grid of pure hydrogen atmospheres with different T_{eff} and $\log g$ was calculated to fit the temperature sensitive hydrogen Lyman lines in the *FUSE* spectral range.

As indicated by the analysis of the *Chandra* spectrum, the *FUSE* spectrum of LB 1919 favors a significantly lower temperature. Instead of the assumed $T_{\text{eff}} = 69000 \text{ K}$, the temperature range is more likely to be $52\text{--}56 \text{ kK}$, $\log g$ still in the range $7.9\text{--}8.5$. Figure 6.6 shows a comparison between a model calculated with the high T_{eff} and a better fitting model with $T_{\text{eff}} = 54000 \text{ K}$. Adding more elements to the atmosphere had no major influence on the line fitting precision.

The influence of the hydrogen column density on the flux shape and on the lines of elements other than hydrogen was investigated considering the relation between reddening and hydrogen column density in the Galaxy by Güver & Özel (2009).

$$N_{\text{H}}(\text{cm}^{-2}) = (6.86 \pm 0.27) \cdot 10^{21} \text{ E(B-V)} \quad (6.1)$$

A hydrogen column density as high as $N(\text{HI}) = 1.6 \cdot 10^{19} \text{ cm}^{-2}$ (Wolff et al. 1998a), corresponds to a reddening of $\text{E(B-V)} = 0.002 \text{ mag}$. This produces an unrecogniz-

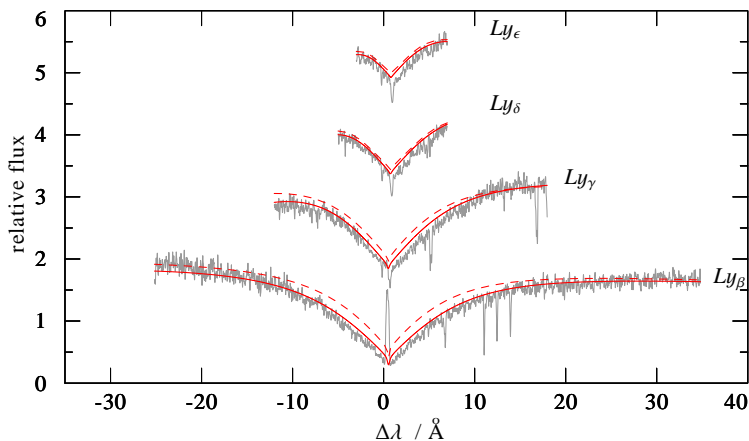


Figure 6.6: Fit to the Lyman lines in the *FUSE* spectrum of LB 1919 (thin line). Overplotted are pure-H models with $T_{\text{eff}} = 54000\text{K}$, $\log g = 7.9$ (thick line), and a model with $T_{\text{eff}} = 69000\text{K}$, $\log g = 7.9$ (dashed line). Models are scaled to fit the local continuum.

able change in the model flux, as do the tentatively applied values of 0.005 and 0.01 mag. In contrast, absorption effects by the *ISM* are noticeable. They become manifest in several interstellar absorption lines which have to be carefully separated from the photospheric features. Since nothing about the atmospheric trace elements of LB 1919 was known, the *FUSE* spectrum was checked for lines of elements known to appear in DA white dwarfs. The elements found in the spectrum of LB 1919 were then included in the calculations successively. As for the *Chandra* range, models with a homogeneous mixture of elements in the atmosphere as well as stratified atmospheres were calculated and compared. The model grid contains the temperatures $T_{\text{eff}} = 52\text{--}56\text{ kK}$ in steps of 2000 K and gravities $\log g = 7.9\text{--}8.5$ in steps of 0.3 dex. Again the abundances in the following analysis are given in number ratios relative to hydrogen unless stated otherwise.

6.6.2 Elements and abundances

Two C III features are visible in the *FUSE* spectrum of LB 1919, a singlet at 977.03 \AA and a triplet around $\sim 1175\text{ \AA}$. For the determination of the carbon abundance the singlet is excluded, since it contains a significant interstellar contribution. The carbon triplet can be successfully reproduced with an abundance of $4.63 \cdot 10^{-7}$. This abundance provides a good agreement for most of the temperatures and surface gravities in the model grid $T_{\text{eff}} = 54 \pm 2\text{ kK}$ and $\log g = 8.2 \pm 0.3$ (see figure B.1). For $T_{\text{eff}} = 56000\text{K}$ the abundance can be reduced slightly for a

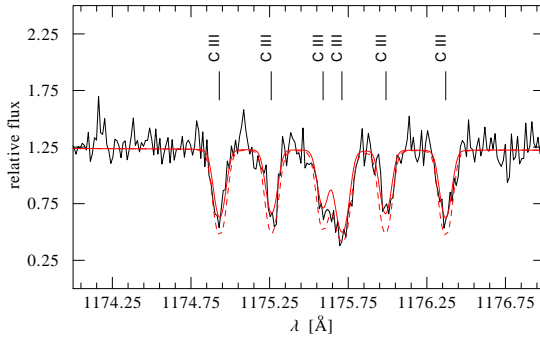


Figure 6.7: Homogeneous (thick line) and stratified (dashed line) model with $T_{\text{eff}} = 52\,000\text{ K}$ and $\log g = 8.5$, fitting the C III triplet in the *FUSE* spectrum of LB 1919 (thin line). The C abundance in the homogeneous model is $\text{C}/\text{H} = 4.63 \cdot 10^{-7}$.

better match giving an error for the abundance of $2.5 \cdot 10^{-7}$ (see also figure B.13).

The self-consistently calculated abundance of the stratified models is satisfactory. Since these models calculate the abundances for every depth of the atmosphere a single abundance value can not easily be given. One possibility is to take the abundance at $\tau_{\text{ross}} = 2/3$ as a representative value (Chayer et al. 1995b). Another way is to fit the suitable stratified model spectra with homogeneous model spectra and determine the abundances of the best fitting homogeneous model (Dreizler 1999b). In order to determine, whether the stratified models are suitable in reproducing the spectral lines, however, only a relative description of the line strength has to be given. Small variations with changing gravity can be detected. The best result can therefore be achieved for the highest value of $\log g = 8.5$. A lower gravity results in an excessively high abundance and too strong C III lines. Figure 6.7 shows a nicely fitting stratified model with the corresponding one calculated with a homogeneous mixture of elements. The dependence of the stratified models on T_{eff} and $\log g$ can be studied in detail in figure B.2.

The abundance of oxygen can only be roughly estimated. The O VI resonance doublet at 1031.91 \AA and 1037.61 \AA is visible. They are blended by an interstellar O VI doublet. No other oxygen feature can be identified. Consequently, only an upper limit of $4 \cdot 10^{-6}$ for the oxygen abundance in LB 1919 can be estimated.

The stratified models predict a low oxygen abundance for $\log g > 7.9$, hence an almost unrecognizable line feature, suggesting that the major part of the visible line is contributed by the ISM (see figure B.4).

Several lines of Si in ionization stage IV are visible, located at 1066.63 \AA , 1122.48 \AA , and 1128.33 \AA . Additionally a Si III triplet around 1109.97 \AA can be

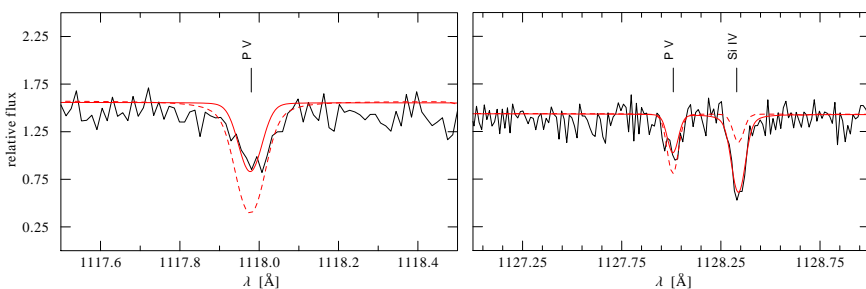


Figure 6.8: Homogeneous (thick line) and stratified (dashed line) model fitting lines of P V and Si IV in the *FUSE* spectrum of LB 1919 (thin line). The abundances in the homogeneous models for temperatures $T_{\text{eff}} = 54 \pm 2\text{kK}$ and $\log g = 8.2 \pm 0.3$ are $\text{Si}/\text{H} = 1.2 \cdot 10^{-7}$ and $\text{Si}/\text{H} = 3 \cdot 10^{-9}$. The predicted diffusion abundance for P is almost in agreement with the observation for $T_{\text{eff}} = 52000\text{K}$ and $\log g = 8.5$. The mismatch of the Si line for these parameters is obvious. See text for details.

seen. The Si lines in the spectrum are free from interstellar contamination. An abundance of $1.2(\pm 0.2) \cdot 10^{-7}$ provides a good fit for the Si IV lines and all temperatures and gravities in the model grid (see figures B.6 and B.14). The Si III lines are much weaker. Therefore they cannot that easily be used for an abundance estimate. Nevertheless, they agree with the determined abundance, preferring the high $\log g$ and low T_{eff} (compare figure B.13).

In the case of silicon the stratified models fail to predict a suitable abundance. The modeled lines are too weak for any temperature and gravity in the grid. The best fit can be achieved for $\log g = 7.9$. This value, however, is still high enough to effectively counteract the weak radiative forces on the silicon atoms. A possible explanation for these weak radiative forces is the still imperfect model atom of silicon used in the calculations. The radiative acceleration of the model atoms strongly depends on the number of radiative bound-bound transitions incorporated. More exact results can therefore be expected for bigger model atoms e.g. oxygen.

The P V resonance doublet appears in the spectrum at 1117.98 \AA and 1118.01 \AA . The lines strength does not vary much with temperatures and $\log g$ (see figure B.6). The abundance for models with homogeneously mixed elements is $3(\pm 1) \cdot 10^{-9}$ for $T_{\text{eff}} = 54 \pm 2\text{kK}$ and $\log g = 8.2 \pm 0.3$ (compare figure B.16).

The fits for the stratified models are not completely satisfying. For a wide range of T_{eff} and $\log g$ the lines are too strong to fit the observation. An acceptable fit can only be achieved for the lowest temperature ($T_{\text{eff}} = 52000\text{K}$) and highest $\log g$ (8.5), contrary to the tendency shown by the silicon lines. A too undetailed phosphorus model atom is this time more unlikely to explain the strong lines. For

an expanded one we would expect a higher radiative force caused by the higher amount of bound-bound transitions and along with it an even higher abundance of phosphorus. Nevertheless, unpredictable interdependencies between different elements are possible. A way to match the line profiles of both elements is to take a low temperature around $T_{\text{eff}} = 52000\text{ K}$ and a $\log g$ as high as $\log g = 8.5$ for granted to explain the phosphorus abundance. The too low silicon abundance for these T_{eff} and $\log g$ might then be attributed to the insufficient model atom (compare figure 6.8).

Sulfur appears in different ionization stages. A S IV triplet can be seen in the observed spectrum at 1062.66 \AA , 1072.96 \AA , and 1073.508 \AA . Questionable is the existence of an S V line at 924.22 \AA . It is very weak at best. A S VI resonance doublet appears at 933.38 \AA and 944.52 \AA . One of the components can be confused with an interstellar Ni II line, identified for example in the FUSE spectrum of the white dwarf PG 1342+444 at 944.37 \AA (Barstow et al. 2002). However, the appearance of the second component makes it more likely that it is a slightly shifted S VI line in both cases, which can also be seen in the model atmospheres. A fit to the most clearly visible S IV lines gives a sulfur abundance of $1(\pm 0.5) \cdot 10^{-7}$ (figure B.19) for $T_{\text{eff}} = 54 \pm 2\text{ kK}$ and $\log g = 8.2 \pm 0.3$ (cf. figure B.9). A fit to the S VI lines favors a slightly lower abundance (see figure B.10).

The stratified models fit the observations best for $\log g = 8.5$ but contrary to the case of phosphorus a high temperature ($T_{\text{eff}} = 56000\text{ K}$) is needed (cf. figure 6.9). Lowering the temperature requires as well $\log g = 8.2$ to maintain an appropriate fit. A value of $\log g = 7.9$ however is too low to match the observation for the given temperatures (figure B.9).

Since the *Chandra* spectrum of LB 1919 did not reveal any significant iron or nickel lines, the expectations for the *FUSE* range were even lower. Most of the lines of the higher ionization stages of iron and nickel expected to appear in a hot white dwarf like LB 1919 lie in the X-ray range, for which reason the *Chandra* observation was taken. As a matter of fact, no iron or nickel lines can be seen in the *FUSE* spectrum. Thus, the maximum abundances of iron and nickel, if existent in the atmosphere at all, can only be roughly estimated. The strength of the iron lines in the case of a homogeneous distribution in the atmosphere does not vary much within temperatures of $T_{\text{eff}} = 54 \pm 2\text{ kK}$ and $\log g = 8.2 \pm 0.3$. Thus, within these margins detectable lines are merely affected by changing abundances. The maximum amount of Fe can be expected for $T_{\text{eff}} = 56000\text{ K}$ and $\log g = 7.9$. For these parameters, an enhanced amount of iron would lead to lines clearly recognizable in the *FUSE* spectrum at an abundance $\text{Fe}/\text{H} > 1.25 \cdot 10^{-5}$. Any lower abundance would disappear in the noise of the observation.

A calculated stratified model atmosphere with hydrogen and iron is more sensitive to changes in T_{eff} and $\log g$. Thus, for the maximum amount of iron possible

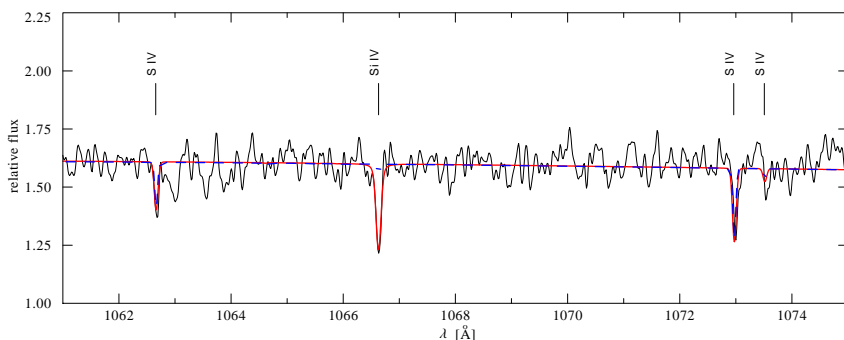


Figure 6.9: Detail of the *FUSE* spectrum of LB 1919 (thin line). Homogeneous (thick line) and stratified (dashed line) model with $T_{\text{eff}} = 52000\text{K}$ and $\log g = 8.5$, fitting lines of S IV and Si IV. Contrary to phosphorus for the stratified model a high temperature is needed to fit the sulfur feature.

a high temperature for the radiative acceleration and a low $\log g$ to prevent the gravitational settling are needed. The model calculated with $T_{\text{eff}} = 56000\text{K}$ and $\log g = 7.9$ reproduces the spectrum well. The abundance is low enough and no Fe lines are detectable.

In the case of nickel the situation for both homogeneous and stratified models is similar. In the first case any abundance higher than $\text{Ni}/\text{H} > 1.25 \cdot 10^{-5}$ would produce nickel lines strong enough to be visible in the observation for $T_{\text{eff}} = 56000\text{K}$ and $\log g = 7.9$. These parameters provide the maximum amount of nickel possible in the stratified model atmospheres. But even this amount is too low to fit the observation and produce no detectable lines.

It should be pointed out that the abundances for iron and nickel estimated above are the upper limit for the analysis of the *FUSE* spectrum and it is more likely that the abundances are much lower (cf. subsection 6.3.1).

6.7 *FUSE* analysis (GD 246)

6.7.1 Parameter checkup

The values for effective temperature and surface gravity for GD 246 have been determined numerous times (cf. table 6.1) and contrary to LB 1919 different elements and their abundances have been determined. Nevertheless, a first parameter checkup was performed to continue the analysis of the *FUSE* spectrum on a solid basis. Similar to the analysis of the *Chandra* spectrum, first a grid of hydrogen model spectra around the mean values for T_{eff} and $\log g$ of table 6.1 was used to fit

the hydrogen Lyman lines.

The results show that the temperature is very likely to be in the range 57 ± 2 kK and $\log g$ between 7.3–7.9. These values do not deviate significantly from the ones previously determined. The temperature is slightly higher than originally expected, hence higher than the newly determined value for LB 1919. For the analysis of the element abundances a grid of models with temperatures between 52–59 kK and $\log g$ as given above was calculated and elements with detectable lines in the spectrum were added analogously to the approach for LB 1919.

The effect of hydrogen column density on the spectrum of GD 246 was investigated using again equation 6.1. Taking $N(\text{HI}) = 1.8 \cdot 10^{19} \text{ cm}^{-2}$ (Wolff et al. 1998a) leads to a reddening of $E(\text{B}-\text{V}) = 0.002 \text{ mag}$, with no detectable influence on the model flux. For a confirmation, a *Hubble Space Telescope (HST)* spectrum of GD 246 was taken from the *Multimission Archive at STScI (MAST)* (<http://archive.stsci.edu/index.html>). Reddening and hydrogen column density have been applied to the models and compared to the observed flux. Again the expected reddening of 0.002 mag does not change the calculated flux. Only enhancing to 0.05 and 0.1 mag respectively lowers the model flux significantly. This, however, contradicts the observation. For the estimation of effects caused by interstellar matter, interstellar lines have been modeled with the *OWENS* code and applied to the spectrum, in order to simplify the identification of possible photospheric features. A number of lines can be found in the *FUSE* spectrum of GD 246, including elements and ionization stages appearing in LB 1919.

6.7.2 Elements and abundances

While the C III triplet was the most compulsive indicator for the abundance determination in LB 1919, it is missing in GD 246. The only carbon feature appearing is the singlet at 977.03 Å. As before, the significant interstellar contribution of the line disqualifies it for the abundance determination. Still an upper limit for the abundance of carbon can be given. Any value higher than $> 3.2 \cdot 10^{-8}$ would result in a detectable carbon triplet around $\sim 1175 \text{ Å}$ for 57 ± 2 kK and $\log g = 7.6 \pm 0.3$ (see figure B.3).

All stratified models computed for GD 246 show carbon features that are clearly too strong to match the observation. For some reason the carbon abundance of GD 246 is unexpectedly low and cannot be explained by a model assuming equilibrium between radiation and gravitational forces.

As mentioned before in the analysis of LB 1919, the *FUSE* spectrum of GD 246 does not show clear features of the O VI resonance doublet at 1031.91 Å and 1037.61 Å. This is a hint that the main contribution of the observed lines in the spectrum of LB 1919 comes from the interstellar resonance lines at the same posi-

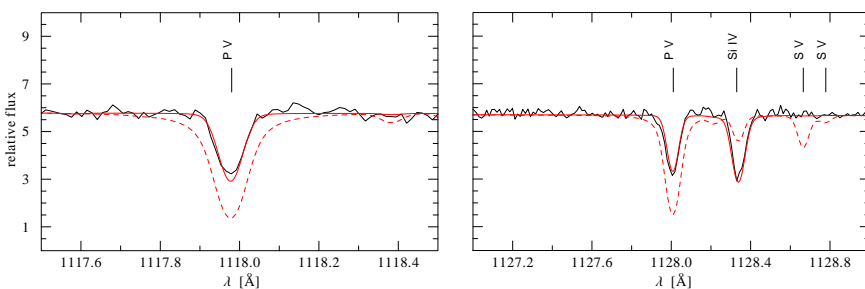


Figure 6.10: Fit to the P V and Si IV lines of GD 246 (thin line) with a homogeneous (thick line) and a diffusion (dashed line) model. The parameters are in both cases $T_{\text{eff}} = 55000\text{ K}$ and $\log g = 7.9$. The abundances in the homogeneous models are $\text{Si} = 1.2(\pm 0.2) \cdot 10^{-7}$ and $\text{P} = 4(\pm 2) \cdot 10^{-9}$. The S V lines, which are predicted by radiative levitation, can not be seen in the observation.

tion (see figure B.4 for oxygen in LB 1919). Again an upper limit for the oxygen abundance in GD 246 can be given: $\text{O} < 6 \cdot 10^{-8}$ (figure B.5).

The diffusion models in the calculated grid predict an extremely high oxygen abundance resulting in strong lines. As seen in the case of LB 1919, a low oxygen abundance in a stratified atmosphere requires a $\log g$ higher than 7.9, hence higher than the most likely gravity determined by the Lyman line fits.

Silicon is present in GD 246 in ionization stage IV. Namely at 1122.48 \AA and 1128.33 \AA . The line strength does not show recognizable variations for the different temperatures and $\log g$ in the model grid (see figure B.7). A satisfying fit can be obtained for an abundance of $\text{Si} = 1.2(\pm 0.2) \cdot 10^{-7}$ (see figure B.14). This value is identical to the value determined by Barstow et al. (2003b).

The diffusion models show the same behaviour known from LB 1919. The Si lines are consistently too weak and prefer a lower $\log g$. The minimum $\log g$ in the grid for GD 246 is lower than in the case of LB 1919. Therefore, fitting the GD 246 Si IV lines results in a better agreement compared to LB 1919.

Fitting the P V resonance lines at 1117.98 \AA and 1128.01 \AA gives an abundance of $\text{P} = 4(\pm 2) \cdot 10^{-9}$, suitable for $57 \pm 2\text{ kK}$ and $\log g = 7.6 \pm 0.3$ (see figures B.17 and B.18).

An abundance too high is predicted for phosphorus in the stratified case. In this case it can not be reduced completely by varying the surface gravity to achieve a better match since the $\log g$ of 7.9 is not sufficiently high (figure B.7).

The main focus of attention for the determination of the sulfur abundance lies on the S VI resonance doublet at 933.38 \AA and 944.52 \AA (cf. section 6.6). No further sulfur lines can be identified and consequently the abundance for sulfur deduced

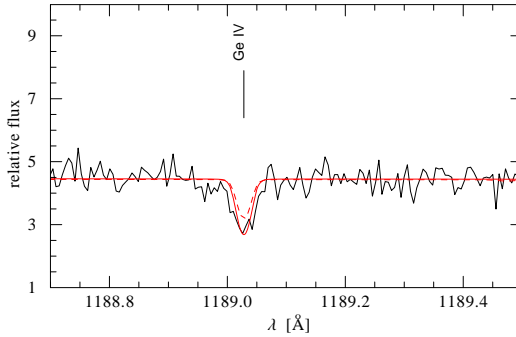


Figure 6.11: Fit to the Ge IV line in the *HST* spectrum of GD 246 (thin line). Overplotted is a model with an atmosphere of homogeneously mixed elements (thick line) and a model with a stratified atmosphere that was calculated for the first time with a Ge model atom (dashed line). Both models are calculated with $T_{\text{eff}} = 55000\text{K}$ and $\log g = 7.3$, which are the best fitting parameters for the diffusion model. The Ge abundance in the homogeneous model is $\text{Ge} = 5(\pm 1) \cdot 10^{-9}$.

from these lines is as low as $S = 5(\pm 2) \cdot 10^{-9}$ for $57 \pm 2\text{kK}$ and $\log g = 7.6 \pm 0.3$ (figure B.20).

The stratified models produce excessively strong lines and behave in the same way as described for LB 1919 (again cf. section 6.6). As for phosphorus, the optimum $\log g$ to fit the sulfur lines is larger than 7.9. Figure 6.10 shows lines of P V, Si IV and S V in the observation and in the overplotted models for selected values of T_{eff} and $\log g$ to illustrate their behavior. An overview of the dependence of the line on the different T_{eff} and $\log g$ can be found in figure B.11.

Contrary to LB 1919 a large amount of iron lines could be identified in the *Chandra* spectrum of GD 246 and an estimate for the abundance of Fe and Ni could be derived. No lines of iron and nickel can be seen in the *FUSE* spectrum of GD 246. Thus the determination of an upper limit for the abundances of iron and nickel in the ultraviolet spectral range can be regarded as an additional constraint to the X-ray analysis. Indeed the models with homogeneously mixed iron in the atmosphere show that any abundance higher than $1 \cdot 10^{-6}$ would result in detectable lines in the spectrum for $T_{\text{eff}} = 59000\text{K}$ and $\log g = 7.9$, which is only slightly lower than the value found at the analysis of the *Chandra* spectrum ($\text{Fe}/\text{H} = 1.25 \cdot 10^{-6}$). The same can be said for the nickel abundance. A maximum value of $\text{Ni} = 1 \cdot 10^{-6}$ is in good agreement with the one determined before ($< 1 \cdot 10^{-6}$).

In the case of a stratified atmosphere the flux produced by a model including iron and nickel contradicts the observation. For all model parameters line features are clearly seen, which indicates that too much iron and nickel are predicted for

the different $\log g$ in the grid. This is a tendency already noticed for phosphorus, oxygen and sulfur.

Following Vennes et al. (2005), the analysis of photospheric lines of elements in GD 246 was expanded to the spectral range of the *HST* to check for Ge IV at 1188.99 Å and 1229.81 Å. The first component is clearly detectable and a fit to the line yields an abundance of $5(\pm 1) \cdot 10^{-9}$ for 57 ± 2 kK and $\log g = 7.6 \pm 0.3$. The second component is much weaker and not detectable. The awareness of the existence of germanium in white dwarfs is rather new. No detailed NLTE model atoms are available yet. Thus the model atom used is based largely on the similarly configured carbon and focused on the identification of the expected Ge IV lines. A detailed description of the model atom can be found in chapter 5.

For the first time Ge was included in the self-consistent diffusion calculations. However, the stratified models demonstrate a strong dependency on accurate and capacious atomic data (cf. Landenberger-Schuh 2005 and chapter 5). This could be the reason why the predicted abundances for Ge IV does not provide a satisfying fit for all values of T_{eff} and $\log g$. They fit good for $T_{\text{eff}} = 55000$ K and $\log g = 7.3$. For other parameters model and observation are not in accordance (see figure B.12). Figure 6.11 shows the best fit for the diffusion model together with a homogeneous model with the same parameters.

The determined abundances for LB 1919 and GD 246 from the analysis of the *FUSE* spectrum for the homogeneous models as well as a tendency for the line fitting with the stratified model atmospheres can be found in table 6.2.

Table 6.2: Element abundances (number ratio relative to hydrogen) for LB 1919 and GD 246 as determined from the *FUSE* and *HST* spectra with homogeneous models with 54 ± 2 kK and $\log g = 8.2 \pm 0.3$ for LB 1919 and 57 ± 2 kK and $\log g = 7.6 \pm 0.3$ for GD 246 with estimated uncertainties. The identified ions of the elements are noted in the fifth column. The sixth column illustrates the tendency of the self-consistently calculated abundance of a diffusion model to be stronger ($>$) or weaker ($<$) than the observed line strength or to match the observation ($=$). Literature values for the abundances are shown in the seventh column. The solar abundances taken from Asplund et al. (2009) can be found in the last column.

WD	Element	Abundance [X/H]	Uncertainty	Ions	Diff	Literature	Solar
LB 1919	C	$4.63 \cdot 10^{-7}$	$2.5 \cdot 10^{-7}$	C III	=		$2.69 \cdot 10^{-4}$
	O	$4 \cdot 10^{-6}$		O VI	$>?$		$4.9 \cdot 10^{-4}$
	Si	$1.2 \cdot 10^{-7}$	$2 \cdot 10^{-8}$	Si III+IV	$<$		$3.24 \cdot 10^{-5}$
	P	$3 \cdot 10^{-9}$	$1 \cdot 10^{-9}$	P V	$>$		$2.57 \cdot 10^{-7}$
	S	$1 \cdot 10^{-7}$	$5 \cdot 10^{-8}$	S IV+VI	$>?$		$1.32 \cdot 10^{-5}$
GD 246	C	$< 3.2 \cdot 10^{-8}$		C III	$>$		
	O	$< 6 \cdot 10^{-8}$		O VI	$>$	$1.6 \cdot 10^{-7}$ Barstow et al. (2003b)	
	Si	$1.2 \cdot 10^{-7}$	$2 \cdot 10^{-8}$	Si IV	$<$	$5.0 \cdot 10^{-8}$ Wolff et al. (2001)	
						$3.2 \cdot 10^{-8}$ Chayer et al. (2001)	
						$1.2 \cdot 10^{-7}$ Barstow et al. (2003b)	
	P	$4 \cdot 10^{-9}$	$2 \cdot 10^{-9}$	P V	$>$	$6.3 \cdot 10^{-9}$ Chayer et al. (2001)	
						$7.5 \cdot 10^{-9}$ Wolff et al. (2001)	
	S	$5 \cdot 10^{-9}$	$2 \cdot 10^{-9}$	S VI	$>$	$< 3.0 \cdot 10^{-6}$ Wolff et al. (2001)	
	Ge	$5 \cdot 10^{-9}$	$1 \cdot 10^{-9}$	Ge IV	$<$	$2.5 \cdot 10^{-9}$ Vennes et al. (2005)	$4.67 \cdot 10^{-9}$
Fe	$< 1 \cdot 10^{-6}$			$>$	$< 2.0 \cdot 10^{-5}$ Wolff et al. (2001)	$3.16 \cdot 10^{-5}$	
					$3.0 \cdot 10^{-7}$ Vennes & Dupuis (2002)		
Ni	$< 1 \cdot 10^{-6}$			$>$		$1.66 \cdot 10^{-6}$	

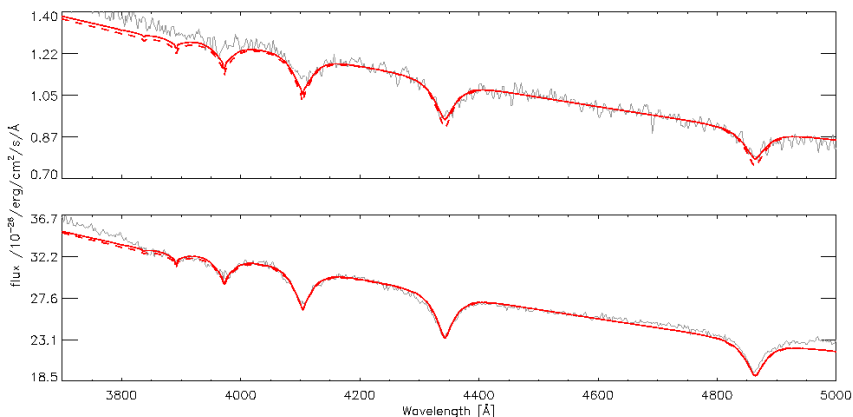


Figure 6.12: Fit to the Balmer lines of LB 1919 (top panel) and GD 246 (bottom panel). The *UVES* spectrum (thin line) is overplotted with a model atmosphere (thick line) including all elements found in the *FUSE* spectrum and models with pure H atmospheres (dashed line). The parameters of the model for LB 1919 are $T_{\text{eff}} = 54000$ K and $\log g = 7.9$, for GD 246 $T_{\text{eff}} = 55000$ K and $\log g = 7.90$.

6.8 Optical constraint

The analysis of the *FUSE* spectrum in the previous section was based on a model grid with temperatures and surface gravities determined by a fit to the Lyman lines. This information about the chemical composition of the atmospheres of LB 1919 and GD 246 can now be taken to continue the analysis in other wavelength ranges. The spectra in the *EUVE* wavelength range are strongly determined by the chosen values of T_{eff} and $\log g$. For a verification of these parameters therefore the Balmer lines in an *Ultraviolet and Visual Echelle Spectrograph (UVES)* spectrum were investigated. The spectra of LB 1919 and GD 246 were taken in the framework of the *ESO SN Ia Progenitor survey (SPY, Napiwotzki et al. 2001)*.

The model fluxes are convolved with a FWHM of 2.5 \AA and scaled to the continuum of the observation. The determined values for T_{eff} and $\log g$ result in model spectra with hydrogen Balmer lines that are in agreement with the observed ones in the optical wavelength range.

For LB 1919 the best fit can be achieved for $T_{\text{eff}} = 54000$ K and $\log g = 7.9$. A higher $\log g$ results in a slightly broader line. For other temperatures the modeled lines become to strong (cf. figure C.1). The GD 246 observation can best be fitted with $T_{\text{eff}} = 55000$ K and $\log g = 7.9$ (figure C.2). For both stars small deviations

due to an inaccurate calibration can be seen. This effect can be disregarded, since it affects the lines only partly.

The models used for the fits to the *UVES* observation contain all elements identified in the *FUSE* analysis. However, the fits do not deviate significantly if pure hydrogen models are used instead. This can be seen in figure 6.12. It shows the *UVES* spectra of LB 1919 and GD 246 together with two model atmospheres with parameters determined by the *FUSE* analysis. One model is calculated with the heavy elements, the other one with a pure H atmosphere. With this additional constraint on the temperatures and surface gravities used so far, it can be proceeded with the analysis of the *EUVE* spectrum of the two objects to gain more information.

6.9 *EUVE* analysis

6.9.1 LB 1919

The main motivation behind the attempt to analyze X-ray spectra of LB 1919 was the goal to identify lines of individual elements, which could give insight to the composition of the atmosphere. To account for the opacity affecting the shape of the SED, sometimes a metal index, i.e. a photospheric parameter-dependent quantity, is introduced (Landenberger-Schuh 2005). The attempt to explain the properties of the atmosphere of LB 1919 by calculating stratified atmospheres with the use of this metal index failed. The calculations yielded a model flux too low to match the observed *EUVE* spectrum of LB 1919. Obviously the opacity, offered by the assumed metal index, exceeded considerably the one existing in reality. Figure 6.13 shows the spectrum of LB 1919 and a stratified model, which was calculated with a metallicity scaled relative to the one of the well studied G191-B2B. Taking the definition of (Landenberger-Schuh 2005) for the metal index,

$$mi = 4 \cdot 10^{-12} \cdot T_{\text{eff}}^4 / [K^4 s^2 / \text{cm}], \quad (6.2)$$

gives a scaling factor of $mi = 0.6$ for LB 1919 compared to G 191-B2B.

The model atmospheres obtained by combining the information provided by the analysis of the *Chandra* and *FUSE* spectra of LB 1919 on the other hand, include only those elements and abundances, which are observable directly in the spectra of the star. These are the elements and abundances noted in table 6.2. A comparison of the *EUVE* spectrum of LB 1919 with the so calculated stratified models therefore yields a good opportunity to check their accuracy. Also using additionally atmospheres with a homogeneous mixture of elements offers a way to check the possibility that the equilibrium between radiative and gravitational

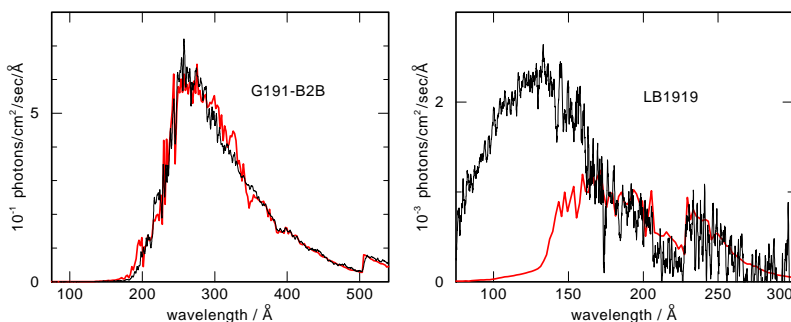


Figure 6.13: *EUVE* spectra of G191-B2B (left) and LB 1919 (right). The observed spectra (thin lines) are compared to stratified model spectra (thick lines). The spectrum of LB 1919 cannot be explained by a metallicity scaled relative to the one of G191-B2B. Picture taken from Werner et al. (2007).

forces is currently disturbed, which cannot be excluded completely by the previous analysis.

The effect of the *ISM* on the flux in the EUV range is very strong. Energy is absorbed by bound-free transitions of H I, He I, and He II. The edges of those absorption processes are located at 911.7 \AA , 504.3 \AA , and 227.8 \AA , respectively. Thus, knowledge of the ionization fractions resulting from the column densities towards the star are of major importance. Wolff et al. (1998a) described a procedure for incorporating the *ISM* absorption. The synthetic spectra are first normalized to the visual magnitude and the interstellar absorption is calculated according to Rumph et al. (1994). The input column densities can then be adjusted by keeping fixed values for T_{eff} and $\log g$. Landenberger-Schuh (2005) adopted the values for the H I column densities from Wolff et al. (1999) for the analyzed stars including LB 1919 whenever possible. The effect of He I and He II column densities plays an important role only at longer wavelengths ($\lambda \gtrsim 160 \text{ \AA}$) and could therefore be partially separated from the analysis of the photospheric influence on the spectra.

The shape of the SED in the *EUVE* spectral range depends on the interstellar hydrogen and helium column densities. For the varying temperatures and surface gravities in the following analysis at first fixed values for these column densities were chosen in order to study solely the effects of changes in the stellar parameters on the *EUVE* spectrum. If not noted otherwise, the values for the column densities are equal to $N(\text{H I}) = 1.6 \cdot 10^{19} \text{ cm}^{-2}$, $\text{He I/H I} = 0.04$, and $\text{He II/H I} = 0.05$, taken from Landenberger-Schuh (2005). The visual magnitude of LB 1919 is 16.8 (Schwope et al. 2000).

For the stratified atmospheres in the used T_{eff} and $\log g$ grid (see section 6.6) and

with the identified elements the results are intuitive. The higher $\log g$, the higher the amount of atoms forced to settle in the atmosphere. Thus, the opacity is lower and the flux is rising. The temperature again has only a minor impact, although a higher temperature causes a slightly higher flux. Consequently, the best fit can be achieved with $T_{\text{eff}} = 56000 \text{ K}$ and $\log g = 8.5$. Overall however, the model flux is not reaching the maximum of the observation at wavelengths $< 200 \text{ \AA}$. The top right panel in figure 6.14 shows an example of three diffusion models with varying $\log g$.

Adjusting the temperature to a higher level, namely 58000 K and 60000 K , and keeping $\log g$ fixed at 8.5 therefore does not lead to a visible improvement (compare figure 6.14, bottom left panel). Moreover, a temperature value much higher than 60000 K contradicts the results from the Lyman line fitting in the *FUSE* spectrum and the fits to the Balmer lines in the *UVES* spectrum and should be carefully dealt with, in order to avoid unrealistic overestimations. Fixing the temperature and raising the surface gravity to $\log g = 8.8$ results in a better fit (figure 6.14, bottom right panel). Again, this is unrealistic for the above mentioned reasons.

The homogeneous models fail in reproducing the *EUVE* spectrum, even though they do not possess any opacity coming from elements with no detectable lines in the observation. Here the temperature is the most compelling parameter affecting the flux. The higher the value, the lower the deviation from the observation. Changes to higher $\log g$ raise the flux only marginally. Nevertheless, the calculated flux of all model atmospheres is far too low to provide a satisfactory fit. Figure 6.14 shows the dependence of the homogeneous models on the surface gravity in the top left panel. Apparently, the opacity generated by absorbers in the atmosphere of LB 1919 in both, stratified and homogeneous models, is still too large. In the case of the diffusion models, this appears to be rather unexpected, since the abundances are calculated self-consistently on physical grounds. For a homogeneous model yet a wrong determined abundance could account for additional absorption.

The abundances for most of the identified elements in LB 1919 are well established by the analysis of the *FUSE* spectrum. For oxygen only an upper limit could be given (cf. section 6.6). Reducing oxygen by a factor of 10 in the homogeneous models in fact raises the flux considerably, though still not enough to match completely. Reducing oxygen further or removing it completely from the calculations does not change the flux shape furthermore.

Even though for the diffusion models the amount of oxygen floating in the atmosphere is limited, its bare existence could correspond to unobservable opacity. Thus removing oxygen completely from the diffusion calculations eliminates any oxygen induced absorption. As for the homogeneous models, an effect is noticeable. The oxygen-free models show a better agreement. Figure 6.15 shows the effect of removing oxygen from the diffusion calculations for a model with

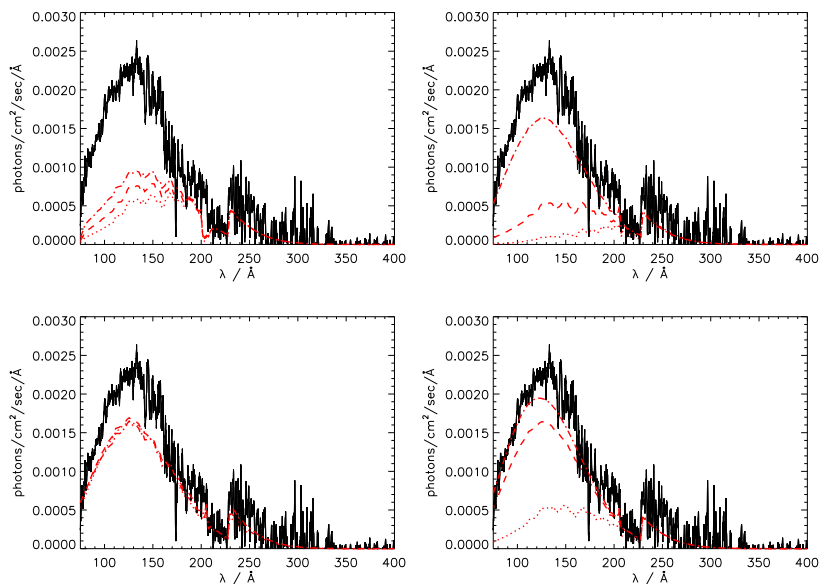


Figure 6.14: EUVE spectrum of LB 1919 (solid line) with overplotted model atmospheres. All models include H,C,O,Si,P and S with abundances according to table 6.2. Top left: Homogeneous models with $T_{\text{eff}} = 56000\text{K}$ and $\log g = 7.9$ (dotted), $\log g = 8.2$ (dashed), and $\log g = 8.5$ (dash dot). Top right: Diffusion models with same parameters. Bottom left: Diffusion models with $\log g = 8.5$ and $T_{\text{eff}} = 56000\text{K}$ (dotted), $T_{\text{eff}} = 58000\text{K}$ (dashed), and $T_{\text{eff}} = 60000\text{K}$ (dash dot). Bottom right: Diffusion models with $T_{\text{eff}} = 56000\text{K}$ and $\log g = 8.2$ (dotted), $\log g = 8.5$ (dashed), and $\log g = 8.8$ (dash dot).

$T_{\text{eff}} = 56000\text{K}$ and $\log g = 8.5$. Even though the fit improves, some flux is still be missing. Evidently the oxygen abundance alone can not be responsible for the lack of flux in the lower wavelength range.

Considering the analysis of the FUSE spectrum two things should be noted. Even though the elimination of oxygen is improving the fit slightly its abundance was at least predicted to be very low and matched the FUSE observation. The predicted abundances of other elements like silicon and phosphorus on the other hand, did not produce lines of an adequate strength and were either too weak (Si) or too strong (P). A computational or conceptual inaccuracy of the diffusion code or the underlying physics producing the difference in the line strengths could also be the cause for the failure to fit the flux in the EUV.

For that reason the self-consistently calculated abundance of the elements in ev-

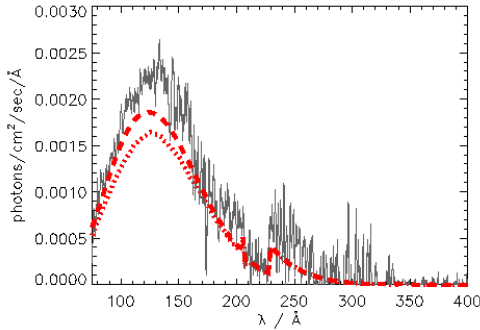


Figure 6.15: *EUVE* spectrum of LB 1919 (solid line). Overplotted a diffusion model with H,C,O,Si,P and S as well as $T_{\text{eff}} = 56000\text{K}$ and $\log g = 8.5$ (dotted) and a model with the same parameters but calculated without oxygen (dashed). A higher SED is recognizable.

ery depth of the diffusion model was manipulated in order to produce line strengths, which provide a good fit to the *FUSE* observation. Based on these new *hand-made* diffusion abundances the effect on the SED of the *EUVE* spectrum was investigated starting with a modified abundance for the low predicted silicon. This investigation is done for fixed values of T_{eff} and $\log g$. The comparison between effects of changed diffusion abundances on the spectra in the *FUSE* and *EUVE* on the other hand does not depend on the specific values chosen, since these abundances are adjusted to fit the spectral lines of the element for this set of parameters.

Raising the abundance of silicon to a value five times and ten times higher than originally predicted, does neither influence sufficiently the line strength of the features in the *FUSE* spectrum nor the flux shape in the EUV range. Changing the abundance to 15 times the initial one, however, results in a good agreement for the line fit in the far ultraviolet. The increased abundance does not lead to a better fit of the flux in the EUV range, so that the maximum of the observed flux again can not be reached.

The effect of a changed abundance of phosphorus for the same parameters are insignificant as noticed for silicon. A good fit to the *FUSE* spectrum requires an abundance 5 times smaller than predicted and does not affect the flux in the EUV range. Figure 6.16 shows the improved fit for the manipulated diffusion abundances for Si and P on the *FUSE* spectrum as well as the unrecognizable influence on the SED in the *EUVE* wavelength range. Manipulation of the lines of sulfur in a similar way and reducing oxygen still does not lead to a better agreement.

Thus, diffusion abundances, which are potentially calculated inaccurately, can

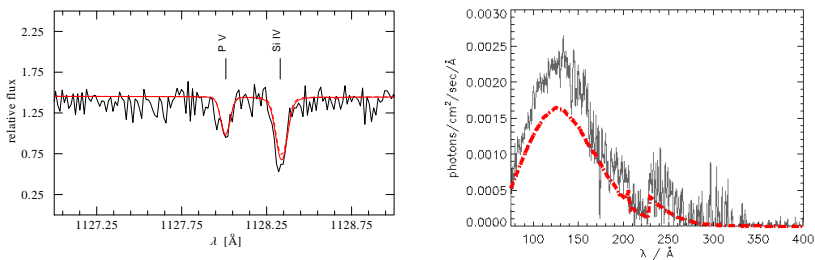


Figure 6.16: Left: Phosphorus and silicon lines in the *FUSE* spectrum (thin line). Overplotted a model with $T_{\text{eff}} = 56000$ K, $\log g = 8.5$ and a homogeneous mixture of elements (thick line) and a diffusion model with the same parameters and a modified abundance output to fit the spectral lines (dashed line). Right: *EUVE* spectrum (solid line) and overplotted diffusion models with same T_{eff} and $\log g$ and abundances as calculated by the code (dotted) and modified abundances (dashed). No recognizable deviations can be found.

not be made responsible for the lack of flux in the EUV wavelength range. Furthermore it should be mentioned that the manipulation of the predicted diffusion abundance output has to be done with caution. Reducing oxygen to a minimum in the model and completely excluding it in the diffusion calculations are two different things. In the first case, it can still account for interactions with the other atoms in the atmosphere and influence the whole stratification of other elements, while in the second case only the opacity provided by oxygen itself is disregarded.

As it was the case for the *Chandra* and the *FUSE* spectra, the analysis of the spectrum of GD 246 offers the opportunity to look for additional hints.

6.9.2 GD 246

The analysis of GD 246 is carried out in the steps mentioned before for LB 1919. Again the values used initially for the hydrogen and helium column densities are taken from Landenberger-Schuh (2005): $N(\text{HI}) = 1.8 \cdot 10^{19} \text{cm}^{-2}$, $\text{He I}/\text{HI} = 0.05$, and $\text{He II}/\text{HI} = 0.03$. The visual magnitude of GD 246 is 13.1 (Pounds et al. 1993). In the previous analysis of the *EUVE* spectrum of GD 246, Landenberger-Schuh (2005) achieved a better agreement between calculated model and observation than for LB 1919. For the lower wavelength range ($\lambda \lesssim 150 \text{Å}$) a small discrepancy and a too low SED of the model flux is recognizable, whereas for intermediate wavelengths ($150 \text{Å} \lesssim \lambda \lesssim 200 \text{Å}$) some opacity is missing and the model flux exceeds the observed one.

For the comparison with the spectra, different kinds of models were calculated. All models include elements identified in the *FUSE* observation with the abun-

dances determined in section 6.7. For one type of model iron is added to this basic structure. The other type of model includes iron as well as nickel. Considering two types of models offers a way to study the influence of additional opacity caused by elements with no detectable lines in the spectra, hence no precisely defined abundances. For convenience the two type of models will be sometimes from now referred to as *iron* and *nickel* models, keeping in mind that these are only the heaviest elements included.

Contrary to LB 1919, the flux obtained from the model calculations for atmospheres with a homogeneous mixture of elements is too high to reproduce the observed spectrum. While the agreement is good for wavelengths $> 200 \text{ \AA}$, the lower wavelength range deviates clearly. This is the case for all T_{eff} and $\log g$ combinations, as well as for the different number of elements. Adding nickel to the models also has only a minor influence and affects mainly the already well fitting upper wavelength range. Contrary to the behaviour of LB 1919, in the case of GD 246 more absorbers producing additional opacity seem to be missing.

The diffusion models are more capable of reproducing the observed spectrum. For the elements up to iron the flux does not exceed the observational SED. For all T_{eff} and $\log g$ the flux is considerably too low especially in the lower wavelength range. Raising the surface gravity prevents the elements from floating in the atmosphere which subsequently increases the flux. Thus, the best fits can be achieved for the highest $\log g$. As before, varying temperatures in the calculations affect the flux only marginally (see the top panels in figure 6.17).

The homogeneous models, including nickel as an additional absorber, show in principle the same behavior as the models with elements up to iron. Since the maximum abundance of nickel, as taken from the *FUSE* analysis, is comparably small no large deviations can be expected. Only for a small $\log g$ a minor flux decrease can be detected.

The effect of the additional opacity becomes apparent only in the modeling of the stratified atmospheres and the self-consistently computed nickel abundances. The SED gets distorted showing large peaks along with nearby deep flux deficiencies in a more extreme way than noticed for the *iron* models. Figure 6.17 gives an overview of homogeneous and stratified *iron* and *nickel* models calculated for different values for the surface gravity. Clearly seen is the unusual shape of the SED for the calculated *nickel* diffusion models.

The reason for this deformation is an extreme form of line blanketing caused by the large amount of additional nickel lines. This can be seen when taking a closer look on the initial spectrum, before processing it for a comparison with the *EUVE* spectrum (figure 6.18). The line blanketing in the model is in some regions strong enough to lower the flux over a remarkably large wavelength range. The original continuum in those regions can not be any longer identified, thus giving

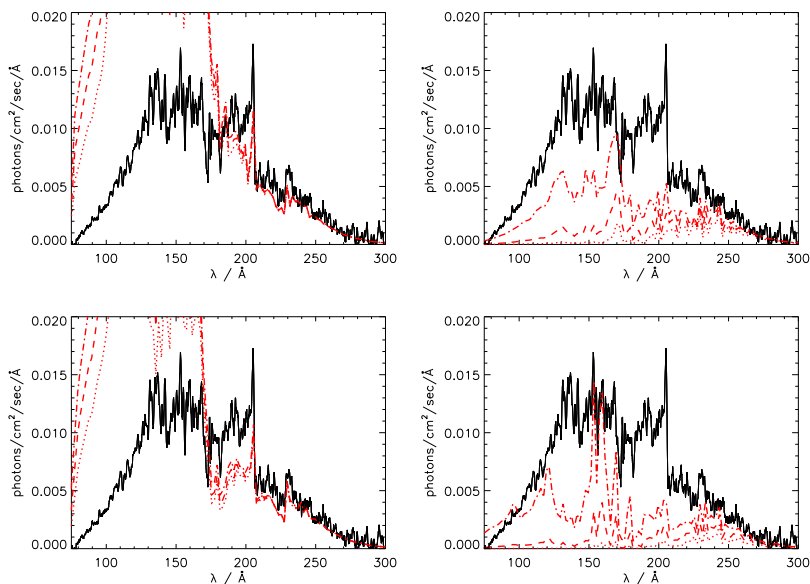


Figure 6.17: EUVE spectrum of GD 246 (solid line) with overplotted models. All models calculated with $T_{\text{eff}} = 55\,000\text{ K}$ and elements H,C,O,Si,P,S,Ge and Fe with abundances according to table 6.2. Top left: Homogeneous models with $\log g = 7.3$ (dotted), $\log g = 7.6$ (dashed) and $\log g = 7.9$ (dash dot). Top right: Diffusion models with same parameters. Bottom left: Homogeneous models with parameters as before but with nickel added to the calculations. Bottom right: Diffusion models with same parameters and Ni.

the impression that we deal with absorption lines stamped on a lower continuum. Especially for the wavelength range between 100–300 Å, the appearance almost resembles an emission line spectrum.

For the produced synthetic spectra, the atomic data for iron and nickel included all calculated .LIN lines available (see chapter 5). That in fact line blanketing is responsible for the shape of the SED can be confirmed by using only the verified iron and nickel lines. After performing a formal solution of the equation of radiative transfer with .POS lines no accumulation of unexpected emission lines should be present in the spectrum. The input model still contains the opacity of all lines.

For the homogeneous *iron* models the difference between formal solutions with .POS and .LIN files is as expected. Clearly, more lines are recognizable in the .LIN spectrum. Whereas the .POS spectrum does not show any signs of serious

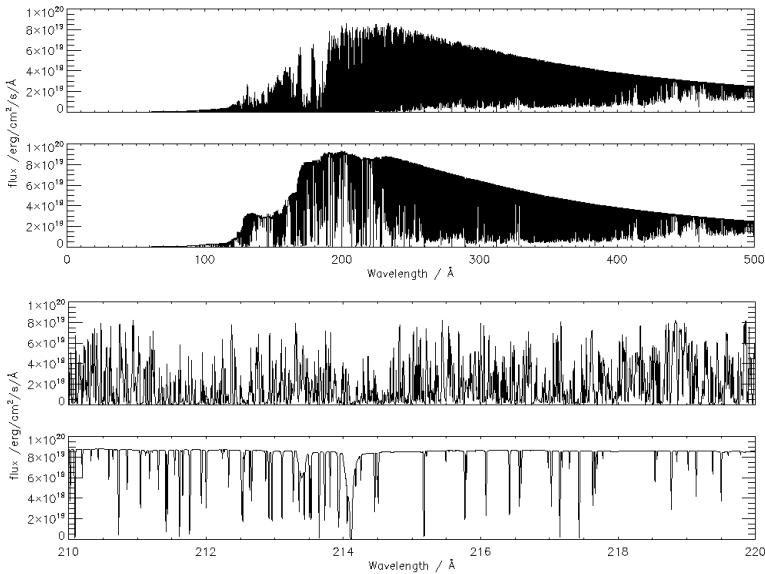


Figure 6.18: Synthetic spectrum of a diffusion model calculated with $T_{\text{eff}} = 59000\text{K}$ and $\log g = 7.9$ and H, C, O, Si, P, S, Ge, Fe, and Ni. The top panel shows the extreme line blanketing resulting in an emission-line like structure of the spectrum. The flux in the second panel from top results from a formal solution with .POS atomic data for Fe and Ni. The last two panels show a detailed view of the models.

line blanketing, the .LIN spectrum is affected slightly more. The diffusion models calculated with .POS lines fit in this picture, even though more regions are affected by line blanketing, which is overall stronger. Not surprisingly the emergent fluxes of the *iron* models calculated by the formal solutions with either .POS and .LIN files are in accordance.

For the *nickel* models, which were the reason for the inspection of the formal solutions with less opacity, the expected differences can be found. The homogeneous models already indicate a strong line blanketing in the region around 170Å for the .LIN data, which vanishes when using .POS lines. The continuum and the individual lines are nevertheless distinguishable even for the highly opaque formal solution. This is not the case for the diffusion models. The emission-line like structure of the emergent flux was already described above. Reducing the opacity by removing the uncertain .LIN lines eliminates the large flux deficiencies and the continuum flux is recovered. The usage of reduced opacity for the calculation

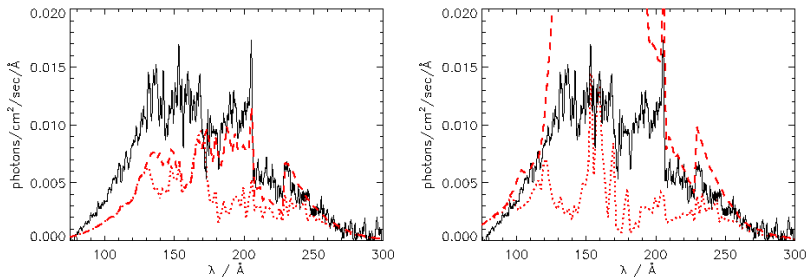


Figure 6.19: *EUVE* spectrum of GD 246 (solid line) compared to diffusion models with $T_{\text{eff}} = 55000\text{K}$ and $\log g = 7.9$. Left: *Iron* model resulting from formal solutions with .LIN (dotted) and .POS (dashed) lines. Right: *Nickel* models calculated accordingly.

of the emergent flux obviously corrects for the strongly deformed overall shape. This can be seen in figure 6.18, where the calculated spectra of diffusion models resulting from formal solutions with .POS and .LIN lines are shown. Especially when regarding a narrow wavelength range, the emission-line like structure of the spectrum can be seen. It is needless to say that the change in the emergent flux also affects the comparison with the *EUVE* spectrum.

Using the .POS atomic data for the formal solution for all homogeneous and stratified *iron* models in the T_{eff} and $\log g$ range, as well as for the models with *nickel*, gives a detailed overview over the influence of the large number of lines (see figure 6.19). For the homogeneous *iron* models less opacity results in a poor fit with a model flux exceeding the observation by far. The consequences are negligible, since the homogeneous models with all lines included did not offer a satisfying result either, unlike the diffusion models, which produced a flux which was too low to match correctly. The diffusion models benefit from the reduced lines. The flux is lifted and reaches almost the maximum of the observed spectra. Especially for a high $\log g$ and a wavelength range $> 160 \text{ \AA}$ a good agreement can be achieved. The *nickel* models again behave in a different way. Here, the change in lines already shows an impact on the models with homogeneously mixed elements in the atmosphere. The flux in the lower wavelength range is still too high, but the intermediate range can be reproduced better than before. For the strongly line blanketed diffusion models the usage of the .POS lines reduces the quality of the fit dramatically. Instead of a small variation, the increase of flux is extreme and causes the SED to resemble the shape of a homogeneously calculated model. An

explanation can be found in the inner structure of the atmosphere. All models are calculated with all lines included to account for the opacity provided by these elements. Only for the last step in the calculations, i.e. the formal solution of the equation of radiative transfer, a different number of lines are taken. For the models with iron and nickel the large opacity in the model calculations blocks the flux effectively, so that only a small amount is eventually emitted from the surface. Changing the number of lines in the last step of the calculations leaves the structure of the atmosphere unaltered. By reducing the opacity however, the formerly blocked flux can escape. The result is a model flux much higher than the observation. The described behavior can be studied in figure 6.19, where a comparison of the different models with the *EUVE* spectrum of GD 246 is shown. To avoid confusion two things should be noted.

First, the usage of .POS files is only reasonable for the identification of individual lines, since the knowledge of the exact position of the line in this case is necessary as already stated in chapter 5. The position of the .LIN lines has not yet been confirmed by laboratory measurements, yet they are present in the spectrum. This means that a line displaced by a few Å is most likely to appear at another position still in the regarded region. Thus, they can account for the opacity within the *EUVE* wavelength range. The purpose of the .POS lines in the context of the analysis of the *EUVE* spectrum of GD 246 is only to clarify the effect of the line blanketing caused by the large number of iron and nickel lines on the modeled spectra.

Second, the very effect of line blanketing becomes eminent at the diffusion calculations for the *nickel* models. The reason is either a too high amount of nickel calculated in a self-consistent way, or an interaction of nickel with the other elements in the atmosphere. In any case neither the homogeneously calculated models nor the diffusion models provide a suitable fit.

Under the assumption that the models with homogeneously mixed elements are capable of adequately reproducing the *EUVE* flux, additional opacity would be required in the calculations. This can only be accomplished by introducing new elements, because the abundance of iron and nickel, as well as the one of the other elements, is limited by the *FUSE* analysis. Deviating from the original attempt to reproduce the *EUVE* spectrum of GD 246 only with elements with detected lines, models with an additional nitrogen abundance were computed. Nitrogen was chosen, because it is one of the first elements produced in the stellar evolution and can be found in central stars of planetary nebulae as well as in many WDs. The parameters of the computed homogeneous and stratified models are chosen considering the best fitting values for the diffusion *nickel* models, $T_{\text{eff}} = 59000\text{K}$ and $\log g = 7.9$, since the homogeneous models are much less affected by varying parameters.

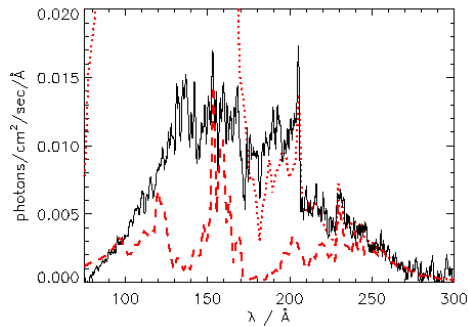


Figure 6.20: Homogeneous (dotted) and diffusion (dashed) model plotted over the GD 246 *EUVE* spectrum (solid line). Models calculated with $T_{\text{eff}} = 59000\text{K}$, $\log g = 7.9$ and H, C, O, Si, P, S, Ge, Fe, Ni with abundances according to table 6.2 plus N as additional absorber with no identified lines and an assumed abundance of $\text{N}/\text{H} = 2.9 \cdot 10^{-9}$. The additional opacity does not result in a better fit.

The results are not explicit. Adding nitrogen to the models does not lower the flux of the homogeneous model and the diffusion model shows the same line blanketed shape as observed before (see figure 6.20). Clearly, the absorption processes treated so far do not provide a coherent conclusion.

The investigation of the *EUVE* spectrum of GD 246 with two types of models with iron and nickel as the heaviest elements included shows that the opacity of additional elements with no detectable lines in the spectra can have a significant effect on the SED in the *EUVE* range. The stratified models with $T_{\text{eff}} = 55000\text{K}$, $\log g = 7.9$, and iron as heaviest element provided the best fit to the observation. The models with a homogeneously mixture of elements in the atmosphere failed in reproducing the spectra. Adding nickel to the models results in a strong line blanketing and a worse fit for the stratified models. The effect of the high number of nickel lines can be seen when comparing spectra calculated with the .LIN and .POS line data set. In the first case the spectrum resembles an emission-line like structure. In the second case individual lines can be recognized. The investigation showed the dependence of the fit quality on the T_{eff} and $\log g$ of the star and used a fixed column density of $\text{N}(\text{H I}) = 1.8 \cdot 10^{19}\text{cm}^{-2}$, $\text{He I}/\text{H I} = 0.05$, and $\text{He II}/\text{H I} = 0.03$.

6.9.3 Column density determination

The treatment of the ISM absorption, as described above, offered a way to effectively analyze a larger number of spectra differing in their T_{eff} and $\log g$ parameters. Taking a fixed value for the hydrogen and helium column densities is legitimate in order to study the influence of the photospheric properties on the spectrum, also because the parameters taken originate from an analysis of the same wavelength range. For a fine adjustment, i.e. to find the best fit for the whole set of parameters, the column densities have to be determined for every combination of T_{eff} and $\log g$. The quality of the fit depends on the chosen value for all three column densities (s.o.), whereas the influence of the hydrogen column density can be regarded as most relevant. Therefore, instead of taking the value of $N(\text{HI}) = 1.8 \cdot 10^{19} \text{cm}^{-2}$ a lower hydrogen column density of $N(\text{HI}) = 1.5 \cdot 10^{19} \text{cm}^{-2}$ and $N(\text{HI}) = 1.3 \cdot 10^{19} \text{cm}^{-2}$ (Barstow et al. 1997) was tested. Reducing the absorption of interstellar hydrogen improves the match for the formerly undervalued fluxes. For the first value the diffusion models fit slightly better, even though the lower wavelength part as well as the characteristic He II absorption edge at 227.8 \AA can not be fitted well. In the second case, the flux gets too high already for the diffusion models, so that the homogeneous models deviate even more. The obvious need to include the column densities of H, He I, and He II to achieve a good agreement hinders the analysis, since this increases the number of parameters for each fit to 6. These are temperature, surface gravity, element abundances, the values for hydrogen column density, and column densities for He I and He II. For a systematic investigation of the influence of the column density absorption, therefore, a large number of possible combinations has to be tested.

For every set of parameters for T_{eff} and $\log g$ for the stratified and homogeneous *iron* and *nickel* models, different values for hydrogen and helium column densities have been applied. For the hydrogen column density they range from $1.1 \cdot 10^{19} \text{cm}^{-2}$ to $2.1 \cdot 10^{19} \text{cm}^{-2}$ in steps of $0.1 \cdot 10^{19} \text{cm}^{-2}$. For both helium column densities they cover the range from $0.02 \cdot N(\text{HI})$ to $0.42 \cdot N(\text{HI})$ in steps of $0.02 \cdot N(\text{HI})$. This leads to a total number of 4851 possibilities for every T_{eff} and $\log g$ combination for one set of models. With 4 different types of models, *iron* or *nickel* with a homogeneous or stratified atmosphere this amounts to 174636 different fits for 9 T_{eff} and $\log g$ combinations. An inspection with the naked eye would clearly be too time consuming, therefore a χ^2 analysis was performed to determine the smallest difference of model and observation and directly start a new calculation with a new set of parameters.

The results can be displayed in a 3 or rather 4 dimensional plot. In such a graph the χ^2 deviation for each combination is plotted over the corresponding column densities for He I and He II. The varying column densities of hydrogen are marked

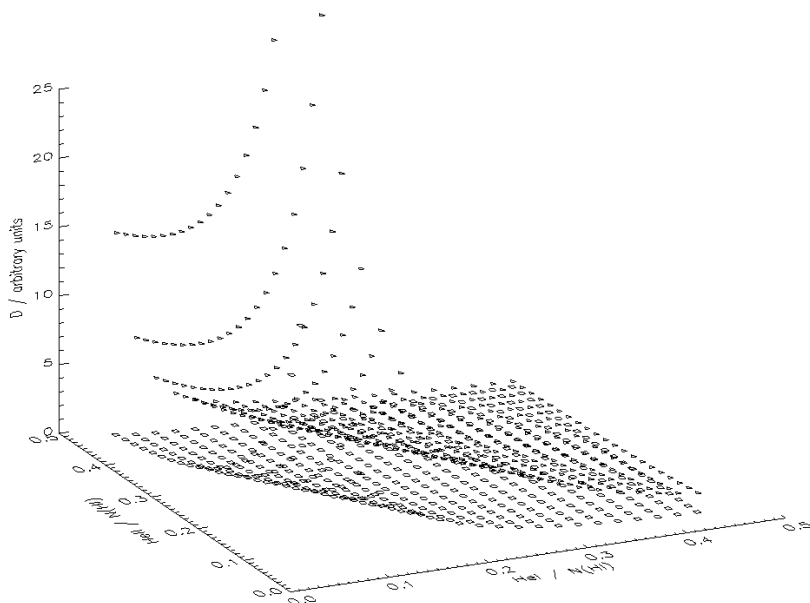


Figure 6.21: Deviation of the model spectra from the observation plotted over the column densities of He I and He II. Models calculated with $T_{\text{eff}} = 59000\text{K}$, $\log g = 7.9$ and a homogeneous mixture of elements up to *iron*. For clarity the plot is only shown for two different column densities of hydrogen marked with different plot symbols, $N(\text{H I}) = 1.1 \cdot 10^{19}\text{cm}^{-2}$ (triangle) and $N(\text{H I}) = 2.1 \cdot 10^{19}\text{cm}^{-2}$ (square). The deviation is highest for low helium column densities.

by different colors or symbols for the data points. Every combination of T_{eff} and $\log g$ corresponds then to another plot. This illustration supports the search for possible systematic patterns. A minimum in the plot corresponds to a minimum deviation from the observation and therefore represents the parameters giving the best fit.

The homogeneous *iron* models show a uniform contribution of values for the deviation for high He I and He II column densities. For lower helium column densities, the deviations begin to increase. As expected from the analysis with constant column densities, the differences between model and observation are comparatively large. Figure 6.21 shows such a deviation plot for an *iron* model with $T_{\text{eff}} = 59000\text{K}$ and $\log g = 7.9$. For clarity, only two different column densities for hydrogen are depicted and marked with different symbols. A minimum value for the deviation can not be easily seen. Out of many similar values the

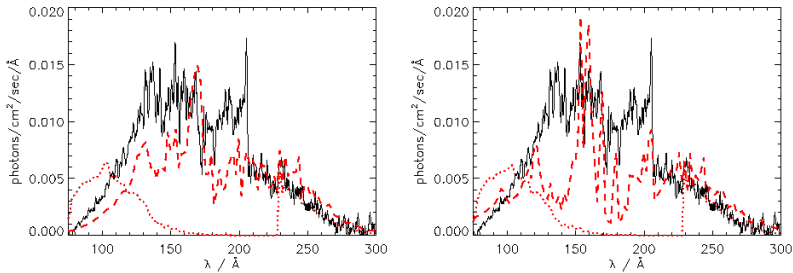


Figure 6.22: Best fit models plotted over the *EUVE* spectrum (solid line). Left: *Iron* models with $T_{\text{eff}} = 55000\text{K}$. The homogeneous model can best be fitted with $\log g = 7.3$ and column densities of $N(\text{H I}) = 1.9 \cdot 10^{19}\text{cm}^{-2}$, $\text{He I} = 0.04 \cdot N(\text{H I})$, and $\text{He II} = 0.42 \cdot N(\text{H I})$ (dotted). For the diffusion model $\log g = 7.9$ and $N(\text{H I}) = 2.0 \cdot 10^{19}\text{cm}^{-2}$, $\text{He I} = 0.02 \cdot N(\text{H I})$, and $\text{He II} = 0.02 \cdot N(\text{H I})$ result in the best fit (dashed). Right: The same for models including *nickel*. In the homogeneous case the parameters are in accordance with the ones found for the *iron* model. For the diffusion model $\log g = 7.9$, $N(\text{H I}) = 1.1 \cdot 10^{19}\text{cm}^{-2}$, $\text{He I} = 0.1 \cdot N(\text{H I})$, and $\text{He II} = 0.02 \cdot N(\text{H I})$ are needed.

best fit can however be found for $T_{\text{eff}} = 55000\text{K}$, $\log g = 7.3$ and column densities of $N(\text{H I}) = 1.9 \cdot 10^{19}\text{cm}^{-2}$, $\text{He I} = 0.04 \cdot N(\text{H I})$, and $\text{He II} = 0.42 \cdot N(\text{H I})$. The *nickel* models behave in a very similar way. The obtained best-fit parameters are in agreement with the *iron* models, but the deviation is slightly higher. With the so determined parameter a best fit model can be calculated to compare to the observation. As the former results imply, the model flux of the homogeneous models is also for the best fitting value not even close to the observation. Instead of being persistently too high, the absorption due to hydrogen and helium is rather reducing the SED effectively. This can be recognized at the high values for the hydrogen column density and the high density for the He II column.

The more promising diffusion models show, also for the different column densities, much smaller deviations. Furthermore, the distribution of the values for the deviation in the plot shows a systematic decrease of the deviation towards smaller helium column densities. Since the model flux exceeded the observation for the constant column densities, it is not surprising that a low absorption is preferred. The uniformity of the decrease on the other hand suggest that He I and He II can be regarded as equally important for the shape of the flux distribution. Instead of speaking of two column densities, in the following they can therefore be referred to as a single helium absorption.

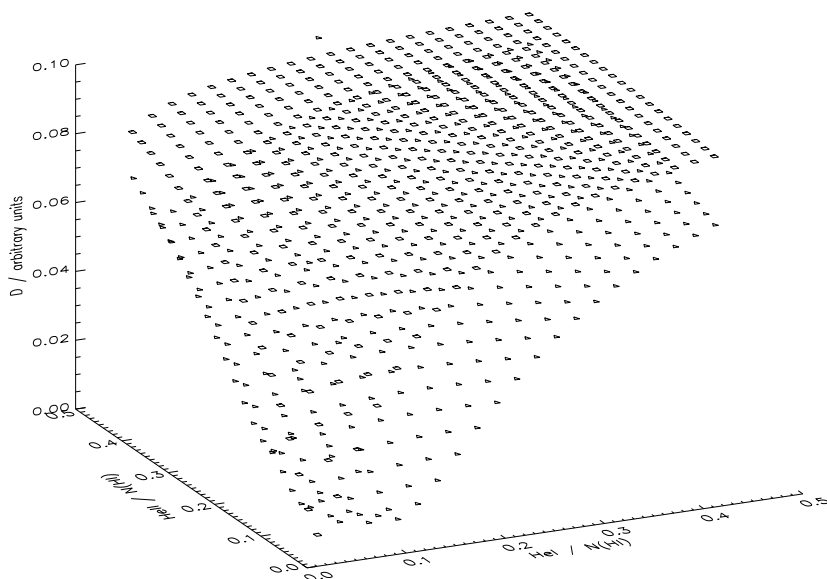


Figure 6.23: Deviation plot for LB 1919 and a diffusion model calculated with $T_{\text{eff}} = 56000\text{K}$ and $\log g = 8.5$. The same two column densities as in figure 6.21 are shown. The deviation gets smallest for low values of the helium column densities.

The comparison between model flux and observation shows better agreement for the diffusion models, especially for the *iron* models. The best fit parameters in this case are $T_{\text{eff}} = 55000\text{K}$, $\log g = 7.9$, $N(\text{H I}) = 2.0 \cdot 10^{19}\text{cm}^{-2}$, $\text{He I} = 0.02 \cdot N(\text{H I})$, and $\text{He II} = 0.02 \cdot N(\text{H I})$. For the stratified models with nickel as the heaviest element the results are $T_{\text{eff}} = 55000\text{K}$, $\log g = 7.9$, $N(\text{H I}) = 1.1 \cdot 10^{19}\text{cm}^{-2}$, $\text{He I} = 0.1 \cdot N(\text{H I})$, and $\text{He II} = 0.02 \cdot N(\text{H I})$. Again the temperatures and surface gravities match, the hydrogen column densities on the other hand differ significantly. Therefore, two remarks should be made.

First, it is fairly hard to bring the modeled flux with a *nickel* composition of the atmosphere in agreement with the observation. Even for different column densities of hydrogen and helium, in some regions considerable differences are seen. The reason is the before mentioned strong line-blanketing.

And finally, even for the best fit of all possible combinations, i.e. the diffusion *iron* model with $T_{\text{eff}} = 55000\text{K}$ and $\log g = 7.9$, deviations occur, especially in the lower wavelength range. This region overlaps with the *Chandra* range. Finding

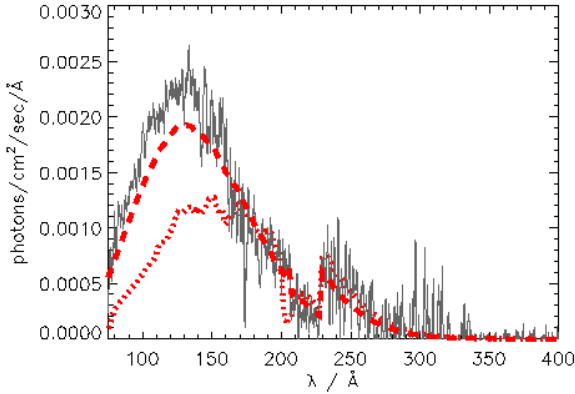


Figure 6.24: Best fit models for the *EUVE* spectrum of LB 1919 (solid line). The homogeneous model (dotted) is calculated with $T_{\text{eff}} = 56000\text{K}$, $\log g = 8.5$ and abundances according to table 6.2. The column densities amount to $N(\text{HI}) = 1.6 \cdot 10^{19}\text{cm}^{-2}$, $\text{He I} = 0.02 \cdot N(\text{HI})$, and $\text{He II} = 0.04 \cdot N(\text{HI})$. The parameters of the diffusion model (dashed) are $T_{\text{eff}} = 56000\text{K}$, $\log g = 8.5$, $N(\text{HI}) = 1.7 \cdot 10^{19}\text{cm}^{-2}$, $\text{He I} = 0.02 \cdot N(\text{HI})$, and $\text{He II} = 0.04 \cdot N(\text{HI})$.

correct absorption column densities that are suitable for both wavelength ranges is therefore a difficult task. Figure 6.22 demonstrates the effect of the systematically determined column densities for hydrogen and helium on the SED of the *iron* and *nickel* models. The homogeneous models do not fit the observation at all, while the diffusion models in the *iron* case provide the best agreement.

The interesting question is how the determination of the best fitting column densities affects the quality of the fit for LB 1919. Applying the whole procedure to LB 1919 should produce the final and best fit for the *EUVE* analysis. The deviation plots for homogeneous and stratified models do not differ in the way noticed for GD 246. This time in both cases low absorption values for the helium column densities are preferred. This is not surprising, since the flux was too low in any of the investigated models. Figure 6.23 shows a deviation plot, typical for homogeneous and diffusion models calculated for LB 1919 as well as for the diffusion models for GD 246. The deviation gets smaller towards small helium column densities and the minimum can be found easily. In general, the calculated discrepancies are lower than for GD 246. For the homogeneous models the best fitting parameters are $T_{\text{eff}} = 56000\text{K}$, $\log g = 8.50$, $N(\text{HI}) = 1.6 \cdot 10^{19}\text{cm}^{-2}$, $\text{He I} = 0.02 \cdot N(\text{HI})$, and $\text{He II} = 0.04 \cdot N(\text{HI})$. In the case of a stratified atmosphere they amount to

$T_{\text{eff}} = 56000 \text{ K}$, $\log g = 8.50$, $N(\text{H I}) = 1.7 \cdot 10^{19} \text{ cm}^{-2}$, $\text{He I} = 0.02 \cdot N(\text{H I})$, and $\text{He II} = 0.04 \cdot N(\text{H I})$. The results are only deviating slightly in the hydrogen column density and lead to the conclusion that a comparison between homogeneous and stratified models concerning the quality of the fit is independent from the exact value chosen.

The quality of the final fit is as expected better for a stratified atmosphere. In fact, the observed shape of the SED can be reproduced in a more satisfying way. Only a small flux deficiency is still recognizable. The atmosphere with a homogeneous mixture of elements on the other hand still does not reach the observed flux maximum (figure 6.24).

The usage of only those lines, which could be identified in the *FUSE* spectrum of LB 1919 helped to improve the fit of the model atmospheres to the *EUVE* spectrum. Even though no complete match could be achieved for the stratified models, they are by far more suitable than atmospheres with a homogeneous mixture of elements. In the case of GD 246 the diffusion models still show some discrepancy, but no larger deviation than found by Landenberger-Schuh (2005). The aim to explain the *Chandra* spectrum of LB 1919 can now be tackled with the knowledge gained out of the analysis of the *FUSE* and *EUVE* spectra of the metal poor white dwarf.

6.10 Chandra analysis (LB 1919)

6.10.1 Homogeneous models

The analysis of the various wavelength ranges and different spectra so far have been performed to explain the metal poor composition of LB 1919 and to reproduce its spectra with a model atmosphere ideally suitable for all wavelengths. Thus, model spectra computed with the newly gained insight concerning occurring elements and their abundances should be able to reproduce the *Chandra* spectrum of LB 1919.

For the synthetic spectra calculated for the comparison, again the elements introduced in section 6.6 have been used. The temperatures and surface gravities remain in the range defined in the same section. At first, the models with a homogeneous mixture of elements in the atmosphere are regarded. The column densities for hydrogen and helium are now chosen considering on the best fitting results from the *EUVE* analysis.

The results can be discussed in the established way. A closer look on the model spectra reveals line features that have to be brought to agreement with the observed structure. Individual features in the observation are not clearly recognizable, a fact already known from the *Chandra* analysis for the hydrogen and iron model in

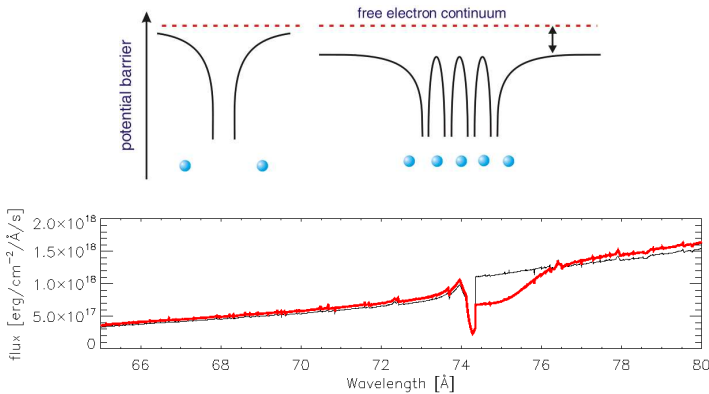


Figure 6.25: Top: The coulomb potential of the single atoms is disturbed by neighboring atoms. High lying levels are broadened and eventually dissolved (picture based on <http://l1t1.iams.sinica.edu.tw/>). Bottom: The effect of the *occupation probability formalism O CPR* on a model spectrum with $T_{\text{eff}} = 54000\text{K}$ and $\log g = 8.2$. The model drawn with the thin line is calculated without *O CPR*, the model drawn with the thick line is calculated with the *O CPR* formalism.

section 6.3. The identification of single lines in the spectrum is therefore an unpromising endeavor. Rather than the position of the lines, the line strength proves to be the essential point and should not contradict the observation.

The calculated models in the grid fit the observation best for $\log g = 8.5$ and high T_{eff} (54–56 kK). The line strengths are in agreement for most of the modeled lines and the SED of the flux can be fitted smoothly (cf. figure A.8). Some of the model lines are yet excessively strong and stand out of the observed line structure. To identify the responsible model atoms the influence of the different elements on the spectrum can be studied.

The biggest influence, i.e. most of the lines, comes from the different ionization stages of oxygen. Features of O V and O VI are present in the *Chandra* wavelength range (see figure 6.27). In fact, excluding oxygen from the calculations, as done in section 6.9, leaves only the features of one other element in the spectrum, silicon. Whereas all of the oxygen features can be brought to consistency when employing $\log g = 8.5$, the Si features are still clearly too strong (see figure A.8). While one line at 117.85Å is weak enough to match the observation the line at 96.44Å , sticks clearly out (figure 6.27). Another Si feature around 74.6Å , should be regarded with attention.

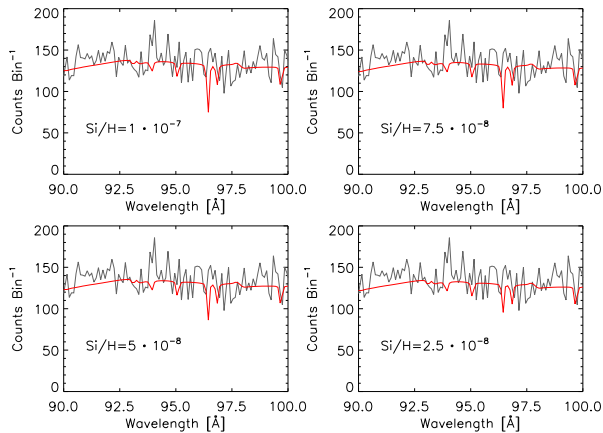


Figure 6.26: Detail of the *Chandra* spectrum of LB 1919 (thin line) with overplotted model atmosphere calculated with $T_{\text{eff}} = 56000\text{K}$, $\log g = 8.5$ and elements H, C, O, P, and S with abundances according to table 6.2 (thick line). The abundance of Si is varied from $\text{Si}/\text{H} = 1 \cdot 10^{-7}$ to $\text{Si}/\text{H} = 2.5 \cdot 10^{-8}$ in order to fit the observation.

This Si V feature is produced by a resonance of a radiative bound-free cross-section. It extends over a wide range of 2 \AA . This is broader than any line modeled in this wavelength range and highly unexpected. A numerical failure could be excluded. In fact, the numerical treatment of the radiative bound-free cross-sections turns out to be the reason for the extreme broadening of the structure. More precisely, it is the dissolution of the atomic levels by the plasma perturbations in the atmosphere that causes the effect. The high-lying atomic levels are strongly perturbed by other charged particles, so that they are broadened and dissolved. This level dissolution is numerically treated by defining an occupation probability, i.e. a ratio of the level populations to those in absence of perturbation, and applying it to each level (Werner et al. 2003). The theory for a phenomenological description of these quantities goes back to Hummer & Mihalas (1988). The generalization to NLTE was done by Hubeny (1992). The broadening of a perturbed level leads to no clearly defined energy and affects therefore the cross section of the regarded transition. This effect leads to the structure seen in the modeled spectra. The calculation of a model atmosphere without the so called *Hummer-Mihalas occupation probability formalism* indeed reduces the width of the feature to a size comparable with the rest of the silicon lines. This can be seen in figure 6.25, where a model calculated with the probability formalism and a model calculated without the formalism are directly compared.

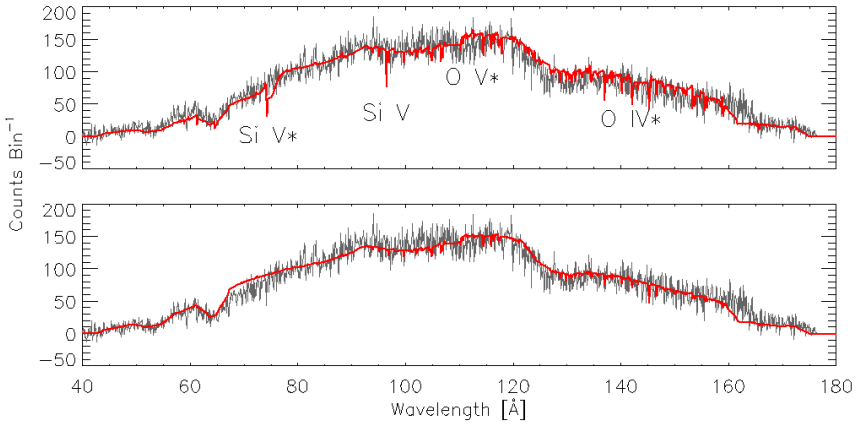


Figure 6.27: Best fit models (thick lines) for the *Chandra* spectrum of LB 1919 (thin lines). The homogeneous model (top panel) is calculated with $T_{\text{eff}} = 56000\text{K}$ and $\log g = 8.5$. The parameters of the diffusion model (bottom panel) are $T_{\text{eff}} = 52000\text{K}$, $\log g = 8.5$. Both models are computed with H,C,O,Si,P, and S. In the homogeneous model calculated with abundances according to table 6.2, Si V features can be found. The component at 74.6Å is caused by the resonance and marked by an asterisk. Also clearly visible is the Si V line at 96.44Å .

Even though the width of this Si feature can be explained by the *occupation probability formalism*, it can not clarify why the strength of the other Si lines is stronger than expected. Obviously the silicon abundance determined in the *FUSE* spectrum are too high to match the *Chandra* observation. The silicon abundance can be reduced to a value that is suitable in order to provide an acceptable fit to the *Chandra* spectrum. The silicon abundance obtained from fitting the lines in the *FUSE* spectrum is $1.2 \cdot 10^{-7}$ (see section 6.6). In order to agree with the *Chandra* observation it has to be reduced to at least $5 \cdot 10^{-8}$ (see figure 6.26). This value is outside of the error margin estimated for the line fitting uncertainty in the *FUSE* range. The fact that the abundance of silicon produces line strengths that are only suitable for a narrow wavelength range raises nevertheless the question if the determination of the abundances might have been subject to mistakes. Since the deviation of the abundances is relatively high, a failure in the abundance based on the *FUSE* observation can be regarded as unlikely. It is interesting to investigate how adequate the stratified model atmospheres are in reproducing the *Chandra* spectrum.

6.10.2 *Stratified models*

It does not come as a surprise that the flux of the diffusion models depends more clearly on the chosen surface gravity. As for the homogeneous models oxygen is the element that mostly influences the model spectrum. A mismatch due to too strong oxygen lines can yet only be seen for a too low $\log g$ in the grid. A value of $\log g = 8.5$ is sufficient to assure an agreement with the observation and provides the best fit regardless of the effective temperatures, which once again are of minor importance (see figure A.9).

The silicon line, so interesting in the homogeneous models, is of no significant importance in the diffusion models. The silicon abundance has already been predicted to be very low by the stratified models at the analysis of the *FUSE* spectrum (see section 6.6). While it was a problem for the fit to the silicon lines then, it turns out to be helpful now. The self-consistently calculated low abundance of silicon assures a more than satisfying fit to the *Chandra* spectrum. Figure 6.27 shows the best fit homogeneous and stratified models for the *Chandra* spectrum and the difference in the predicted silicon abundances, which can be recognized by the features at 74.6 Å and 96.44 Å.

Before a final evaluation of the collected information about the various characteristics of LB 1919 can be made, for the last time an analysis of GD 246 for the purpose of comparison is performed.

6.11 *Chandra* analysis GD 246

6.11.1 *Homogeneous models*

The separation into *iron* and *nickel* models for the analysis of the *EUVE* spectrum is again used here. Even though the *iron* models were more suitable to explain the observed flux, the presence of Ni V and Ni VI lines was indicated by Vennes & Dupuis (2002) based on a NLTE model-atmosphere analysis. However, the investigation of the *Chandra* spectrum with models with H and Ni (see section 6.5) as well as with the *nickel* models introduced for the *EUVE* analysis can not confirm the presence of Ni lines. Similar to the behavior of the different types of models in the *EUVE* range, the influence of nickel on the SED of the model atmospheres is also noticeable in the *Chandra* range.

The homogeneous models are in general hard to bring in accordance with the observation in this wavelength range. This holds for both the models with iron and the models with nickel as the heaviest element (cf. figures A.10 and A.12). One reason is the strong silicon feature in the model already discussed in the previous section. A probably more important reason is the not suitable absorption by the ISM. The values for the column densities determined in section 6.9 do not result

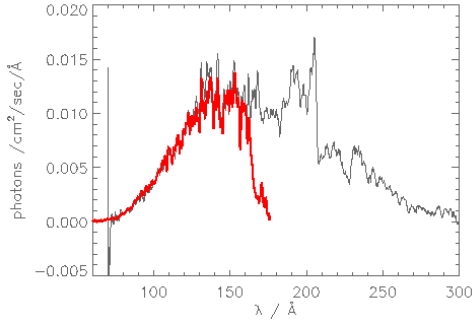


Figure 6.28: Comparison between the *Chandra* (thick line) and *EUVE* spectrum (thin line) of GD 246. The *Chandra* flux is decreasing rapidly at $\lambda > 160 \text{ \AA}$. This wavelength range should be disregarded in the analysis of the *Chandra* spectrum.

in an appropriate flux shape for the *Chandra* range. How big the difference is can be demonstrated by regarding only hydrogen as the column density causing most of the absorption. While a value of $N(\text{HI}) = 1.9 \cdot 10^{19} \text{ cm}^{-2}$ is suitable to account for the absorption in the *EUVE* range, for the *Chandra* spectrum even a column density reduced to $N(\text{HI}) = 1.3 \cdot 10^{19} \text{ cm}^{-2}$ is not enough. Reducing the value further to $N(\text{HI}) = 1.9 \cdot 10^{18} \text{ cm}^{-2}$ eventually results in a successful fit. This, however, is too low to be regarded as realistic.

The final *EUVE* results already indicated that the observed flux in the lower wavelength range is hard to reach. This part of the *EUVE* spectrum overlaps with the *Chandra* observation. A direct comparison of the both observations shows that for wavelengths $> 160 \text{ \AA}$ the *Chandra* flux decreases strongly. This decrease can not be found in the *EUVE* spectrum. For a comparison between *Chandra* observation and model, this wavelength range can therefore be disregarded. Figure 6.28 shows a comparison between the *Chandra* and the *EUVE* spectrum of GD 246 and the overlapping wavelength range.

Even when ignoring the high wavelengths an overall satisfying agreement can not be achieved for most of the homogeneous spectra. The best result is a fit to a homogeneous *iron* model with $T_{\text{eff}} = 55000 \text{ K}$ and $\log g = 7.3$. For higher T_{eff} and $\log g$ the modeled flux deviates to some extent clearly. The *nickel* models do not differ much. In any event, for a potential line identification no .POS lines are located in the *Chandra* range (see chapter 5).

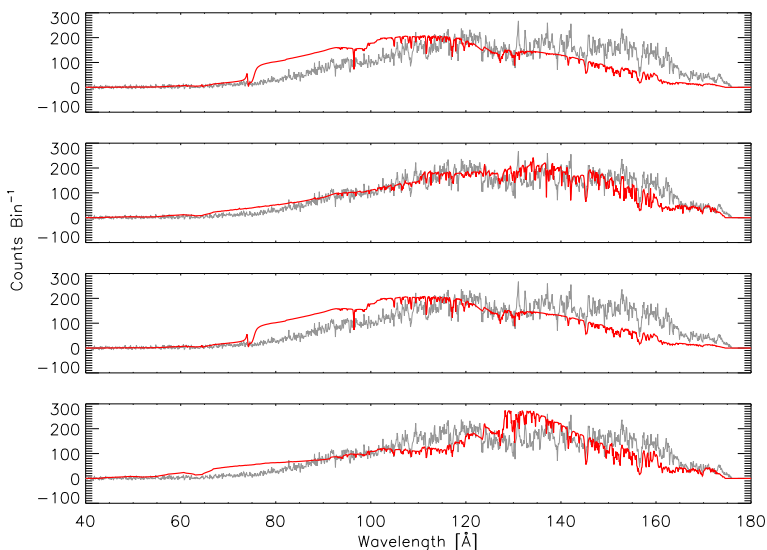


Figure 6.29: Best fit models (thick lines) for the *Chandra* spectrum of GD 246 (thin lines). From top to bottom: Homogeneous *iron* model with $T_{\text{eff}} = 55\,000\text{K}$ and $\log g = 7.3$. Stratified *iron* model with $T_{\text{eff}} = 55\,000\text{K}$ and $\log g = 7.9$. Homogeneous *nickel* model with $T_{\text{eff}} = 55\,000\text{K}$ and $\log g = 7.3$. And stratified *nickel* model with $T_{\text{eff}} = 55\,000\text{K}$ and $\log g = 7.9$.

6.11.2 Stratified models

The diffusion models for the *iron* and *nickel* models fit the observation best for $\log g = 7.9$. In all other cases the modeled flux is too low for $80\text{Å} < \lambda < 120\text{Å}$ and gets far too high for larger wavelengths ($\lambda > 160\text{Å}$). Ignoring again the strong deviations towards the end due to the misleading *Chandra* calibration, leaves still a sudden increase in flux at intermediate wavelengths that can not be found in the observation. For a $\log g$ of 7.3 the rise of the model flux is extremely steep, contrary to the observation (see figures A.11 and A.13).

Contrary to the homogeneous models, an effect of the additional nickel is recognizable. Here, even a high $\log g$ can not keep the elements from levitating in the atmosphere and affecting the SED. The flux shape of the diffusion model is not negatively influenced by the ISM absorption and provides, as in the case of LB 1919, for certain values of T_{eff} and $\log g$ an overall satisfying fit compared to the models calculated with a homogeneous mixture of elements in the atmosphere.

Figure 6.29 shows the final best fits for the *iron* and *nickel* models for GD 246. The best result can be achieved with a stratified *iron* model with $T_{\text{eff}} = 55\,000\text{K}$ and $\log g = 7.3$.

6.12 Final remarks

The investigation of spectra of LB 1919 from X-ray to optical wavelengths should provide a clear picture of the composition of the photosphere and the physical properties of the star. Especially for the question whether the elements in the atmosphere are stratified or homogeneously mixed a final answer should be found. As shown in this chapter however, every investigated wavelength range reveals new characteristics, which partly seem to contradict each other.

No features of iron and nickel were found in the *Chandra* spectrum and the spectrum could be reproduced only by assuming a small amount of iron homogeneously mixed in the atmosphere, or by a stratified atmosphere with high surface gravity causing the iron to sink (see section 6.3). Temperature and $\log g$ of LB 1919 were constrained by fits to the Lyman (section 6.6) and Balmer (section 6.8) lines, and the metal lines in the *FUSE* spectrum agree with homogeneous model atmospheres calculated with temperatures of $T_{\text{eff}} = 54\,000(\pm 2\,000)\text{K}$ and gravities of $\log g = 8.2 \pm 0.3$, while the stratified atmospheres deliver diverse fit qualities for lines of different species (see section 6.6). The SED of the *EUVE* spectrum could be reproduced by a stratified atmosphere including only those elements that were identified in the *FUSE* spectrum and an analysis of the *Chandra* spectrum with the same elements, temperatures, and $\log g$, offered a good agreement for the diffusion models and an acceptable fit for an atmosphere with homogeneously mixed elements.

In general it can be seen that the diffusion models are superior in predicting the SED of a WD. Because they calculate the abundances of the elements in every depth of the atmosphere they can account better for the opacity distribution, which determines the overall flux shape of the spectrum. The accuracy of the fit of the stratified atmospheres depends mainly on the assumed $\log g$. Therefore, for the X-ray and *EUVE* spectra the stratified models provide a better agreement only for a suitable surface gravity. As mentioned before, an accurate fitting of individual spectral lines can not in all cases be achieved with a diffusion model spectrum. Obviously the accuracy of the abundance prediction is good enough for a somewhat precise distribution of elements in each depth so that the opacity can be reproduced. For the reproduction of a single line however a much higher accuracy for the elements abundances is needed. The spectra of the *FUSE*, *HST* and *UVES* instruments can therefore be better described by model atmospheres with

homogeneously mixed elements.

The failure of the diffusion models to reproduce line features of individual species is an intrinsic property of the used code and model atoms (compare Dreizler 1999b and Schuh 2000). Therefore, the missing accuracy of the fits in the wavelength ranges that require a precise line fitting should not be misinterpreted. If the equilibrium of radiative and gravitational forces in LB 1919 would be currently disturbed, much bigger deviations than found in the analysis would have been expected. Especially the SED of the star would have been affected. This leads to the conclusion that the atmosphere of LB 1919 is still in equilibrium and that no significant disturbance takes place at the moment. No iron and nickel and only a few other elements can be identified in the photosphere. For some reason LB 1919 must have entered the WD cooling track (see chapter 2) with its metal poor composition. This poses questions about the evolution of the metal poor WD in general and LB 1919 in particular. A discussion about possible explanations for the development of the LB 1919 configuration seems to be necessary.

Analysis of PG 1520+525

7.1 Previous investigations

PG 1520+525 is also known under the aliases WD 1520+525, EUVE J1521+52.3 and RE J1521+522. It was investigated together with other hydrogen deficient degenerate PG 1159 stars by Wesemael et al. (1985). Temperature and surface gravity were determined roughly to be $T_{\text{eff}} \approx 100\,000\text{K}$ and $\log g > 6$ based on optical and ultraviolet spectrophotometric observations made by the *International Ultraviolet Explorer (IUE)*. The absorption trough between 4640 \AA and 4690 \AA , caused by He II 4686 \AA and C IV lines, which is characteristic for PG 1159 stars, has been identified. Additional strong O VI and C IV features were found in optical spectra of PG 1520+525 (Sion et al. 1985). The first precise determination of T_{eff} and $\log g$ was achieved by an analysis of optical spectra with non-LTE model atmospheres (Werner et al. 1991). The results yielded $T_{\text{eff}} = 140\,000\text{K}$ and $\log g = 7.0$. Dreizler & Heber (1998) used new *HST* observations and NLTE model atmospheres to constrain T_{eff} and $\log g$ of PG 1520+525. The results suggest a higher temperature of $T_{\text{eff}} = 150\,000\text{K}$ and $\log g = 7.5$. The abundances of the identified elements were settled to C/He = 0.3, O/He = 0.1, and N/He $< 10^{-4}$ (number ratio). The small abundance of nitrogen can be explained by the transformation of ^{14}N to ^{22}Ne in the He burning shell in the AGB phase. The resulting neon-rich intershell is then dredged up to the surface in the helium flash that lets the star re-enter the AGB. Indeed, Werner et al. (2004b) identified a Ne VII line at 973 \AA in a *FUSE* spectrum of PG 1520+525 and determined a Ne abundance of about 2 % (mass fraction).

Even though the temperature of PG 1520+525 was determined in different ways, the analyzed spectra do not allow a sufficiently precise conclusion. This is due to the fact that the errors of the analysis overlap significantly. With the strong sensitivity of the soft-X-ray flux to variations in temperature, however, a more precise T_{eff} determination is possible (Werner et al. 2007). No pulsations were found for PG 1520+525. Depending on the viewing angle of the observer certain pulsational

Table 7.1: Model atoms used in the calculations for PG 1520+525. The first four elements, i.e. He to Ne are included in the calculation of the model structure, Mg is added in subsequent line formation calculations. The abundances of the elements in the calculations are taken from Dreizler & Heber (1998). The abundance of Mg is varied from 10 times solar to solar.

Element	Ion	LTE levels	NLTE levels	lines
He	I	18	1	0
	II	22	10	36
	III	0	1	0
C	III	12	6	4
	IV	5	36	98
	V	0	1	0
O	IV	17	1	0
	V	1	20	24
	VI	1	52	231
Ne	VII	0	1	0
	IV	8	1	0
	V	8	5	0
	VI	10	23	56
	VII	6	54	250
Mg	VIII	21	5	6
	IX	0	1	0
	IV	13	1	0
	V	11	10	7
	VI	25	48	161
	VII	19	39	86
	VIII	6	23	56
IX	0	1	0	

modes might be possible that cancel out each other. With no observational evidence for possible oscillations, however, this consideration has to be regarded as speculative.

7.2 Chandra analysis

To determine the temperature of PG 1520+525 and constrain the position of the GW Vir instability strip a *Chandra* LETG spectrum was taken on April 04-06 2006 with an integration time of 142 ksec. Analog to the analysis of LB 1919 and

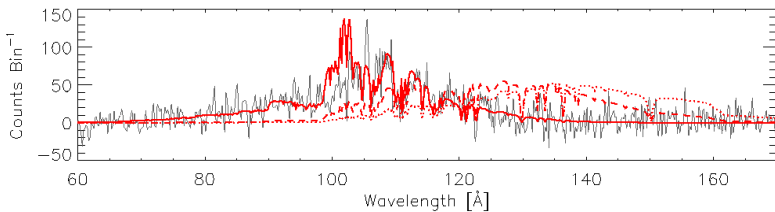


Figure 7.1: *Chandra* count rate spectrum of PG 1520+525 with a binning of 0.2 \AA (thin line). Overplotted are model spectra calculated with $T_{\text{eff}} = 140\,000 \text{ K}$, $\log g = 7.0$, and varying hydrogen column densities applied to demonstrate the effect on the model flux. Three different column densities are applied ranging from $\log N(\text{HI}) = 20.0$ (thick line), to 19.8 (dashed line), and 19.5 (dotted line). Obviously a high column density is needed to provide a satisfying fit for this set of parameters.

GD 246, NLTE models and emergent fluxes have been calculated to compare with the observations. The atomic data includes all elements with expected lines in the *Chandra* wavelength range, i.e. carbon, oxygen, and neon in different ionization stages and with abundances given in Dreizler & Heber (1998). Magnesium is included additionally, keeping fixed the atmospheric structure. Magnesium has been identified in the *Chandra* spectrum of the hot bare stellar core H 1504+65 (Werner et al. 2004a) and it is very likely that a significant influence of magnesium is recognizable in the *Chandra* spectrum of PG 1520+525 as well. Table 7.1 gives an overview of the model atoms used in the calculations.

As before, the calculated flux has then been re-binned, convolved with the response file and multiplied with the effective area of the *Chandra* satellite. The binning was varied slightly depending on the currently regarded wavelength range in order to make a comparison with the observation easier. Values about the hydrogen and helium column densities in the literature are rare. Dreizler & Heber (1998) determined $N(\text{H}) = 2.5 \cdot 10^{20} \text{ cm}^{-2}$. Since other estimations do not exist, the treatment of the interstellar absorption due to hydrogen was regarded as a free parameter in the comparison between model and observation.

Models are calculated for $T_{\text{eff}} = 140\,000 \text{ K}$, $150\,000 \text{ K}$, and $160\,000 \text{ K}$. The $\log g$ amounts to 6.4, 7.0, and 7.5. Each model is then treated with different hydrogen column densities, whereas the helium column densities are fixed to $N(\text{He I}) = 0.05 N(\text{HI})$ and $N(\text{He II}) = 0.026 N(\text{HI})$. Varying the He column densities does not have a noticeable influence on the *Chandra* flux. The results show that an assumed hydrogen column density of $\log N(\text{HI}) = 20.4$ is far too strong to match the observation, rather densities between 19.5 and 20.0 can be expected. The effect of the hydrogen column density on the modeled spectrum can be seen in figure 7.1.

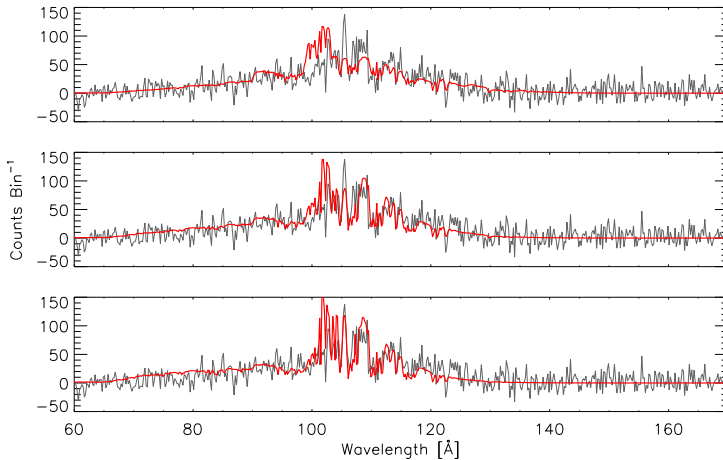


Figure 7.2: Effect of changing T_{eff} on the model spectra for PG 1520+525. The observation (thin line) is overplotted with three models with $\log g = 7.5$ and varying T_{eff} (thick line), from top to bottom $T_{\text{eff}} = 140\,000\text{ K}$, $150\,000\text{ K}$, and $160\,000\text{ K}$. The models are calculated with He, C, O, Ne with abundances according to Dreizler & Heber (1998) and Mg with an abundance of 10 times solar (see table 7.2). The hydrogen column density is $\log N(\text{H}) = 20.0$.

Three different column densities are applied to the model and change the shape of the flux significantly. Increasing the hydrogen column density lifts the flux in the wavelength range below 100 \AA . At the same time the flux in regions $>115\text{ \AA}$ is strongly suppressed. The adjustment of the model fluxes to fit the slopes on both sides of the line-rich center region is as well the most important indicator for the T_{eff} and $\log g$ investigation.

As it turns out, the temperature of $T_{\text{eff}} = 140\,000\text{ K}$ is too low to match the observations. This is true independent of the assumed abundance of Mg. In general, models with a Mg abundance of 10 times solar fit the observations slightly better than models calculated with a solar Mg abundance. However, the differences are small and affect mainly line features that do not have a significant influence on the overall shape of the flux. The best fitting $\log g$ turns out to be 7.5. This provides the best fit for the many lines in the central regions. A lower $\log g$ results in too strong features. The slopes, important for the T_{eff} and hydrogen column density determination, however, are only marginally affected by a change in $\log g$.

Higher temperatures of $T_{\text{eff}} = 150\,000\text{ K}$ and $160\,000\text{ K}$ provide better fits, although the influence of the column density makes it difficult to determine a best fitting value. While for a good fit to the slopes of the observation a higher column

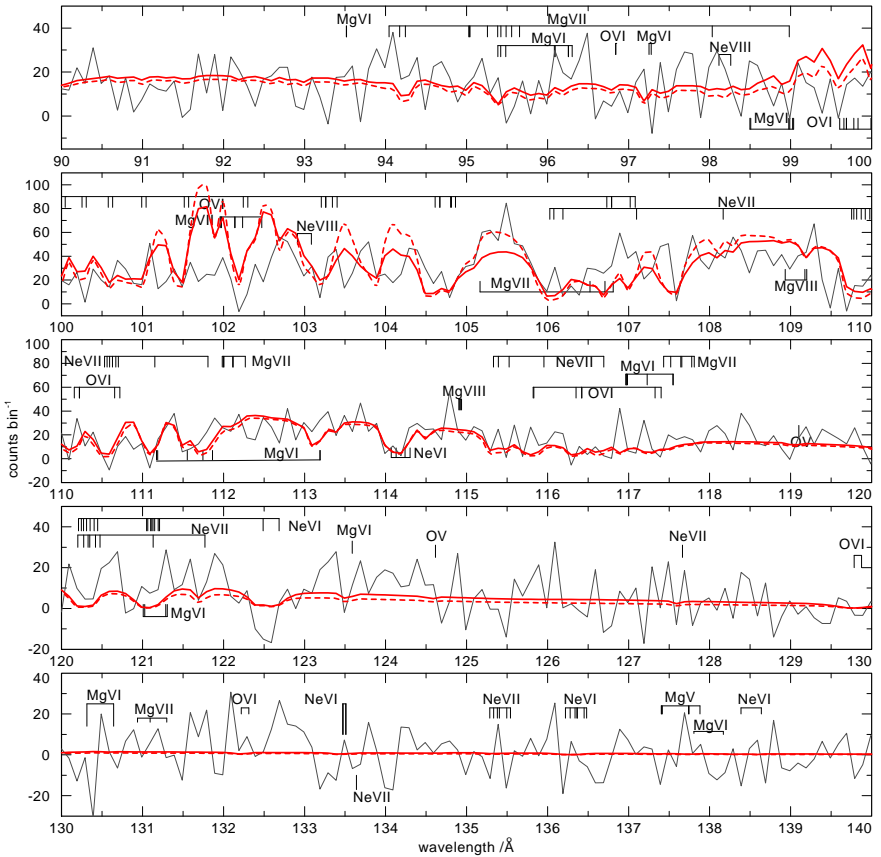


Figure 7.3: Line identification in the *Chandra* spectrum of PG 1520+525 (thin line). Many absorption features of O VI, Ne VI, VII, VII, and Mg VI, VII, and VIII are recognizable. Overplotted are two models with $\log g = 7.5$ and He, C, O, Ne with abundances according to 7.2 and Mg with an abundance of 10 times solar to demonstrate the effect of a change in T_{eff} . The first model is calculated with $T_{\text{eff}} = 150\,000\text{ K}$ (thick line) the second one with $T_{\text{eff}} = 160\,000\text{ K}$ (dashed line).

density of $\log N(\text{H I}) = 19.9 \pm 0.1$ is needed, the line-rich central region agrees better with $\log N(\text{H I}) = 19.5\text{--}19.8$. The differences are subtle and require a careful examination. The main focus of attention is again on the fitting of the overall flux shape of model and spectrum. Figure 7.2 shows a comparison between models calculated with different T_{eff} . Obviously the model with $T_{\text{eff}} = 140\,000\text{ K}$ is not able

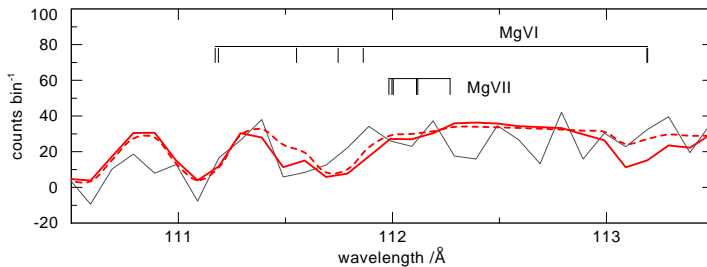


Figure 7.4: Effect of a changed Mg abundance in the model calculations. The *Chandra* observation of PG 1520+525 (thin line) and overplotted model atmospheres calculated with $T_{\text{eff}} = 150000\text{K}$ and $\log g = 7.5$ and the usual abundances for He, C, O and Ne (table 7.2). The Mg abundance is varied from solar (dashed line) to 10 times solar (thick line).

to reproduce the slope of the observed spectrum at the wavelength range around 100 \AA . The models with $T_{\text{eff}} = 150000\text{K}$ and 160000K reproduce this range better but overestimate a line structure around 102 \AA .

Too strong or too weak line features in the center region, however, should not be regarded with too much attention. This is mainly justified due to the fact that the appearance of the line features depends on the implemented line broadening theories, which might deliver inaccurate line shapes (see Werner et al. 2004a and Werner et al. 1991 for details). Furthermore, the abundance of Mg is completely uncertain.

Under this consideration the best fit can be achieved for a spectrum calculated with $T_{\text{eff}} = 150000\text{K}$, $\log g = 7.5$, and a hydrogen column density of $\log N(\text{HI}) \approx 20.0$. For these parameters a satisfying fit can be achieved for both slopes of the spectrum and the central region provides also a good agreement. Only for the feature around 102 \AA a significant difference can be found.

The identification of this and comparable features is a challenging task, since the signal-to-noise ratio of the observation is low. This is the case for a small binning ($\sim 0.1\text{ \AA}$) that is taken for the identification of individual lines. A too large binning ($> 0.2\text{ \AA}$) on the other hand flattens the line profiles and makes the separation of different lines impossible. Nevertheless, a significant number of line features can be identified. As expected, they originate mostly from O VI and Ne VI, VII, and VIII. Also features of Mg VI, VII, and VIII can be found, however the exact abundance of Mg and its influence on the spectrum cannot be determined with certainty. A detailed overview of the identified lines in the spectrum of PG 1520+525 can be found in figure 7.3. The overplotted models with $\log g = 7.5$ and $T_{\text{eff}} = 150000\text{K}$, and 160000K provide in general a satisfying fit for most of the line features. The before mentioned feature at 102 \AA is predicted to be much stronger in the models

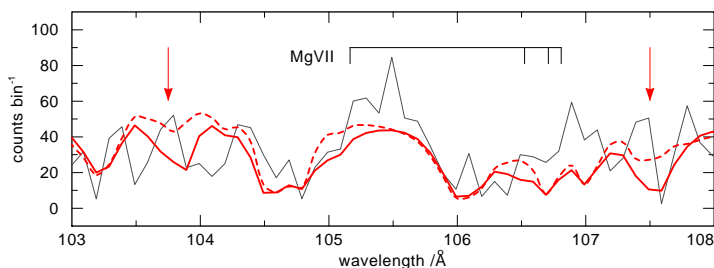


Figure 7.5: *Chandra* observation of PG 1520+525 (thin line) with overplotted model atmospheres calculated with the same parameters as in figure 7.4. Strong autoionization features in the bf cross-section of Mg can be recognized. They result in line-like absorption features in the model spectrum indicated with the two arrows. Because of uncertain wavelength positions, the resonances cannot be identified in the observation (see text for details).

than actually found in the observation. The Mg abundance as a possible source for unsuitable features was investigated further.

A change in the Mg abundance from solar to 10 times solar affects the strength of the identified lines only marginally. Figure 7.4 shows a close-up of identified Mg line features. The effect of a changed Mg abundance on the model spectra can be seen, however, it is not clear which abundance is more likely to fit the observation. This is due to the too low signal-to-noise ratio of the observed spectrum. From the appearance of the lines in the spectrum, however, it can be estimated that the Mg abundance is likely to lie in the range between solar and 10 times solar. Despite the change of the line strengths with different abundances, the flux of the models is also affected in regions where no Mg lines are expected. Here, the noticeable differences are even bigger than found in the line regions. This can be explained by the occurrence of autoionization features in the bf cross-sections. These resonances can be strong and narrow giving the impression to deal with a common absorption line (Werner et al. 2004a). The wavelength position of such a resonance is uncertain and therefore cannot be used for identification of the spectral features. Therefore, these resonances remain a possible explanation for unidentified features in the spectrum.

Even though the Mg abundance remains unclear, the temperature as the most important constraint on the position of the GW Vir instability strip in the HRD could be determined. The parameters for T_{eff} , $\log g$, and element abundances of both stars are shown in table 7.2. Together with the pulsating PG 1159–035, PG 1520+525 can be regarded in the $\log T_{\text{eff}} - \log g$ diagram together with pulsation models predicting the blue edge of the strip (Gautschy et al. 2005). The edge is computed by performing nonradial stability analyses of dipole and quadrupole

Table 7.2: Parameters of PG 1520+525 and its spectroscopic twin PG 1159–035. T_{eff} and $\log g$ with their uncertainties are taken from Jahn et al. (2007). The abundances are given in mass fraction. For PG 1159–035 no Mg abundance was determined. The Mg abundance of PG 1520+525 is a upper limit and can be as high as 10 times solar.

	PG 1159–035	PG 1520+525
T_{eff} [K]	140000 ± 5000	150000 ± 5000
$\log g$	7.0 ± 0.5	7.5 ± 0.5
He	0.33	0.43
C	0.48	0.38
O	0.17	0.17
Ne	0.02	0.02
Mg		$< 6 \cdot 10^{-3}$ ($10 \times$ solar)

high-order gravity (g) modes on model stars analog to the earlier PG 1159 study by Gautschy (1997) (for additional information about the instability analysis technique see also Gautschy et al. 1996). The model stars were extracted from Althaus et al. (2005) and are based on an initially $2.7 M_{\odot}$ star with solar composition, which were evolved from the zero-age main sequence (ZAMS) in the HRD, through the AGB and a VLTP to the cooling sequence as a hydrogen-deficient WD.

The red edge of the instability strip is located at much lower temperatures. No GW Vir pulsator can be found below $T_{\text{eff}} = 80000$ K and no PG 1159 is cooler than 75 000 K. Gravitational settling of C and O is believed to leave behind an almost pure He-rich atmosphere in evolving PG 1159 stars. This settling is slowed down by the presence of residual stellar winds (Quirion et al. 2006). Accordingly, the red edge can be determined by evolutionary calculations taking into account diffusion processes competing against mass loss. Considering PG 1159 model stars with typical envelope compositions and following their stability behavior during the evolution along the white dwarf cooling track leads to a stopping point for the pulsations at a certain T_{eff} and $\log g$ depending on the star's mass. Calculations for different masses then define the red edge. The exact position of the edge is influenced strongly by the mass loss law used in the model (Quirion et al. 2007).

The position of the edges can be seen in figure 7.6 where the positions of PG 1520+525 and PG 1159–035 together with other known PG 1159 pulsators are marked in a T_{eff} - $\log g$ diagram. The positions are shown in comparison with post-AGB evolutionary tracks for PG 1159 stars by Miller Bertolami & Althaus (2006). The masses can be estimated to be around $0.53 \pm 0.07 M_{\odot}$ for PG 1159–035 and $0.61 \pm 0.07 M_{\odot}$ for PG 1520+525. The theoretically calculated blue edge of the

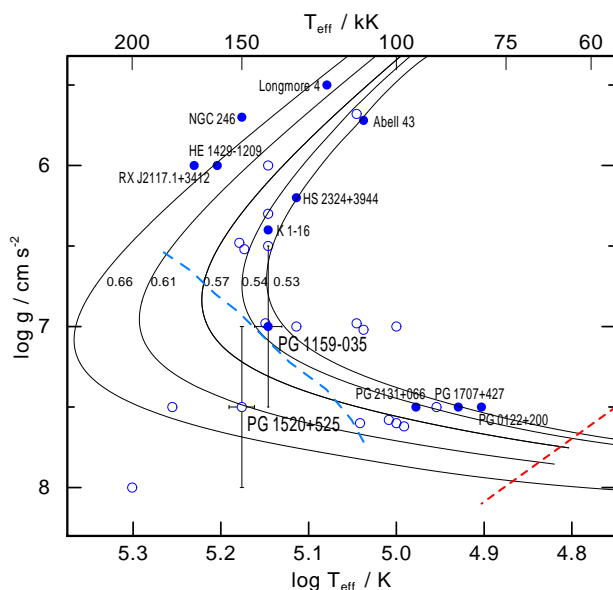


Figure 7.6: $\log T_{\text{eff}} - \log g$ diagram with the pulsating PG 1159–035 and the non-pulsating PG 1520+525. The long-dashed line indicates the position of the blue edge of the GW Vir instability strip as predicted by the theoretical model by (Gautschy et al. 2005). Also shown are the red edge according to Quirion et al. 2006 (short-dashed line). Post-AGB evolutionary tracks by Miller Bertolami & Althaus (2006) computed for PG 1159 stars are included (solid lines) and are labeled with the corresponding masses in solar units.

instability strip is drawn according to Gautschy et al. (2005) and is constrained by the determined position of PG 1520+525. The red edge is consistent with Quirion et al. (2006). Even though the previous determinations of PG 1520+525 already indicated this position by the determined parameters of $T_{\text{eff}} = 150\,000\text{K}$ and $\log g = 7.5$ by Dreizler & Heber (1998), only the detailed investigation of the temperature sensitive soft X-ray range enabled the T_{eff} determination with high accuracy. As indicated in the plot the determination of T_{eff} does not leave much tolerance for the position of the instability strip. A greater inaccuracy is however caused but the uncertainty in $\log g$. A more exact $\log g$ determination however cannot be achieved with the *Chandra* observations. The $\log g$ value for PG 1520+525 determined by Dreizler & Heber (1998) is based on an analysis with model atmospheres computed for two different $\log g$ only. Thus, the error bar might be smaller. The analysis of PG 1159–035 includes $\log g$ of 6.6, 7.0, and 7.5 (Jahn

2005). Again, a grid with a smaller spacing might lead to a smaller error bar.

CHAPTER 8

Discussion

8.1 LB 1919

In chapter 6 an analysis of the metal poor white dwarf LB 1919 was presented. At first, the background of the class of the metal poor white dwarfs and PG 1159 stars was introduced (chapter 2) and informations about X-ray observations of white dwarfs were provided (chapter 3). Two types of NLTE models were used for the determination of the photospheric parameters T_{eff} , $\log g$, and element abundances. One type of models was computed with a homogeneously mixture of elements in the atmosphere, the other type accounts for a stratified composition. Both types of models were described briefly (cf. chapter 4). Test calculations of the model atmospheres were performed and the characteristics of the used model atoms were presented (see chapter 5). The actual analysis starts with the investigation of the metal poor LB 1919 and for comparison the DA white dwarf GD 246 (chapter 6).

LB 1919 was investigated in different wavelength ranges in order to find an explanation for the low metallicity. The first approach to identify features of Fe and Ni in a LETG *Chandra* spectrum failed due to the obviously too small abundance in the atmosphere. The comparison with the DA white dwarf GD 246 showed that a detectable amount of Fe can be kept in the atmosphere by radiative levitation at T_{eff} and $\log g$ comparable to LB 1919. For the identification of element line features and a detailed analysis of their strengths, the investigation was expanded to the *FUSE* wavelength range. Lines of the elements H, C, Si, P, and S were found in the *FUSE* spectrum of LB 1919 and the abundances have been determined with the homogenous models (see table 6.2). The abundance of oxygen could not be determined with certainty due to an unclear interstellar contribution. Analogously, the abundances for the elements in GD 246 were determined including for the first time Ge in NLTE calculations for homogeneously mixed and stratified models. The latter were less able to match the observed spectra of LB 1919 and GD 246 in the *FUSE* range. In order to check how accurate the models including only

the newly identified elements can reproduce the SED of LB 1919, the extreme ultraviolet wavelength range was regarded. Stratified models that only include the elements that were definitely identified in the *FUSE* spectrum in general succeeded in reproducing the SED of the *EUVE* spectra of LB 1919 for certain values of $\log g$ (8.2, 8.5) even though small differences could still be found. The models of GD 246 showed larger differences to the observation when including Ni in the calculations due to a strong line blanketing. The observation was therefore best matched with models including Fe as the heaviest element. A detailed investigation of interstellar hydrogen and helium column densities helped to obtain the best fitting values in the EUV range. The *Chandra* spectra of LB 1919 and GD 246 were fitted with the new models. The metallicity of LB 1919 is too low to identify individual line features in its *Chandra* spectrum, the overall shape of the flux on the other hand is in accordance with modeled stratified atmospheres with a high $\log g$ (8.5). The same is valid for GD 246.

The homogenous models with the same elements and abundances as determined in the *FUSE* spectrum fail in reproducing especially the observed overall flux shape in the EUV range. This indicates that the small differences between the stratified model atmospheres and the observed spectra found in this range can rather be contributed to inaccurate models and do not question the stratified nature of the atmospheres of LB 1919 itself. That the spectra of LB 1919 can in general be described with a stratified atmosphere means that it is in equilibrium between radiative and gravitational forces and that no competing mechanism is currently at work. This confirms theoretical predictions that do not expect mechanisms such as accretion and strong winds or mass-loss to occur in the atmospheres of hot white dwarfs (cf. chapter 2). Only those elements were included in the models that were clearly identified in the spectra. The absence of more heavy elements with additional opacity assured the quality of the fit. Given that no mechanism is expected to be at work in LB 1919 at the moment, this means that the stars must have entered the white dwarf cooling track with an already metal poor composition. The origin of this low metallicity must be found in an earlier evolutionary state.

The evolution of white dwarfs has already been outlined in chapter 2. It is important to keep in mind that due to their small initial mass, the progenitors of the white dwarf stars cannot fuse elements heavier than carbon and oxygen in their core. Heavier elements, which can be found in the spectra must have been present in the interstellar ingredients at the star formation process or must have been produced through the *s*-process at the later phase at the AGB in the HRD. White dwarfs possess relatively low luminosities. Therefore, they can only be observed up to close distances. Consequently, the interstellar matter their progenitors were formed in is located in the Galaxy.

In general, all stars can be divided into the three populations I, II, and III. The

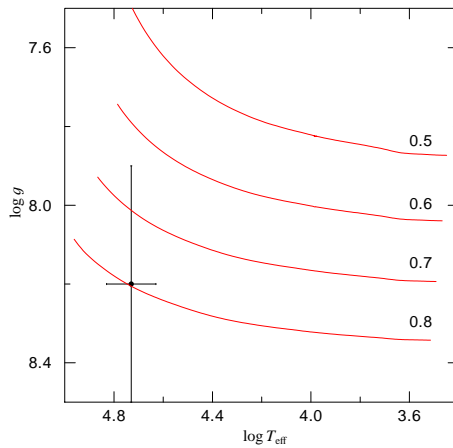


Figure 8.1: Position of LB 1919 in the $\log g - \log T_{\text{eff}}$ diagram. Evolutionary tracks for DA white dwarfs with different masses are taken from Althaus & Benvenuto (1998). The gravity is given in cm s^{-2} , effective temperature in K.

metallicity of the types decreases with increasing number. The metal free population III stars are only hypothetical and are very massive stars with up to $\sim 100M_{\odot}$, which lived for a short time at the beginning of the Universe. These stars are believed to have produced all heavy elements up to iron, which can now be found in a variety of stars. The population II stars with a low metallicity are old and were born in the metal poor left-overs of the population III stars. These stars still exist and are located in the halo of the galactic disk. The youngest and metal-richest stars are that of population I. Just like the Sun these objects are most likely to be found in the spiral arms of the Galaxy. The distribution of white dwarfs in the Galaxy were determined empirically. For the solar neighborhood densities of $5-5.6 \cdot 10^{-3} \text{pc}^{-3}$ were found (Ruiz & Bergeron 2001; Holberg et al. 2002). This observational evidence of the white dwarf population defines the WD luminosity function (LF) that can be taken to calculate the WD density in other parts of the Galaxy (Robin et al. 2003). Accordingly, for the thin disc a WD population of $6.6 \cdot 10^{-3} \text{pc}^{-3}$ can be expected. For the thick disc less observational constrains exist. Numerical simulations of the LF indicate a lower WD population of $5 \cdot 10^{-4} \text{pc}^{-3}$ (García-Berro et al. 1999; Robin et al. 2003). In the last years strong evidence for a significant white dwarf population in the population II-star rich galactic halo arrived (Koester 2002). Calculated luminosity functions, however, lack observational confirmation and are uncertain (Chabrier 1999). The number of halo white dwarfs can therefore only be assumed to be not higher than $2.8 \cdot 10^{-4} \text{pc}^{-3}$ (Robin et al. 2003).

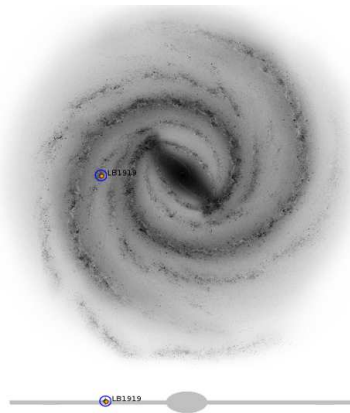


Figure 8.2: The position of LB 1919 in the Milky Way. At the galactic coordinates $l = 156.33$ and $b = +57.82$ and in a distance of 306 pc LB 1919 is labeled close to the Sun (spot). See text for details.

In order to conclude in what kind of environment LB 1919 is located, the distance has to be determined. The distance to the star on the other side can only be calculated if its mass is known. Depending on the mass, the evolution of the white dwarf takes different ways. Evolutionary tracks for DA white dwarfs with different masses, metallicities, and hydrogen envelopes thickness were computed by Althaus & Benvenuto (1998). For a comparison with the actual evolutionary state of LB 1919 the smallest metallicity ($z = 10^{-3}$) and the thickest hydrogen envelope with a fractional mass of $M_{\text{H}}/M_{\star} = 10^{-4}$ was assumed. The different evolutionary tracks for masses of $0.5 M_{\odot}$ to $0.8 M_{\odot}$ can be seen in figure 8.1. Accordingly, the mass of LB 1919 is $0.8 \pm 0.15 M_{\odot}$. Knowing the mass of the star as well as T_{eff} and $\log g$, makes it now possible to determine the distance following the flux calibration of Heber et al. (1984). With the Eddington flux at 5404 \AA , the corrected visual magnitude m_{V_0} that is defined by the visual magnitude of the star (16.8, Schwöpe et al. 2000) and the interstellar extinction $E(B-V)$ (see section 6.6) the distance in parsec is derived (Rauch et al. 1994),

$$d = 7.11 \cdot 10^4 \sqrt{H_{\nu} M 10^{0.4m_{V_0} - \log g}}. \quad (8.1)$$

In the previous analysis the parameters of LB 1919 have been derived, $T_{\text{eff}} = 54 \pm 2 \text{ kK}$, $\log g = 8.2 \pm 0.3$, and $H_{\nu} = 7.01 \cdot 10^{-4} \text{ erg cm}^{-2} \text{ sec}^{-1} \text{ Hz}^{-1}$. For these determined values of LB 1919 a distance of 306 pc is obtained. The galactic co-

ordinates of LB 1919 are $l = 156.33$ and $b = +57.82$, thus almost 58° above the galactic plane. With the coordinates and the distance the position of LB 1919 in the Milky Way can be mapped. This is shown in figure 8.2. The upper part of the figure shows the simulated top view of our Galaxy. The position of LB 1919 is labeled. The position of the Sun is marked with a spot at almost the same position. More important than the top perspective is the smaller inlay in figure 8.2 that shows the side view of the Milky Way. It is clear to see that LB 1919 is located in the galactic plane, hence, in the region of the population I stars. It can therefore be assumed that it was born in an at least slightly metal-rich environment.

If the white dwarf progenitors are not born in a metal free region, the metallicity must have been lowered during a later phase of their evolution. The question to answer is in what phase this could be the case. Shortly after the formation of the star it enters the zero age main sequence in the HRD. The time the star spends on the main sequence with the fusion of hydrogen to helium is the longest, but also the most unspectacular phase in the life of the star. The next eventful episode is marked by the expansion of the star's envelope and by entering the AGB. As mentioned before, heavier elements can be produced in that evolutionary phase. This, however, would rather increase the metal content of the star instead of lowering it. More important for a decrease of metallicity is the development during the red giant branch phases, where most of the mass-loss takes place. This mass-loss is important for the stellar evolution since it affects the luminosity of stars and the nucleosynthesis developing in their cores (Le Bertre et al. 2005). The mechanisms of mass-loss are diverse. One example are grains that are formed in the atmospheres of cool giant atmospheres. These grains consist either of C, SiC, or other silicates. They can then be ejected into the ISM by radiation pressure and lower the metal content in the stellar envelope (Knapp 1985). Another possibility are radiatively driven winds that act directly on the bound-bound transitions of specific ions. Considering the self-absorption of the lines, this would still result in a significant outward directed line acceleration that exceeds the repulsing gravitational force (Owocki 2005). These winds might work selectively on particular line features and could explain the relative deficiency of certain elements in the atmosphere. Indeed it has been shown that in thin winds the radiation pressure will only accelerate the metal ions while most of the matter composed of hydrogen and helium is not affected. This leads to the decoupling of the metal ions the so called *ion runaway* (Springmann & Pauldrach 1992). These winds cannot only occur in massive stars of spectral class O and B but also in Wolf-Rayet (WR) stars or in low-mass central stars of planetary nebulae, hence, in different phases of stellar evolution (Hamann 2010).

Only recently, Renedo et al. (2010) presented full evolutionary calculations appropriate for the study of hydrogen-rich DA white dwarfs. The computations in-

cluded every step in the development of the DAs and followed their progenitors from the zero-age main sequence through the core hydrogen-burning phase and the asymptotic giant branch phase, including the various thermal pulses (TP), to the white dwarf cooling sequence. In their models mass-loss is treated during the phases of helium-burning and the red giant branch phase (Schröder & Cuntz 2005) as well as during the AGB and the TP-AGB phases (Vassiliadis & Wood 1993). Element diffusion as one of the major physical processes that change the chemical abundance distribution of white dwarfs is incorporated, radiative levitation on the other hand is neglected. This might underestimate the exact surface abundances of elements in the final white dwarf stage, it does, however, not affect the prior evolution of the white dwarf progenitor.

The results show a initial-final mass ratio (IFMR) in accordance with Salaris et al. (2009). The IFMR is important since it provides information about the expected WD mass on the cooling sequence and an estimate of the mass-loss during the stellar evolution when the initial main sequence mass of a formed star is known. For a WD mass of $0.7\text{--}0.8 M_{\odot}$ the initial mass on the zero age main sequence is about $3\text{--}4 M_{\odot}$. The mass-loss on the AGB is in the range $2.2\text{--}3.1 M_{\odot}$. The number of thermal pulses on the AGB varies from 15–19. These results hold for WD progenitors with a metal content representative for the solar neighborhood, hence suitable for LB 1919. The number of thermal pulses and the associated mass-loss can be an indicator for a possible decrease in the metal content.

As a conclusion it can be stated that the reason for the metal poor nature of LB 1919 cannot be explained in terms of an investigation of the photospheric properties in the white dwarf configuration of the star. Possible mechanisms for a depletion of the metal content of LB 1919 in an earlier evolutionary state exist. To put these in a relation to the actual history of LB 1919 is complicated by the lack of observational data of earlier evolutionary phases. Evolutionary calculations concentrating on the exact metal content of heavier elements including mass-loss and radiatively driven winds during the evolution of the star as well as radiative levitation in the white dwarf stage could improve the knowledge about the class of the metal poor white dwarf stars further.

8.2 PG 1520+525

The PG 1159 star PG 1520+525 was investigated in chapter 7. The comparison of the LETG *Chandra* spectrum with calculated model atmospheres allowed a precise temperature determination. The results confirmed the value determined by Dreizler & Heber (1998). This is necessary to determine the exact position of the not pulsating PG 1520+525 in the $T_{\text{eff}}\text{-log } g$ diagram with respect to its spectroscopic

twin the pulsating PG 1159 prototype PG 1159-035. Both stars constrain the blue edge of the GW Vir instability strip, thus the separation between pulsating and non-pulsating PG 1159 stars. Pulsation models investigate the reason for the occurrence or the absence of the κ -mechanism, which causes the pulsations, in stars with similar spectroscopic characteristics. They now can make use of an additional constraint for their comparison of model and the real star's properties.

To conclude, the exact determination of T_{eff} and $\log g$ of the non-pulsating PG 1159 star PG 1520+525 in the temperature sensitive soft X-ray wavelength range made it possible to constrain the blue edge of the GW Vir instability strip in the $T_{\text{eff}}\text{-}\log g$ diagram. An uncertainty arises from the larger error bars for the $\log g$ value. The soft X-ray range is not sensitive enough to changes in $\log g$ to determine a more precise result. However, a wide spacing in the $\log g$ grid for the determination of these values was used in previous investigations. Therefore, the error bars might be smaller than assumed, leading to a further constraint of the position of the strip.

Bibliography

- Abbott, D. C. 1982, *ApJ*, 259, 282
- Aller, L. H. 1959, *PASP*, 71, 324
- Althaus, L. G. & Benvenuto, O. G. 1998, *MNRAS*, 296, 206
- Althaus, L. G., Serenelli, A. M., Panei, J. A., et al. 2005, *A&A*, 435, 631
- Aschenbach, B., Braeuninger, H., Briel, U., et al. 1981, *Space Science Reviews*, 30, 569
- Asplund, M., Grevesse, N., Sauval, A. J., & Scott, P. 2009, *ARA&A*, 47, 481
- Auer, L. H. & Mihalas, D. 1968, *ApJ*, 151, 311
- . 1969, *ApJ*, 158, 641
- Baranov, V. B., Krasnobaev, K. V., & Kulikovskii, A. G. 1970, *Akademiia Nauk SSSR Doklady*, 194, 41
- Barstow, M. A. 1989, in *Lecture Notes in Physics*, Berlin Springer Verlag, Vol. 328, IAU Colloq. 114: White Dwarfs, ed. G. Wegner, 156–159
- Barstow, M. A., Dobbie, P. D., Holberg, J. B., Hubeny, I., & Lanz, T. 1997, *MNRAS*, 286, 58
- Barstow, M. A., Fleming, T. A., Diamond, C. J., & Finley, D. S. 1992, in *Lecture Notes in Physics*, Berlin Springer Verlag, Vol. 401, *The Atmospheres of Early-Type Stars*, ed. U. Heber & C. S. Jeffery, 329
- Barstow, M. A., Fleming, T. A., Diamond, C. J., et al. 1993, *MNRAS*, 264, 16
- Barstow, M. A., Good, S. A., Burleigh, M. R., et al. 2003a, *MNRAS*, 344, 562
- Barstow, M. A., Good, S. A., Holberg, J. B., et al. 2002, *MNRAS*, 330, 425
- . 2003b, *MNRAS*, 341, 870
- Barstow, M. A. & Holberg, J. B. 2003, *Extreme Ultraviolet Astronomy*, ed. Barstow, M. A. & Holberg, J. B.
- Bergeron, P., Wesemael, F., Beauchamp, A., et al. 1994, *ApJ*, 432, 305
- Bergeron, P., Wesemael, F., Lamontagne, R., et al. 1995, *ApJ*, 449, 258
- Beuermann, K., Burwitz, V., & Rauch, T. 2007, in *Astronomical Society of the Pacific Conference Series*, Vol. 372, 15th European Workshop on White Dwarfs, ed. R. Napiwotzki & M. R. Burleigh, 221–+
- Blöcker, T. 1995, *A&A*, 299, 755
- Boothroyd, A. I. 2006, *Science*, 314, 1690
- Bowyer, S., Lampton, M., Lewis, J., et al. 1996, *ApJS*, 102, 129
- Bowyer, S. & Malina, R. F. 1991, *Advances in Space Research*, 11, 205
- Bruhweiler, F. C. & Kondo, Y. 1983, *ApJ*, 269, 657
- Cannon, C. J. 1973, *Journal of Quantitative Spectroscopy and Radiative Transfer*, 13, 627
- Chabrier, G. 1999, *ApJ*, 513, L103
- Chandrasekhar, S. 1935, *MNRAS*, 95, 207
- . 1939, *An introduction to the study of stellar structure*, ed. Chandrasekhar, S.
- Chayer, P., Fontaine, G., & Wesemael, F. 1989, in *Lecture Notes in Physics*, Berlin

- Springer Verlag, Vol. 328, IAU Colloq. 114: White Dwarfs, ed. G. Wegner, 253–257
- Chayer, P., Fontaine, G., & Wesemael, F. 1995a, *ApJS*, 99, 189
- Chayer, P., Fontaine, G., Wesemael, F., & Michaud, G. 1987, in IAU Colloq. 95: Second Conference on Faint Blue Stars, ed. A. G. D. Philip, D. S. Hayes, & J. W. Liebert, 653–656
- Chayer, P., Kruk, J. W., Vennes, S., & Dupuis, J. 2001, in *Astronomical Society of the Pacific Conference Series*, Vol. 226, 12th European Workshop on White Dwarfs, ed. J. L. Provencal, H. L. Shipman, J. MacDonald, & S. Goodchild, 90
- Chayer, P., LeBlanc, F., Fontaine, G., et al. 1994, *ApJ*, 436, L161
- Chayer, P., Vennes, S., Dupuis, J., & Kruk, J. W. 2005, *ApJ*, 630, L169
- Chayer, P., Vennes, S., Pradhan, A. K., et al. 1995b, *ApJ*, 454, 429
- Chu, Y., Gruendl, R. A., Williams, R. M., Gull, T. R., & Werner, K. 2004a, *AJ*, 128, 2357
- Chu, Y., Guerrero, M. A., Gruendl, R. A., & Webbink, R. F. 2004b, *AJ*, 127, 477
- Córsico, A. H., Althaus, L. G., Miller Bertolami, M. M., & Werner, K. 2007, *A&A*, 461, 1095
- Cowan, R. D. 1968, *J. Opt. Soc. Am.*, 58, 808
- Cox, D. P. & Reynolds, R. J. 1987, *ARA&A*, 25, 303
- Cruddace, R., Paresce, F., Bowyer, S., & Lampton, M. 1974, *ApJ*, 187, 497
- Czerny, B. & Nikolajuk, M. 2009, *ArXiv e-prints*
- Dreizler, S. 1998, *Baltic Astronomy*, 7, 71
- Dreizler, S. 1999a, in *Astronomical Society of the Pacific Conference Series*, Vol. 169, 11th European Workshop on White Dwarfs, ed. S.-E. Solheim & E. G. Meistas, 499
- . 1999b, *A&A*, 352, 632
- Dreizler, S. 2003, in *Astronomical Society of the Pacific Conference Series*, Vol. 288, *Stellar Atmosphere Modeling*, ed. I. Hubeny, D. Mihalas, & K. Werner, 69
- Dreizler, S. & Heber, U. 1998, *A&A*, 334, 618
- Dupuis, J. 2002, in *Astronomical Society of the Pacific Conference Series*, Vol. 264, *Continuing the Challenge of EUV Astronomy: Current Analysis and Prospects for the Future*, ed. S. B. Howell, J. Dupuis, D. Golombek, F. M. Walter, & J. Cullison, 15
- Dupuis, J., Vennes, S., Bowyer, S., Pradhan, A. K., & Thejll, P. 1995, *ApJ*, 455, 574
- Finley, D. S., Koester, D., & Basri, G. 1997, *ApJ*, 488, 375
- Fleming, T. A., Liebert, J., & Green, R. F. 1986, *ApJ*, 308, 176
- Fleming, T. A., Snowden, S. L., Pfeffermann, E., Briel, U., & Greiner, J. 1996, *A&A*, 316, 147
- Fontaine, G., Brassard, P., & Bergeron, P. 2001, *PASP*, 113, 409
- Fontaine, G. & Michaud, G. 1979, *ApJ*, 231, 826
- Fontaine, G. & Wesemael, F. 1991, in *IAU Symposium*, Vol. 145, *Evolution of Stars: the Photospheric Abundance Connection*, ed. G. Michaud & A. V. Tutukov, 421
- Fontaine, G. & Wesemael, F. 1997, in *Astrophysics and Space Science Library*, Vol. 214, *White dwarfs*, ed. J. Isern, M. Hernanz, & E. Garcia-Berro, 173
- García-Berro, E., Torres, S., Isern, J., & Burkert, A. 1999, *MNRAS*, 302, 173
- Gautschy, A. 1997, *A&A*, 320, 811
- Gautschy, A., Althaus, L. G., & Saio, H. 2005, *A&A*, 438, 1013
- Gautschy, A., Ludwig, H., & Freytag, B. 1996, *A&A*, 311, 493

- Gonzalez, J., LeBlanc, F., Artru, M., & Michaud, G. 1995, *A&A*, 297, 223
- Groenewegen, M. A. T., Smith, C. H., Wood, P. R., Omont, A., & Fujiyoshi, T. 1995, *ApJ*, 449, 119
- Güver, T. & Özel, F. 2009, *MNRAS*, 400, 2050
- Hamann, W. 2010, *Ap&SS*, 119
- Hasinger, G. 1985, *Bulletin d'Information du Centre de Données Stellaires*, 28, 87
- Hauschildt, P. H. & Baron, E. 1999, *Journal of Computational and Applied Mathematics*, 109, 41
- Heber, U., Hunger, K., Jonas, G., & Kudritzki, R. P. 1984, *A&A*, 130, 119
- Heber, U., Napiwotzki, R., & Reid, I. N. 1997, *A&A*, 323, 819
- Heise, J., Paerels, F. B. S., Bleeker, J. A. M., & Brinkman, A. C. 1988, *ApJ*, 334, 958
- Holberg, J. B., Oswalt, T. D., & Sion, E. M. 2002, *ApJ*, 571, 512
- Hubeny, I. 1992, in *Lecture Notes in Physics*, Berlin Springer Verlag, Vol. 401, *The Atmospheres of Early-Type Stars*, ed. U. Heber & C. S. Jeffery, 377
- Hubeny, I. & Lanz, T. 2000, *SYNSPEC: A User's Guide*, version 43
- Hubeny, I., Mihalas, D., & Werner, K., eds. 2003, *Astronomical Society of the Pacific Conference Series*, Vol. 288, *Stellar Atmosphere Modeling*
- Hummer, D. G. & Mihalas, D. 1988, *ApJ*, 331, 794
- Jahn, D. 2005, *Analyse des HST/STIS-Spektrums von PG1159-035*, Diploma thesis, Univ. of Tübingen
- Jahn, D., Rauch, T., Reiff, E., et al. 2007, *A&A*, 462, 281
- Kahn, S. M., Wesemael, F., Liebert, J., et al. 1984, *ApJ*, 278, 255
- Kawaler, S. D. 2003, *ArXiv Astrophysics e-prints*
- Kippenhahn, R. & Weigert, A. 1994, *Stellar Structure and Evolution*, ed. Kippenhahn, R. & Weigert, A.
- Knapp, G. R. 1985, *ApJ*, 293, 273
- Koester, D. 1976, *A&A*, 52, 415
- 1989, *ApJ*, 342, 999
- 2002, *A&A Rev.*, 11, 33
- Koester, D. & Chanmugam, G. 1990, *Reports on Progress in Physics*, 53, 837
- Koester, D., Dreizler, S., Weidemann, V., & Allard, N. F. 1999, in *Astronomical Society of the Pacific Conference Series*, Vol. 169, *11th European Workshop on White Dwarfs*, ed. S.-E. Solheim & E. G. Meistas, 415
- Koester, D., Voss, B., Napiwotzki, R., et al. 2009, *A&A*, 505, 441
- Kovetz, A. & Shaviv, G. 1970, *A&A*, 8, 398
- Kurucz, R. 1993, *ATLAS9 Stellar Atmosphere Programs and 2 km/s grid*. Kurucz CD-ROM No. 13. Cambridge, Mass.: Smithsonian Astrophysical Observatory, 1993., 13
- 2009, Kurucz Atoms database, <http://kurucz.harvard.edu/atoms.html>
- Kurucz, R. L. 1991, in *NATO ASIC Proc. 341: Stellar Atmospheres - Beyond Classical Models*, 441
- Kwok, S. 2005, *Journal of Korean Astronomical Society*, 38, 271
- Landenberger-Schuh, S. 2005, PhD thesis, Univ. of Tübingen
- Le Bertre, T., Gérard, E., & Winters, J. M. 2005, in *ESA Special Publication*, Vol. 577, *ESA Special Publication*, ed. A. Wilson, 217–222
- Liebert, J., Bergeron, P., & Holberg, J. B. 2005, *ApJS*, 156, 47
- Lucy, L. B. 1964, *SAO Special Report*, 167, 93
- MacDonald, J. 1992, *ApJ*, 394, 619
- MacDonald, J. & Vennes, S. 1991, *ApJ*, 371, 719
- Marsh, M. C., Barstow, M. A., Buckley,

- D. A., et al. 1997a, *MNRAS*, 286, 369
 —. 1997b, *MNRAS*, 287, 705
 Mason, K. O., Hassall, B. J. M., Bromage, G. E., et al. 1995, *MNRAS*, 274, 1194
 Massacrier, G. 1996, *A&A*, 309, 979
 Massacrier, G. & El-Murr, K. 1996, *A&A*, 312, L25
 McCook, G. P. & Sion, E. M. 1999, *ApJS*, 121, 1
 Mestel, L. 1952, *MNRAS*, 112, 583
 Mestel, L. & Ruderman, M. A. 1967, *MNRAS*, 136, 27
 Mewe, R., Heise, J., Gronenschild, E. H. B. M., et al. 1975a, *ApJ*, 202, L67
 —. 1975b, *Nature*, 256, 711
 Michaud, G. 1970, *ApJ*, 160, 641
 Michaud, G. & Fontaine, G. 1979, *ApJ*, 229, 694
 Mihalas, D. 1970, *Stellar atmospheres*, ed. Mihalas, D.
 Mihalas, D. M. 1982, *Stellar atmospheres*, ed. Mihalas, D. M.
 Miller, A. 1997, *EUVE Guest Observer Program Handbook*, 4th Edition, ed. Miller, A.
 Miller Bertolami, M. M. & Althaus, L. G. 2006, *A&A*, 454, 845
 Montgomery, M. H. & Kupka, F. 2004, *MNRAS*, 350, 267
 Morvan, E., Vauclair, G., & Vauclair, S. 1986, *A&A*, 163, 145
 Murray, S. S. 2001, in *Astronomical Society of the Pacific Conference Series*, Vol. 238, *Astronomical Data Analysis Software and Systems X*, ed. F. R. Harnden Jr., F. A. Primini, & H. E. Payne, 13
 Nagel, T., Dreizler, S., Rauch, T., & Werner, K. 2004, *A&A*, 428, 109
 Napiwotzki, R. 2010, *White Dwarfs*: <http://star.herts.ac.uk/progs/whitedwarf.html>
 Napiwotzki, R., Christlieb, N., Drechsel, H., et al. 2001, *Astronomische Nachrichten*, 322, 411
 Napiwotzki, R., Green, P. J., & Saffer, R. A. 1999, *ApJ*, 517, 399
 O'Dwyer, I. J., Chu, Y., Gruendl, R. A., Guerrero, M. A., & Webbink, R. F. 2003, *AJ*, 125, 2239
 Oliveira, C. M., Hébrard, G., Howk, J. C., et al. 2003, *ApJ*, 587, 235
 Olofsson, H. 2001, in *Astronomical Society of the Pacific Conference Series*, Vol. 235, *Science with the Atacama Large Millimeter Array*, ed. A. Wootten, 355
 Owocki, S. 2005, in *Astronomical Society of the Pacific Conference Series*, Vol. 332, *The Fate of the Most Massive Stars*, ed. R. Humphreys & K. Stanek, 169
 Paerels, F. B. S., Bleeker, J. A. M., Brinkman, A. C., & Heise, J. 1988, *ApJ*, 329, 849
 Palla, F. 2001, in *Astronomical Society of the Pacific Conference Series*, Vol. 243, *From Darkness to Light: Origin and Evolution of Young Stellar Clusters*, ed. T. Montmerle & P. André, 525
 Parker, E. N. 1961, *ApJ*, 134, 20
 Pounds, K. A., Allan, D. J., Barber, C., et al. 1993, *MNRAS*, 260, 77
 Press, W. H., Teukolsky, S. A., Vetterling, W. T., & Flannery, B. P. 1992, *Numerical recipes in FORTRAN. The art of scientific computing*, ed. T. S. A. V. W. T. . F. B. P. Press, W. H.
 Proffitt, C. R., Sansonetti, C. J., & Reader, J. 2001, *ApJ*, 557, 320
 Quirion, P. 2009, *Communications in Asteroseismology*, 159, 99
 Quirion, P., Fontaine, G., & Brassard, P. 2004, *ApJ*, 610, 436
 —. 2006, *Memorie della Societa Astronomica Italiana*, 77, 53
 —. 2007, *Communications in Asteroseismology*, 150, 247
 Rauch, T. & Deetjen, J. L. 2003, in *As-*

- tronomical Society of the Pacific Conference Series, Vol. 288, Stellar Atmosphere Modeling, ed. I. Hubeny, D. Mihalas, & K. Werner, 103
- Rauch, T., Koepfen, J., & Werner, K. 1994, *A&A*, 286, 543
- Renedo, I., Althaus, L. G., Miller Bertolami, M. M., et al. 2010, *ApJ*, 717, 183
- Richer, J., Michaud, G., & Massacrier, G. 1997, *A&A*, 317, 968
- Richmond, M. 2007, Late stages of evolution for low-mass stars, lecture notes: <http://spiff.rit.edu/classes/phys230/lectures/planneb/planneb.html>
- Robin, A. C., Reyl e, C., Derri ere, S., & Picaud, S. 2003, *A&A*, 409, 523
- Roxburgh, I. W. 1965, *Zeitschrift fur Astrophysik*, 62, 134
- Ruiz, M. T. & Bergeron, P. 2001, *ApJ*, 558, 761
- Rumph, T., Bowyer, S., & Vennes, S. 1994, *AJ*, 107, 2108
- Saio, H. 1996, in *Astronomical Society of the Pacific Conference Series*, Vol. 96, Hydrogen Deficient Stars, ed. C. S. Jeffery & U. Heber, 361
- Salaris, M., Serenelli, A., Weiss, A., & Miller Bertolami, M. 2009, *ApJ*, 692, 1013
- Salpeter, E. E. 1961, *ApJ*, 134, 669
- Schr oder, K. & Cuntz, M. 2005, *ApJ*, 630, L73
- Schuh, S. 2000, Gleichgewichtshaeufigkeiten in hei en Wei en Zwergen, Diploma thesis, Univ. of T bingen
- Schuh, S. L., Dreizler, S., & Wolff, B. 2002, *A&A*, 382, 164
- Schwobe, A., Hasinger, G., Lehmann, I., et al. 2000, *Astronomische Nachrichten*, 321, 1
- Seaton, M. J. 1958, *Reviews of Modern Physics*, 30, 979
- Seaton, M. J. 1995, *Journal of Physics B: Atomic, Molecular and Optical Physics*, 28, 3185
- Seaton, M. J., Yan, Y., Mihalas, D., & Pradhan, A. K. 1994, *MNRAS*, 266, 805
- Shipman, H. L. 1976, *ApJ*, 206, L67
- Sion, E. M., Liebert, J., & Starrfield, S. G. 1985, *ApJ*, 292, 471
- Sommerfeld, A. 1939, *Atombau und Spektrellinien*, vol. 2, 5th ed., Braunschweig
- Springmann, U. W. E. & Pauldrach, A. W. A. 1992, *A&A*, 262, 515
- Starrfield, S., Cox, A. N., Kidman, R. B., & Pesnell, W. D. 1984, *ApJ*, 281, 800
- Starrfield, S. G., Cox, A. N., Hodson, S. W., & Pesnell, W. D. 1983, *ApJ*, 268, L27
- Tomlin, S. 1999, *Nature*, 401, 32
- Tr mper, J. E. & Hasinger, G. 2008, *The Universe in X-Rays*, ed. Tr mper, J. E. & Hasinger, G.
- Ungraub, K. & Bues, I. 1994, in *Astronomische Gesellschaft Abstract Series*, Vol. 10, *Astronomische Gesellschaft Abstract Series*, ed. G. Klare, 61
- Ungraub, K. & Bues, I. 1998, *A&A*, 338, 75
- van Kerkwijk, M. H. 2004, in *Compact Stars: The Quest for New States of Dense Matter*, ed. D. K. Hong, C.-H. Lee, H. K. Lee, D.-P. Min, T.-S. Park, & M. Rho, 116
- Vassiliadis, E. & Wood, P. R. 1993, *ApJ*, 413, 641
- Vauclair, G. 1987, in *IAU Colloq. 95: Second Conference on Faint Blue Stars*, ed. A. G. D. Philip, D. S. Hayes, & J. W. Liebert, 341–349
- Vauclair, G. 1989, in *Lecture Notes in Physics*, Berlin Springer Verlag, Vol. 328, *IAU Colloq. 114: White Dwarfs*, ed. G. Wegner, 176–187
- Vauclair, G., Vauclair, S., & Greenstein, J. L. 1979, *A&A*, 80, 79
- Vauclair, S. & Vauclair, G. 1982, *ARA&A*,

- 20, 37
- Vennes, S. 1992, *ApJ*, 390, 590
- Vennes, S., Chayer, P., & Dupuis, J. 2005, *ApJ*, 622, L121
- Vennes, S. & Dupuis, J. 2002, in *Astronomical Society of the Pacific Conference Series*, Vol. 262, *The High Energy Universe at Sharp Focus: Chandra Science*, ed. E. M. Schlegel & S. D. Vrtilik, 57
- Vennes, S., Pelletier, C., Fontaine, G., & Wesemael, F. 1988, *ApJ*, 331, 876
- Vennes, S., Thejll, P. A., Galvan, R. G., & Dupuis, J. 1997, *ApJ*, 480, 714
- Weidemann, V. & Koester, D. 1984, *A&A*, 132, 195
- Weisskopf, M. C., Tananbaum, H. D., Van Speybroeck, L. P., & O'Dell, S. L. 2000, in *Presented at the Society of Photo-Optical Instrumentation Engineers (SPIE) Conference*, Vol. 4012, *Society of Photo-Optical Instrumentation Engineers (SPIE) Conference Series*, ed. J. E. Truemper & B. Aschenbach, 2–16
- Werner, K. 1986, *A&A*, 161, 177
- . 1988, *A&A*, 204, 159
- Werner, K. 1992, in *Lecture Notes in Physics*, Berlin Springer Verlag, Vol. 401, *The Atmospheres of Early-Type Stars*, ed. U. Heber & C. S. Jeffery, 273
- Werner, K., Deetjen, J. L., Dreizler, S., et al. 2003, in *Astronomical Society of the Pacific Conference Series*, Vol. 288, *Stellar Atmosphere Modeling*, ed. I. Hubeny, D. Mihalas, & K. Werner, 31
- Werner, K., Drake, J. J., Rauch, T., Schuh, S., & Gautschy, A. 2007, in *Astronomical Society of the Pacific Conference Series*, Vol. 372, *15th European Workshop on White Dwarfs*, ed. R. Napiwotzki & M. R. Burleigh, 225
- Werner, K. & Dreizler, S. 1994, *A&A*, 286, L31
- . 1999, *Journal of Computational and Applied Mathematics*, 109, 65
- Werner, K., Heber, U., & Hunger, K. 1991, *A&A*, 244, 437
- Werner, K. & Herwig, F. 2006, *PASP*, 118, 183
- Werner, K. & Husfeld, D. 1985, *A&A*, 148, 417
- Werner, K., Rauch, T., Barstow, M. A., & Kruk, J. W. 2004a, *A&A*, 421, 1169
- Werner, K., Rauch, T., & Dreizler, S. 2010, *A User's Guide to the Tübingen NLTE Model Atmosphere Package*: <http://astro.uni-tuebingen.de/~rauch/TMAP/UserGuide/UserGuide.html>
- Werner, K., Rauch, T., & Kruk, J. W. 2008a, in *Astronomical Society of the Pacific Conference Series*, Vol. 391, *Hydrogen-Deficient Stars*, ed. A. Werner & T. Rauch, 239
- Werner, K., Rauch, T., Reiff, E., & Kruk, J. W. 2008b, in *Astronomical Society of the Pacific Conference Series*, Vol. 391, *Hydrogen-Deficient Stars*, ed. A. Werner & T. Rauch, 109
- Werner, K., Rauch, T., Reiff, E., Kruk, J. W., & Napiwotzki, R. 2004b, *A&A*, 427, 685
- Wesemael, F. 1978, *A&A*, 65, 301
- . 1979, *A&A*, 72, 104
- Wesemael, F., Green, R. F., & Liebert, J. 1985, *ApJS*, 58, 379
- Wickramasinghe, D. T. & Ferrario, L. 2000, *PASP*, 112, 873
- Wolff, B., Koester, D., Dreizler, S., & Haas, S. 1998a, *A&A*, 329, 1045
- . 1998b, *A&A*, 329, 1045
- Wolff, B., Koester, D., & Lallement, R. 1999, *A&A*, 346, 969
- Wolff, B., Kruk, J. W., Koester, D., et al. 2001, *A&A*, 373, 674
- Wood, M. A. 1992, *ApJ*, 386, 539
- Zijlstra, A. 2002, *Stellar Evolution: a summary*. Lecture notes <http://iapetus.phy.umist.ac.uk/Teaching/IntroAstro/StellarEvolution.html>

APPENDIX A

***Chandra* plots**

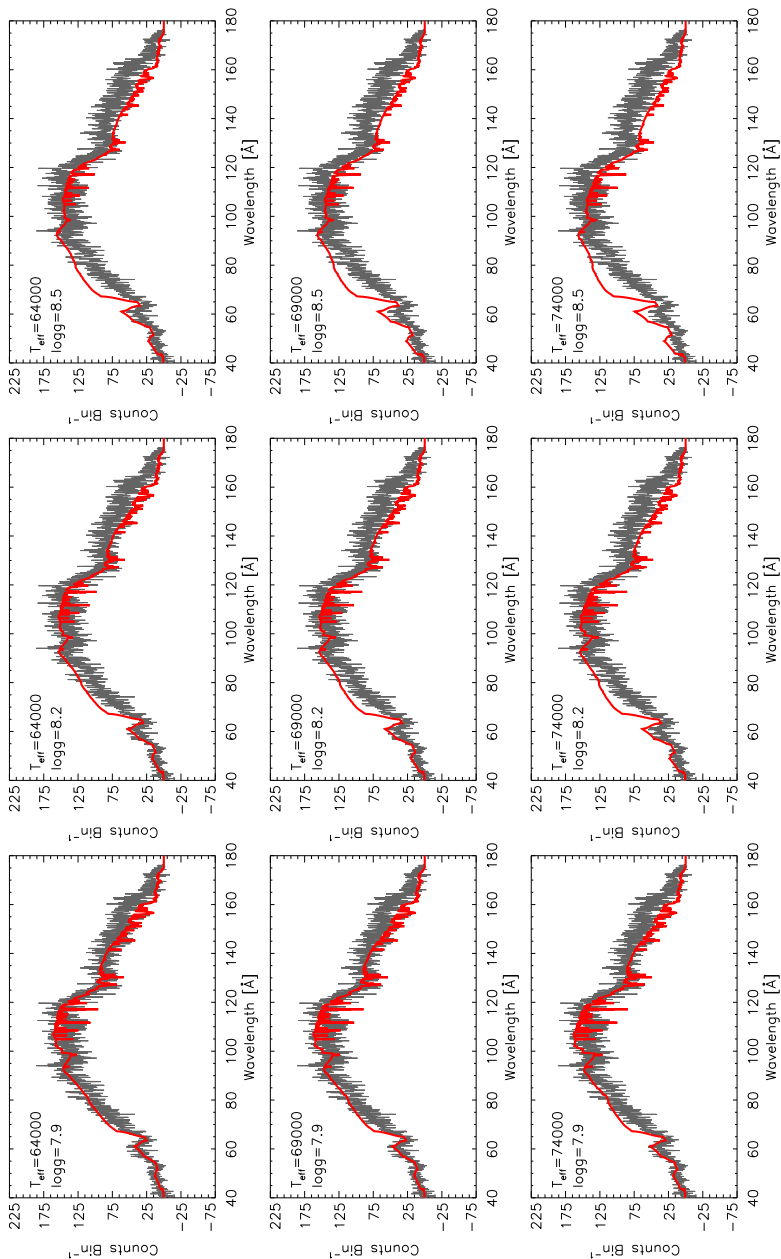


Figure A.1: *Chandra* spectra of LB 1919 (thin lines) with overplotted homogeneous models calculated with hydrogen and iron for $T_{\text{eff}} = 64\text{--}74$ kK and $\log g = 7.9\text{--}8.5$ (thick lines).

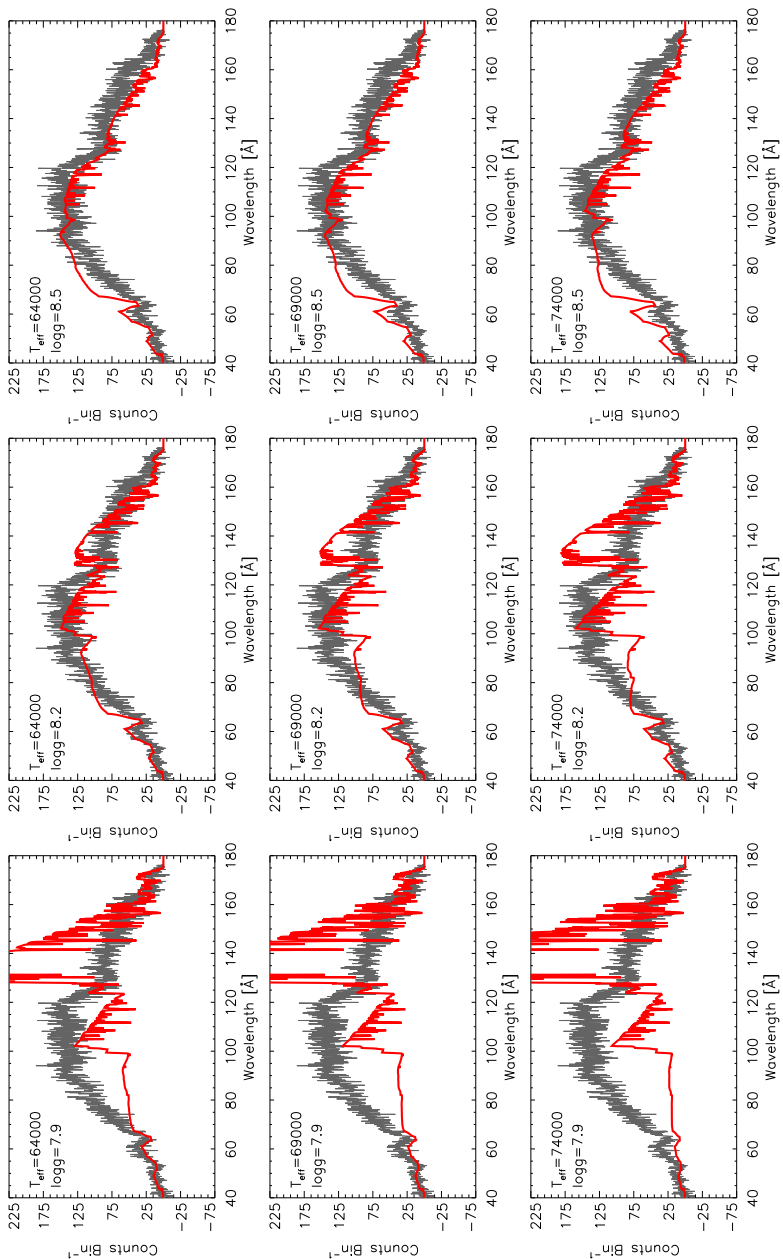


Figure A.2: *Chandra* spectra of LB 1919 (thin lines) with overlotted stratified models calculated with hydrogen and iron for $T_{\text{eff}} = 64\text{--}74$ kK and $\log g = 7.9\text{--}8.5$ (thick lines).

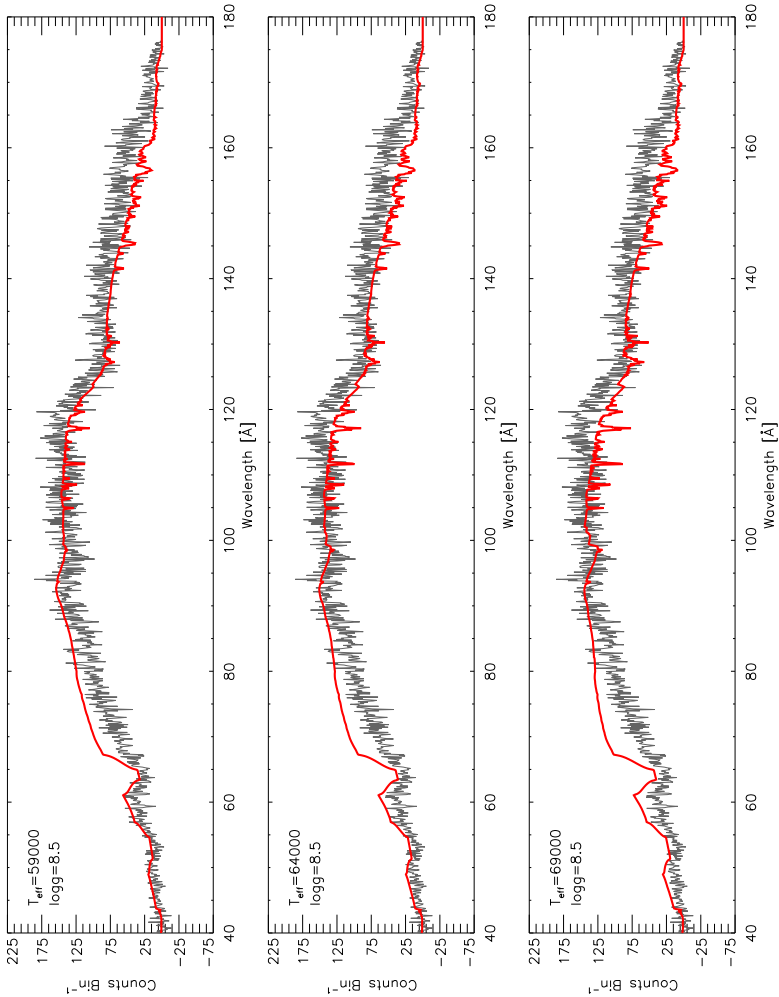


Figure A.3: *Chandra* spectra of LB 1919 (thin lines) with overplotted stratified models calculated with hydrogen, iron, $T_{\text{eff}} = 59\text{--}69$ kK, and $\log g = 8.5$ (thick lines).

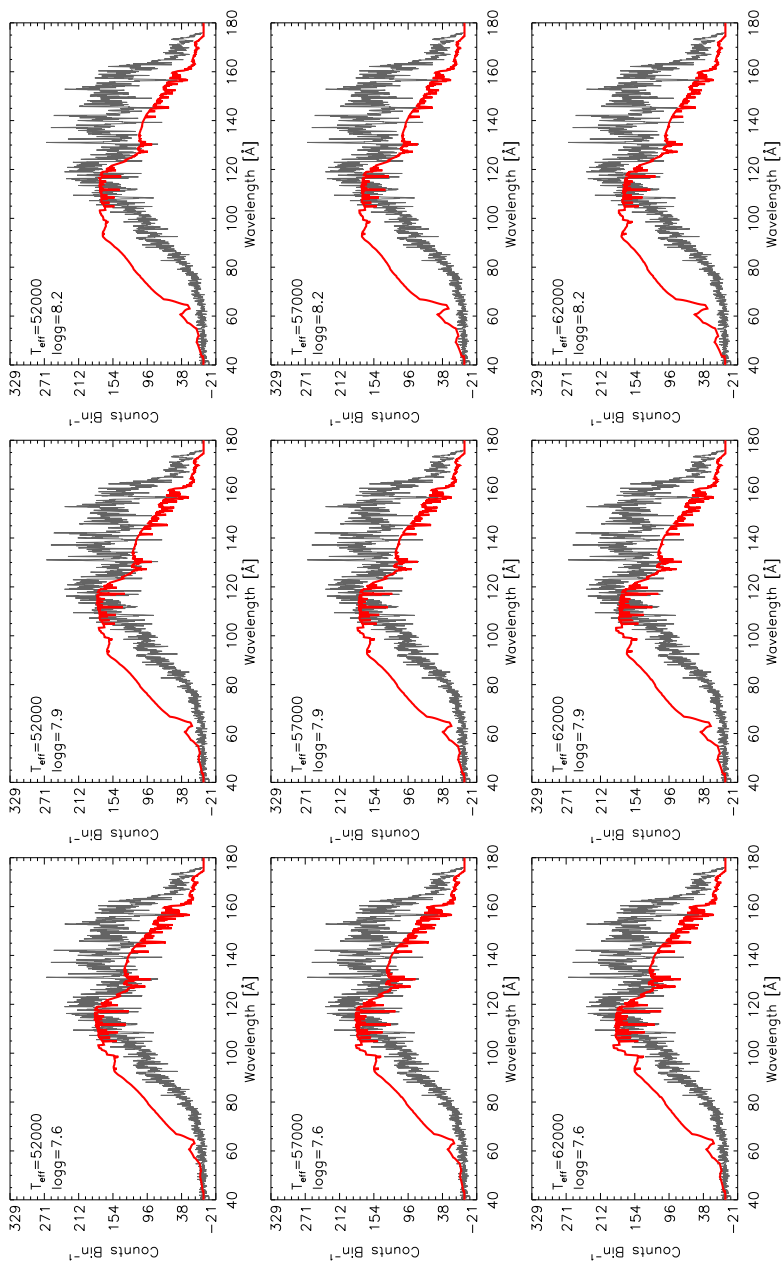


Figure A.4: *Chandra* spectra of GD 246 (thin lines) with overplotted homogeneous models calculated with hydrogen and iron for $T_{\text{eff}} = 52\text{--}62$ kK and $\log g = 7.6\text{--}8.2$ (thick lines).

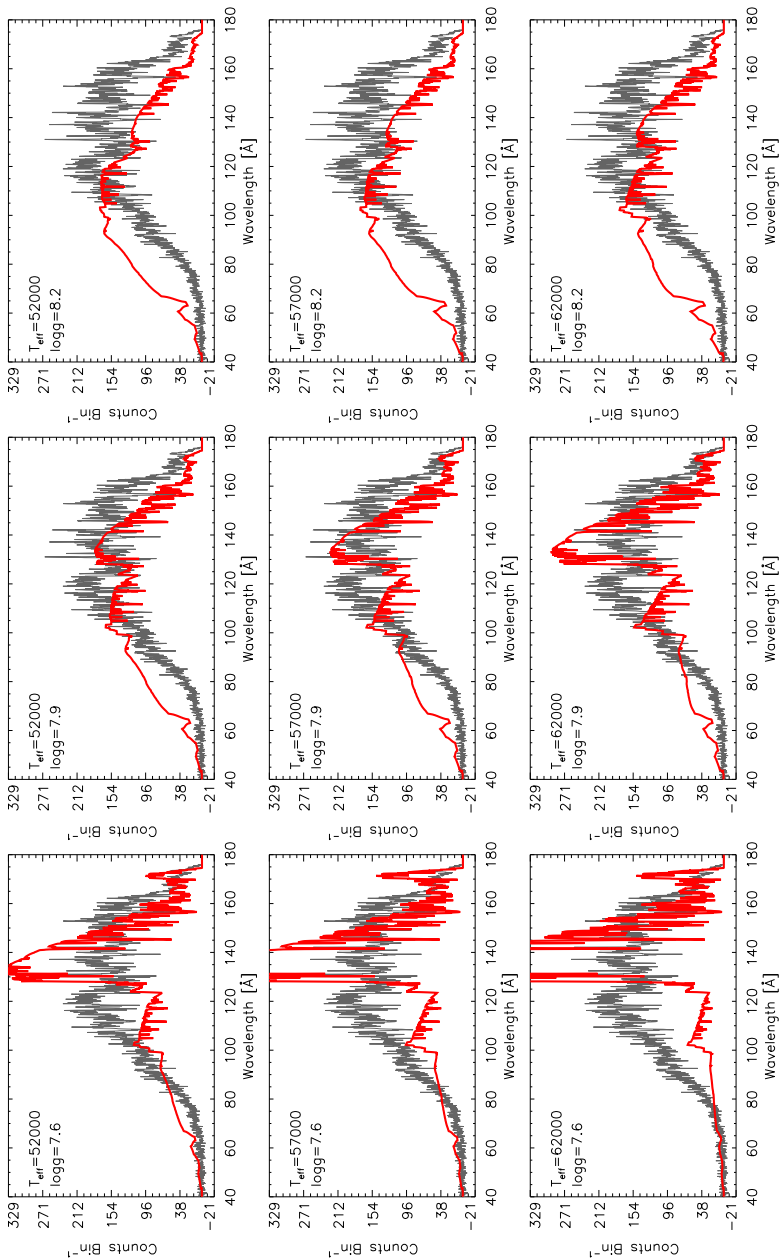


Figure A.5: *Chandra* spectra of GD 246 (thin lines) with overplotted stratified models calculated with hydrogen and iron for $T_{\text{eff}} = 52\text{--}62$ kK and $\log g = 7.6\text{--}8.2$ (thick lines).

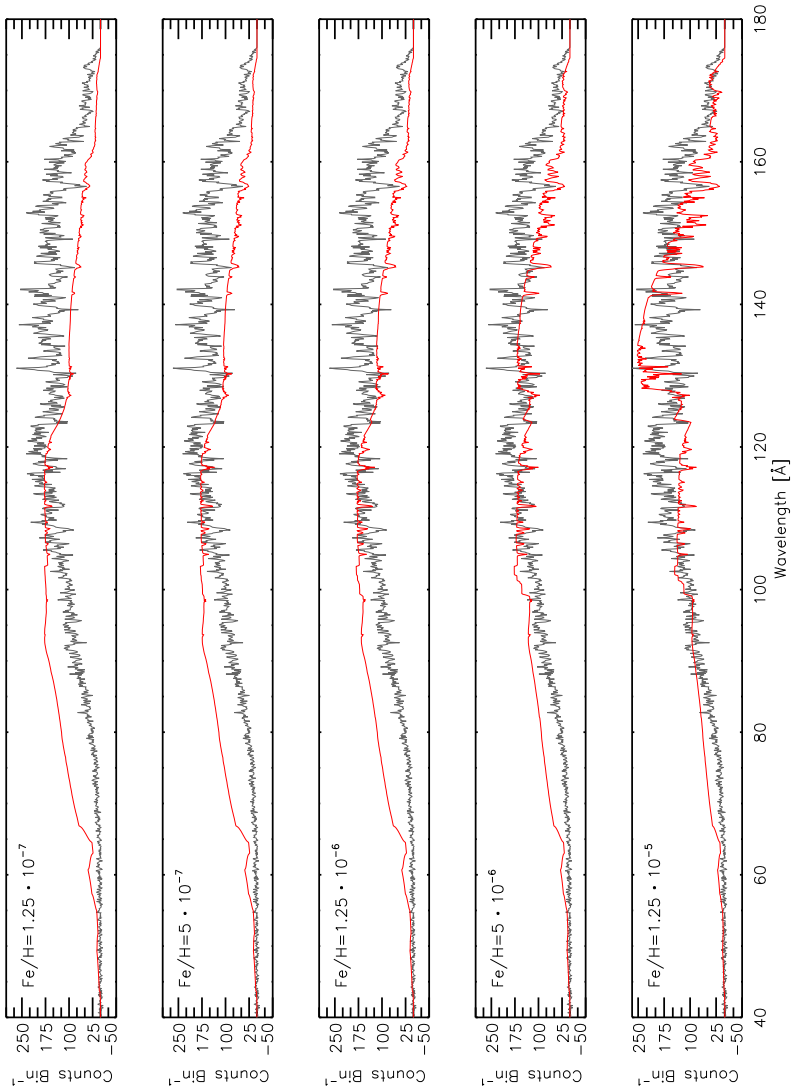


Figure A.6: Determination of Fe abundance in the *Chandra* spectrum of GD 246 (thin line). The model atmospheres with H and Fe (thick line) are calculated with $T_{\text{eff}} = 57000\text{K}$ and $\log g = 7.90$.

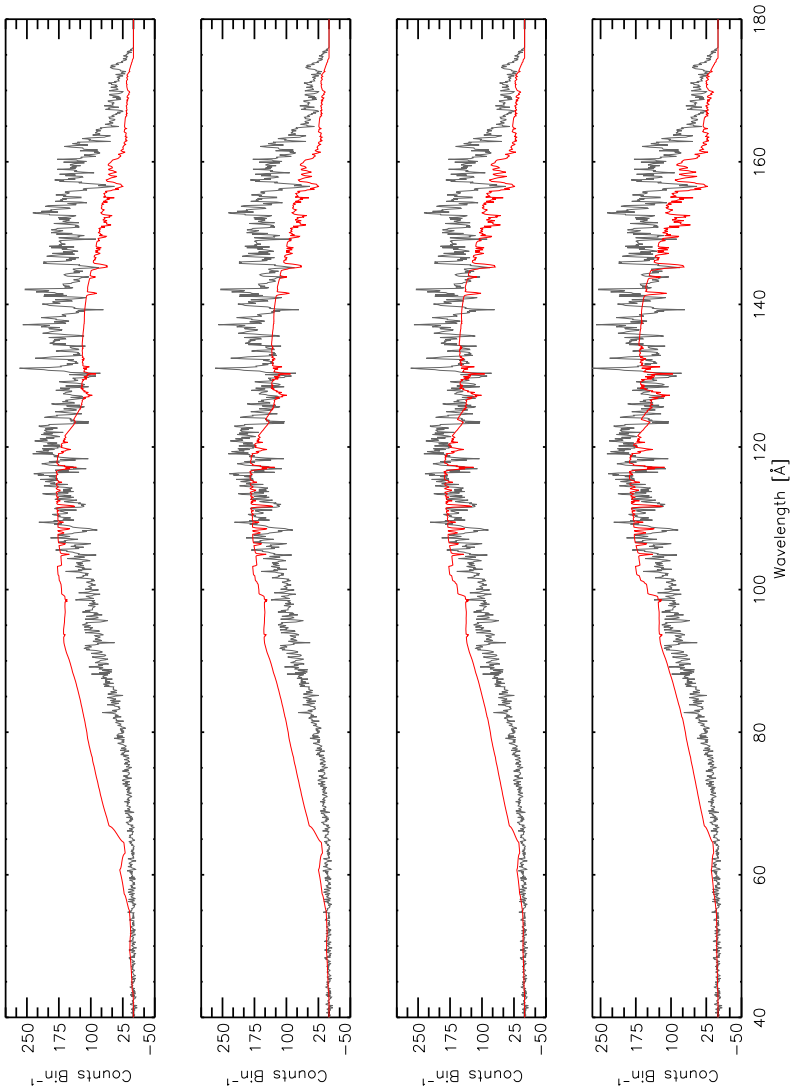


Figure A.7: *Chandra* observation (thin line) with overplotted model spectra (thick line) calculated with $T_{\text{eff}} = 52000\text{K}$ and different $\log g$, from top to bottom: $\log g = 7.9, 7.6, 7.3, 7.1$. The smallest $\log g$ provides the best fit.

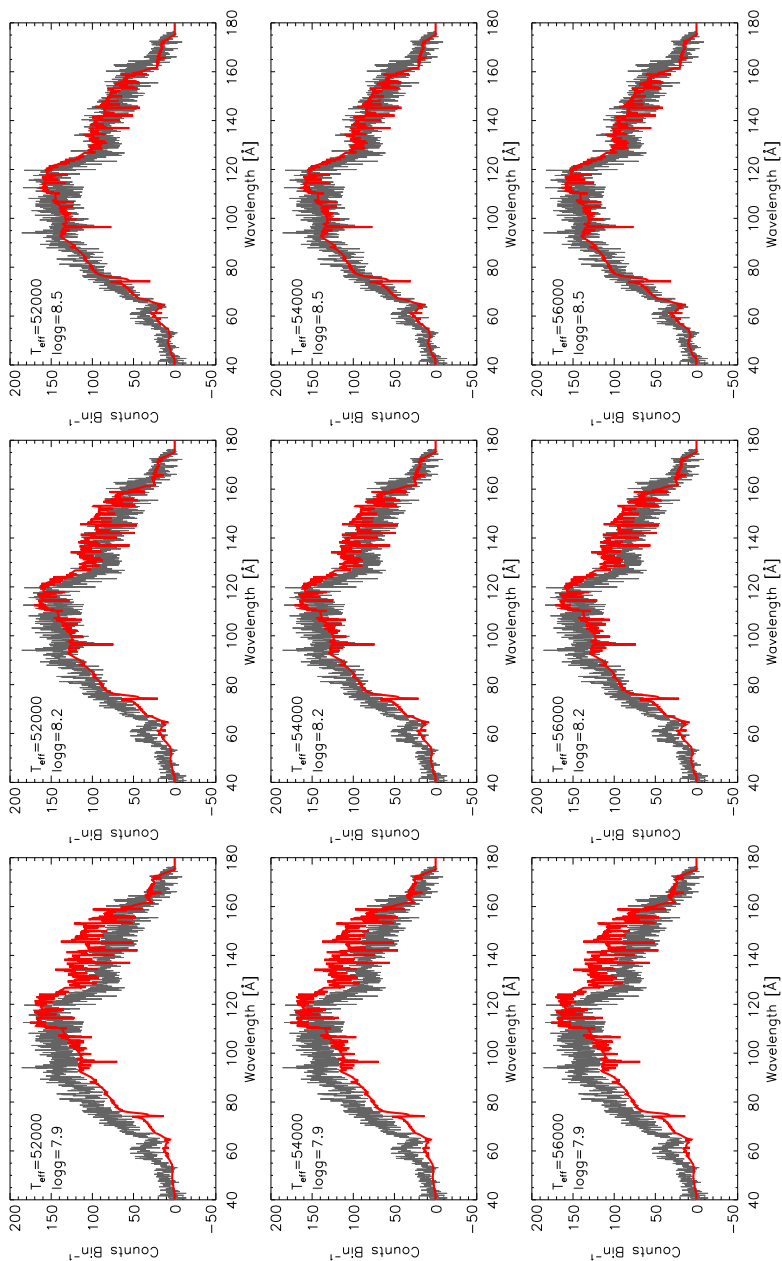


Figure A.8: *Chandra* spectra of LB 1919 (thin lines) with overplotted homogeneous models calculated with H, C, O, Si, P, and S for $T_{\text{eff}} = 52\text{--}56$ kK and $\log g = 7.9\text{--}8.5$ (thick lines).

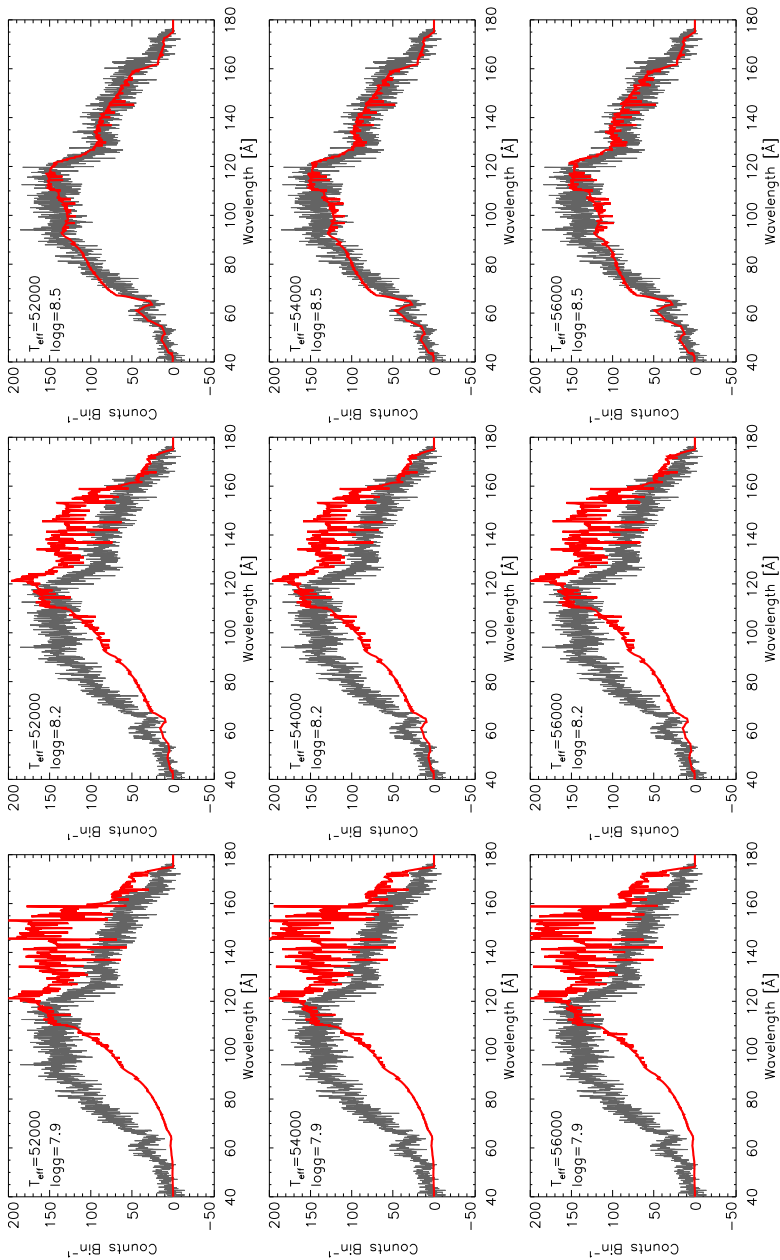


Figure A.9: *Chandra* spectra of LB 1919 (thin lines) with overplotted stratified models calculated with H, C, O, Si, P, and S for $T_{\text{eff}} = 52\text{--}56\text{ kK}$ and $\log g = 7.9\text{--}8.5$ (thick lines).

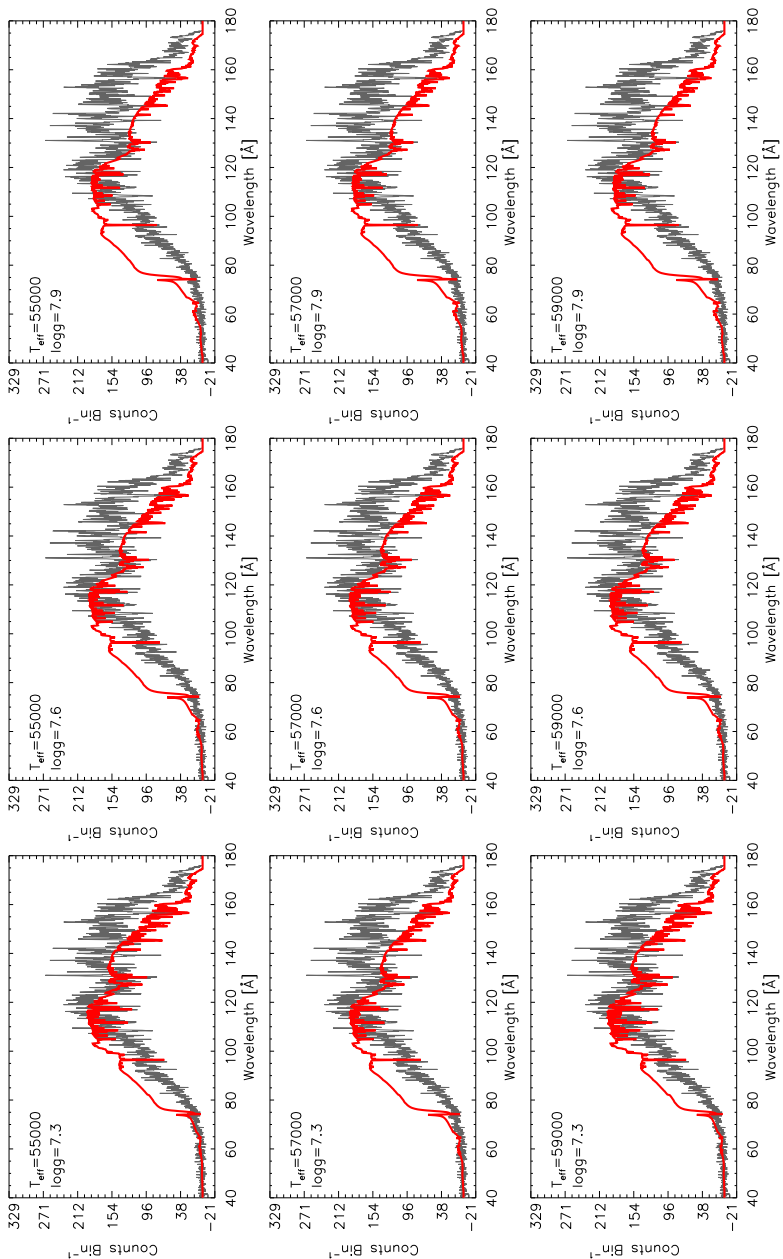


Figure A.10: *Chandra* spectra of GD 246 (thin lines) with overplotted homogeneous models calculated with H, C, O, Si, P, S, Ge, and Fe for $T_{\text{eff}}=55\text{--}59\text{ kK}$ and $\log g=7.3\text{--}7.9$ (thick lines).

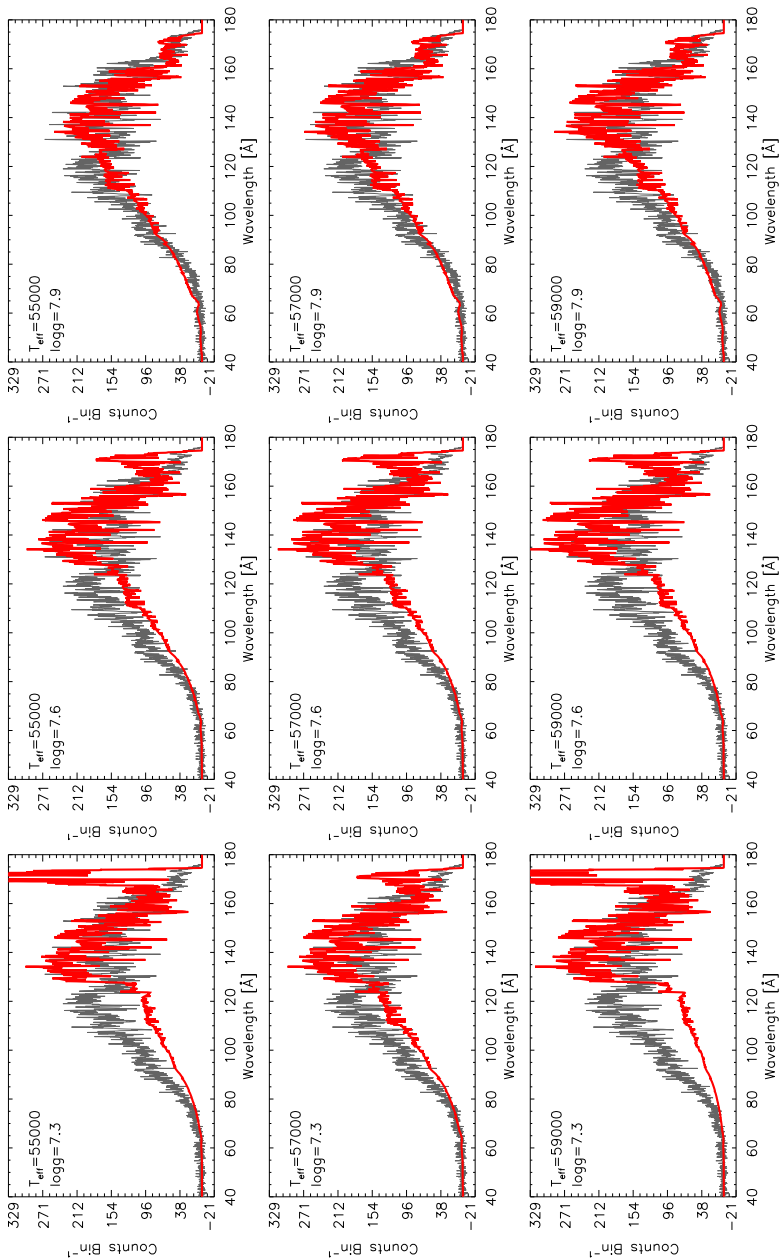


Figure A.11: *Chandra* spectra of GD246 (thin lines) with overplotted stratified models calculated with H, C, O, Si, P, S, Ge, and Fe for $T_{\text{eff}}=55\text{--}59$ kK and $\log g=7.3\text{--}7.9$ (thick lines).

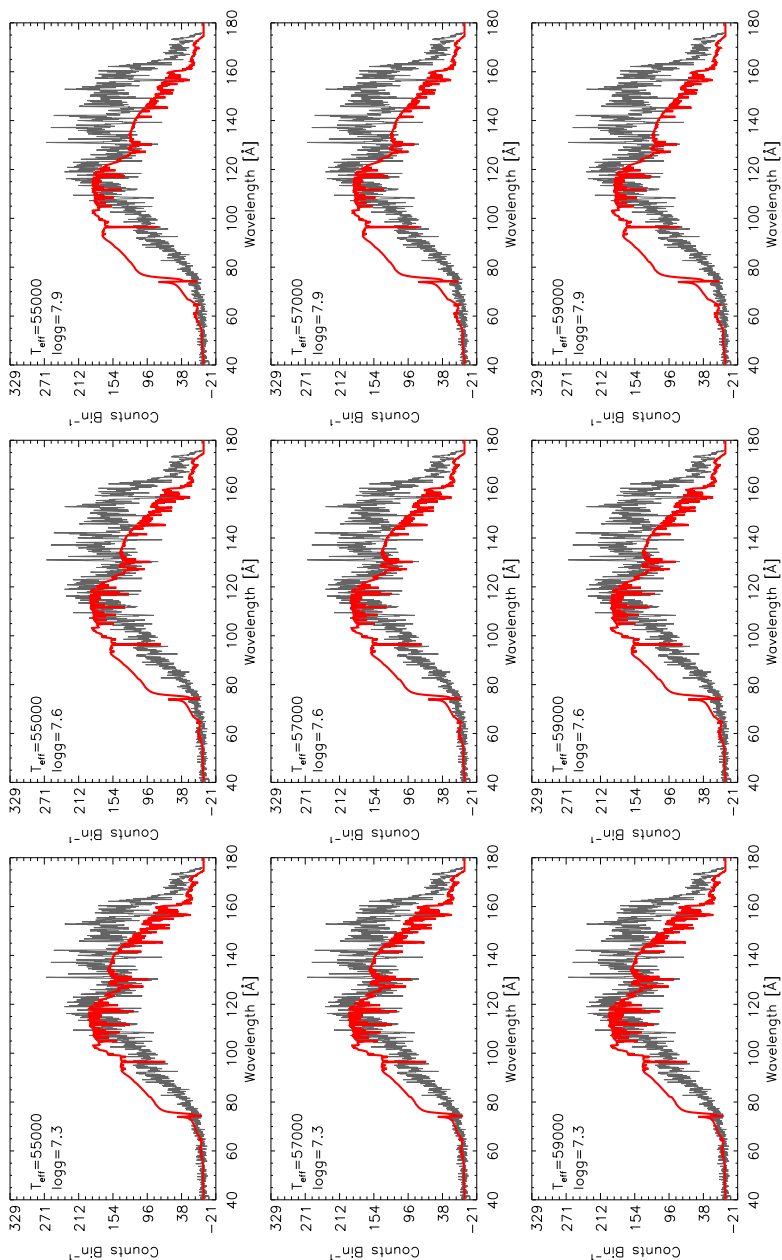


Figure A.12: *Chandra* spectra of GD 246 (thin lines) with overplotted homogeneous models calculated with H, C, O, Si, P, S, Ge, Fe, and Ni for $T_{\text{eff}}=55\text{--}59$ kK and $\log g=7.3\text{--}7.9$ (thick lines).

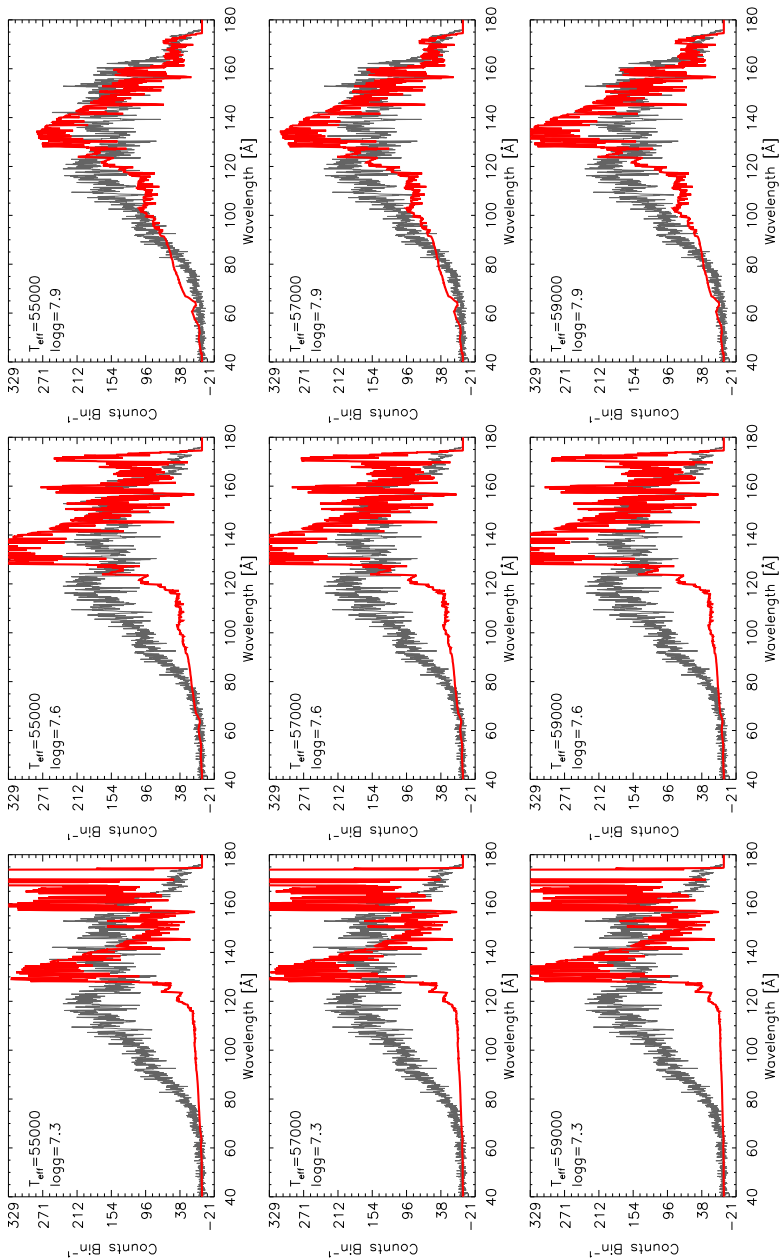


Figure A.13: *Chandra* spectra of GD246 (thin lines) with overplotted stratified models calculated with H, C, O, Si, P, S, Ge, Fe, and Ni for $T_{\text{eff}}=55\text{--}59\text{ kK}$ and $\log g=7.3\text{--}7.9$ (thick lines).

APPENDIX B

***FUSE* plots**

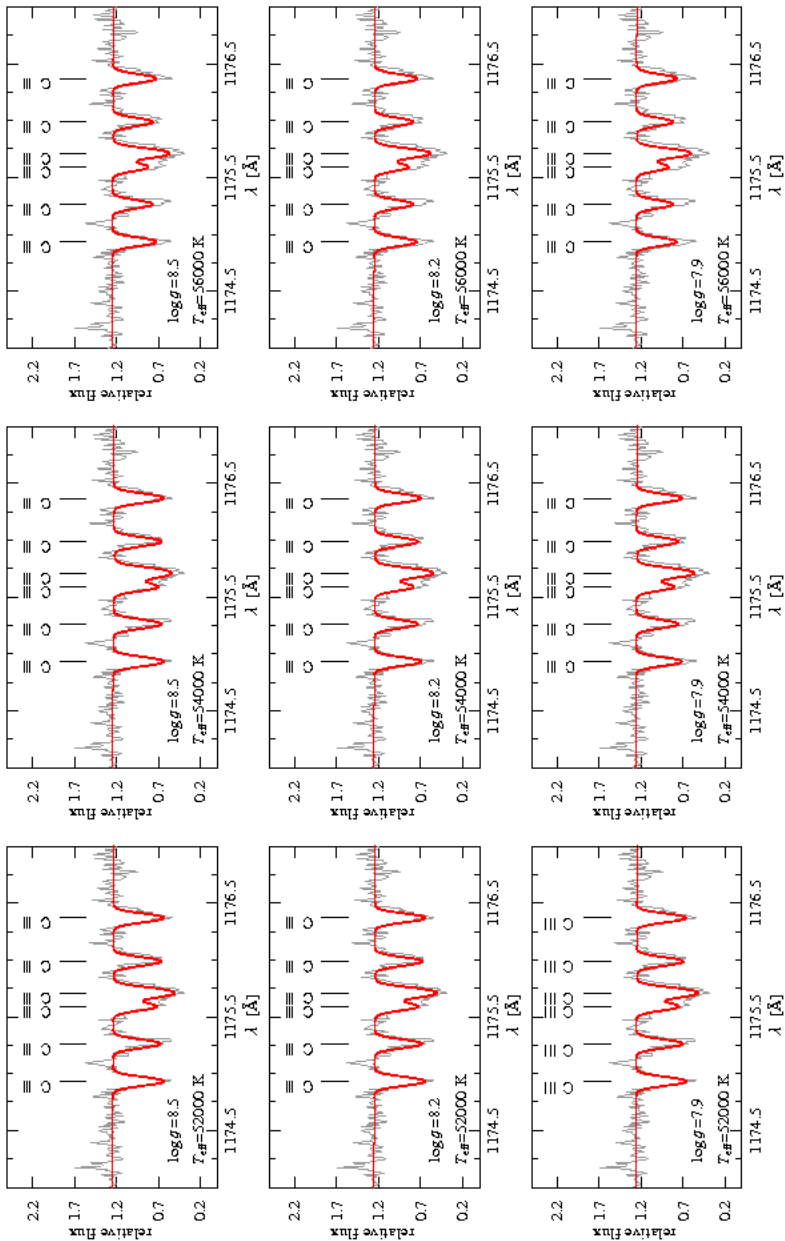


Figure B.1: C III triplet in the *FUSE* spectra of LB 1919 (thin lines) with overplotted homogeneous models (thick lines).

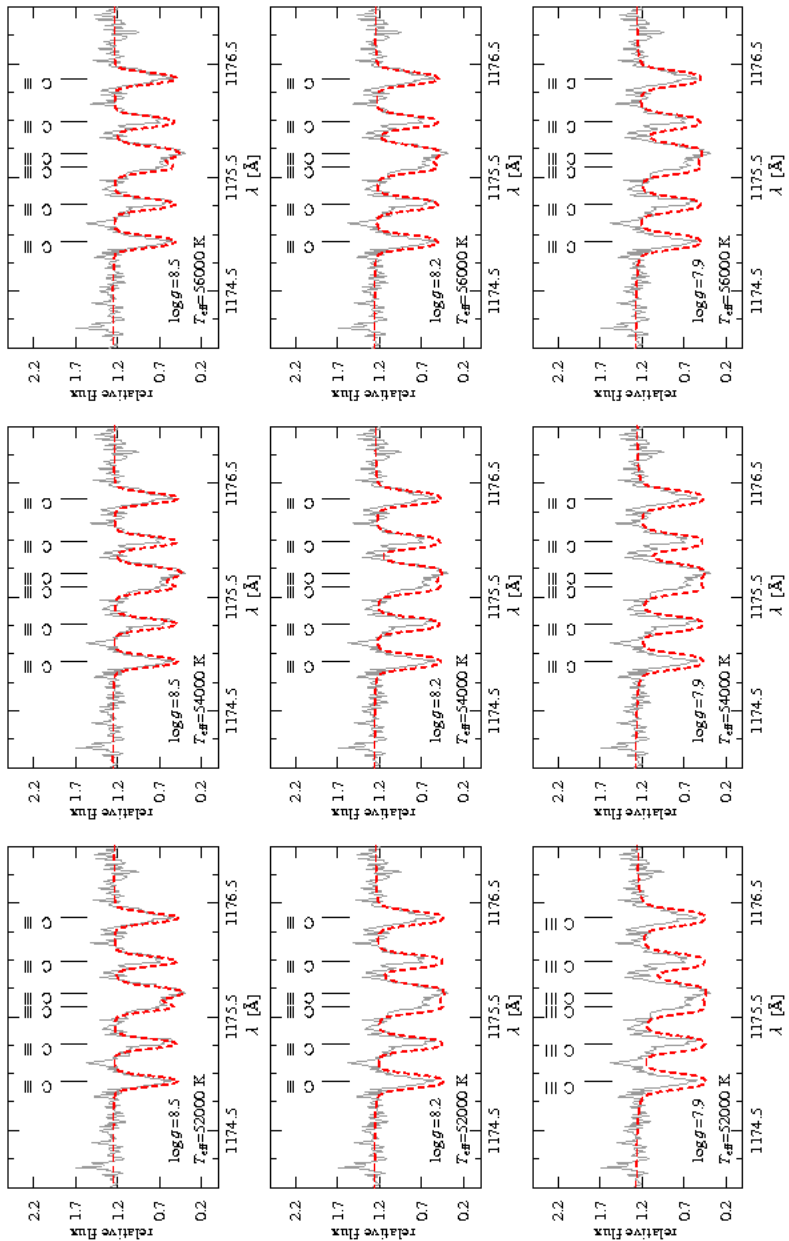


Figure B.2: C III triplet in the *FUSE* spectra of LB 1919 (thin lines) with overlotted stratified models (dashed lines).

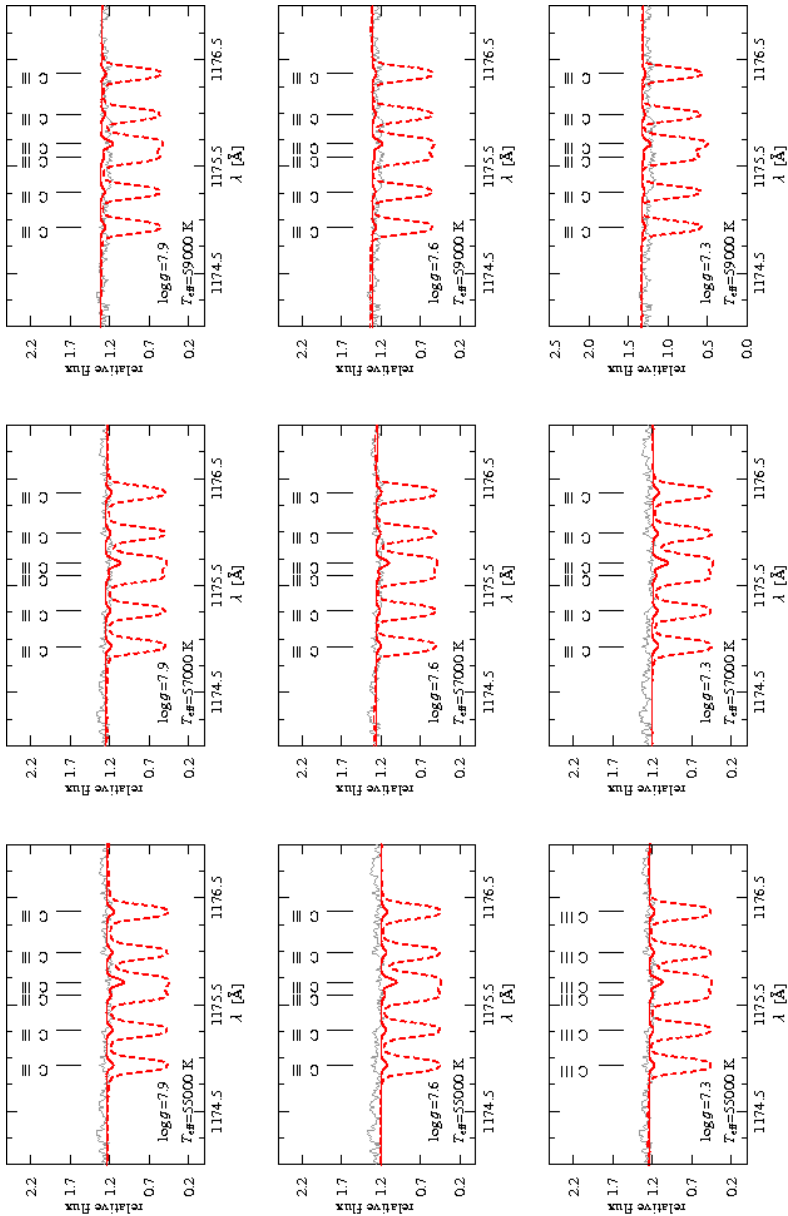


Figure B.3: C III triplet in the *FUSE* spectra of GD 246 (thin lines) with overplotted homogeneous (thick line) and stratified models (dashed lines).

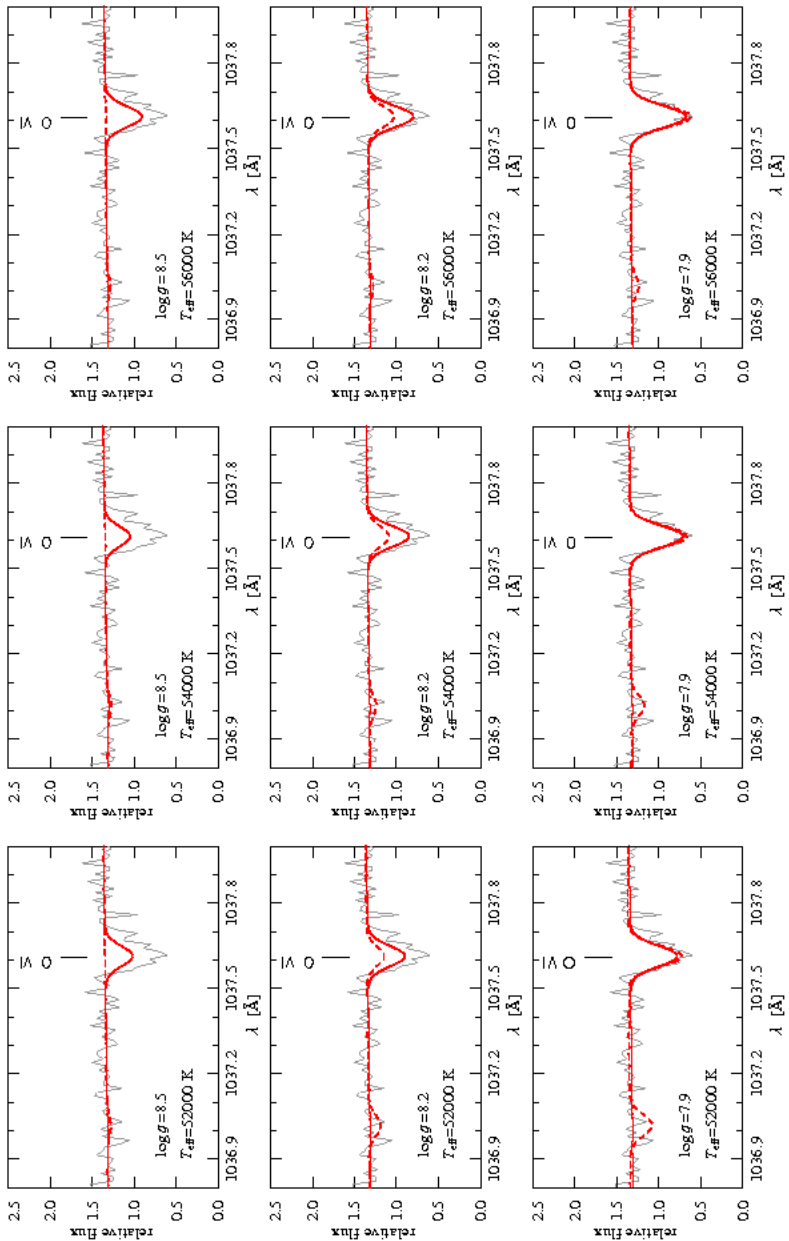


Figure B.4: O VI line in the *FUSE* spectra of LB 1919 (thin lines) with overplotted homogeneous (thick line) and stratified models (dashed lines).

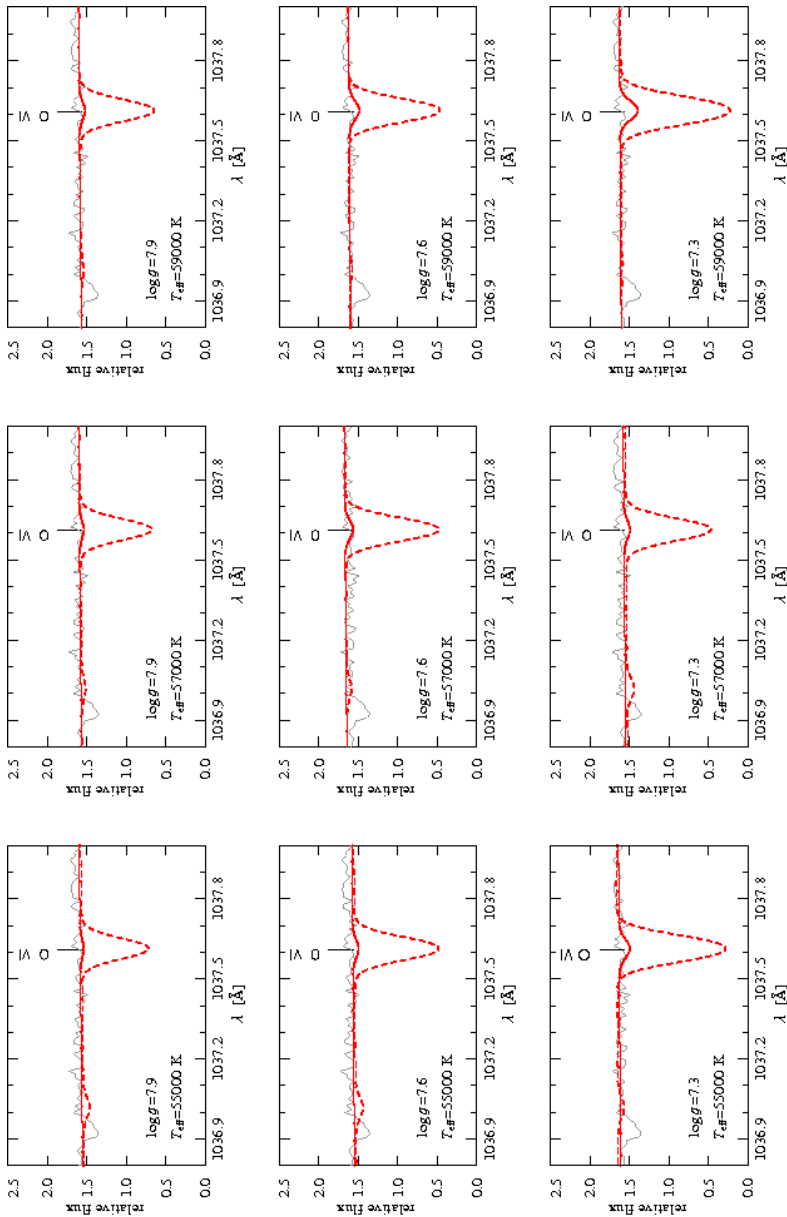


Figure B.5: O VI line in the *FUSE* spectra of GD 246 (thin lines) with overplotted homogeneous (thick line) and stratified models (dashed lines).

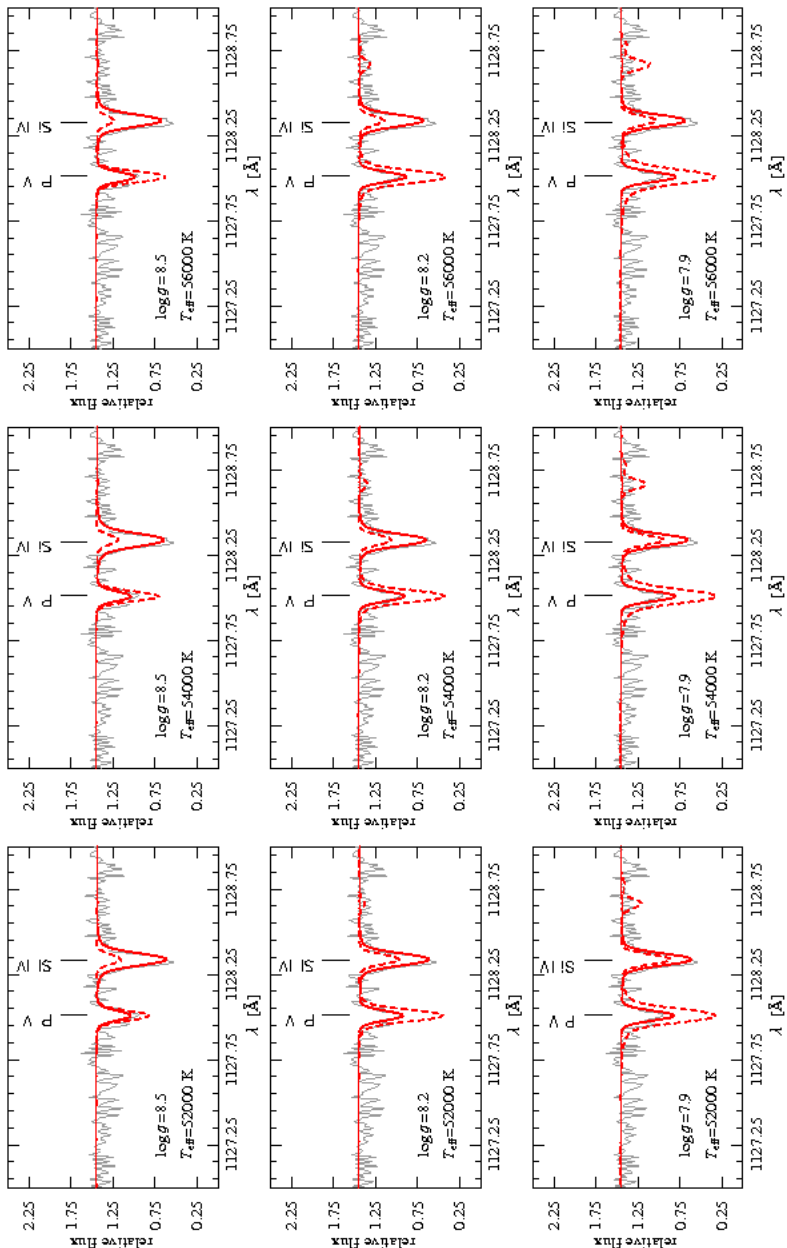


Figure B.6: P V and Si IV line in the *FUSE* spectra of LB 1919 (thin lines) with overplotted homogeneous (thick line) and stratified models (dashed lines).

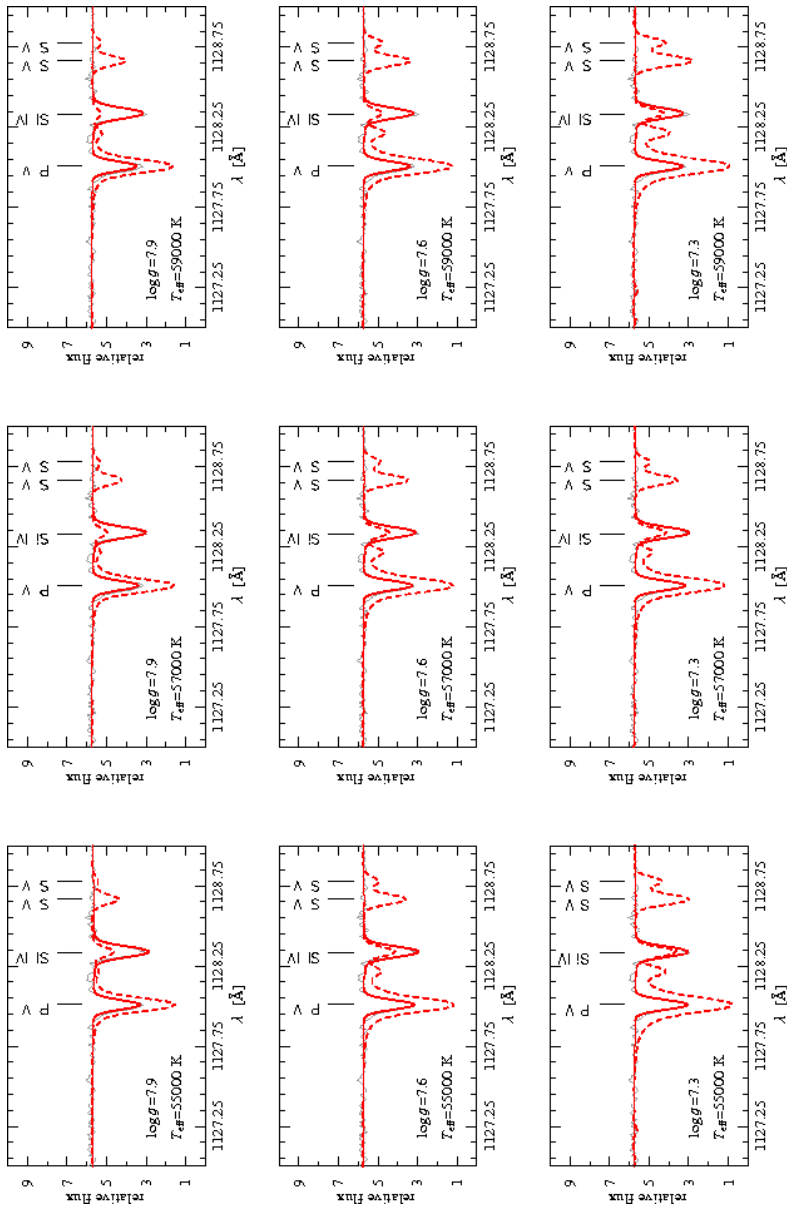


Figure B.7: P V and Si IV line in the *FUSE* spectra of GD 246 (thin lines) with overlotted homogeneous (thick line) and stratified models (dashed lines).

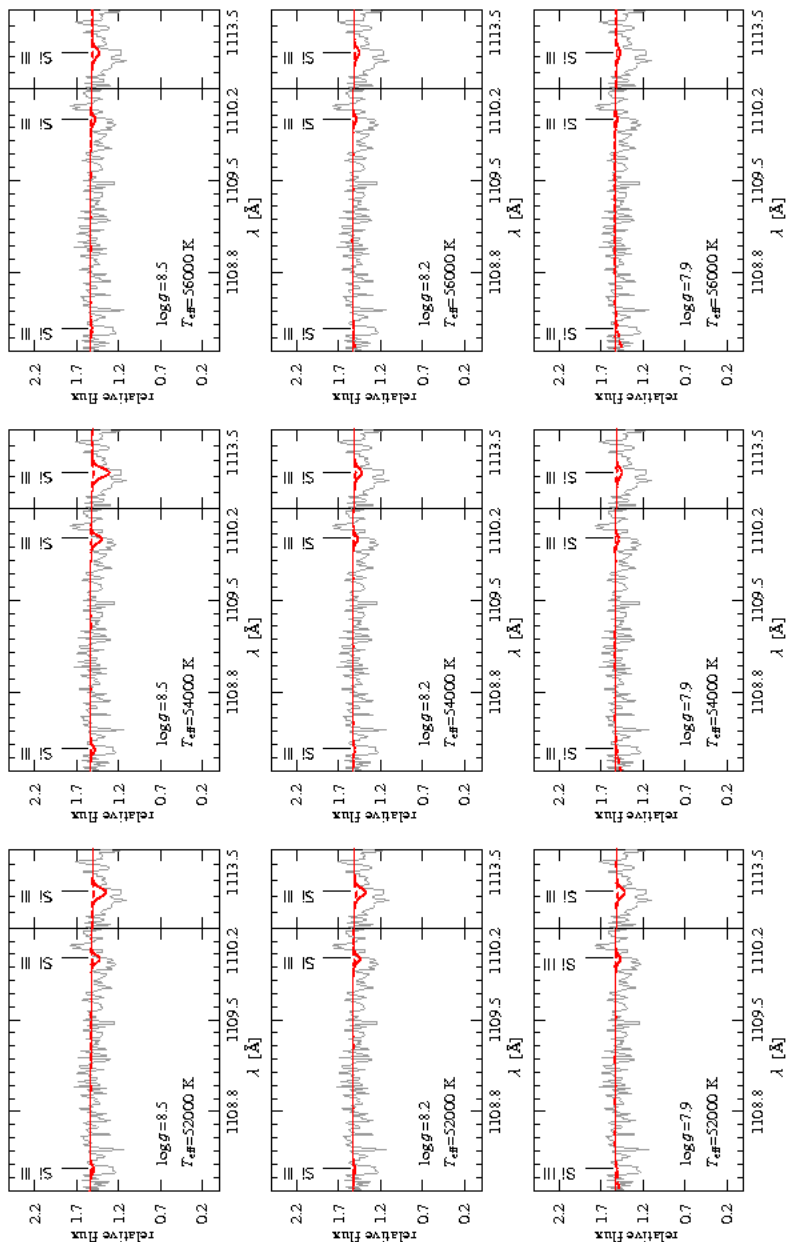


Figure B.8: Si III triplet in the *FUSE* spectra of LB 1919 (thin lines) with overplotted homogeneous (thick line) and stratified models (dashed lines).

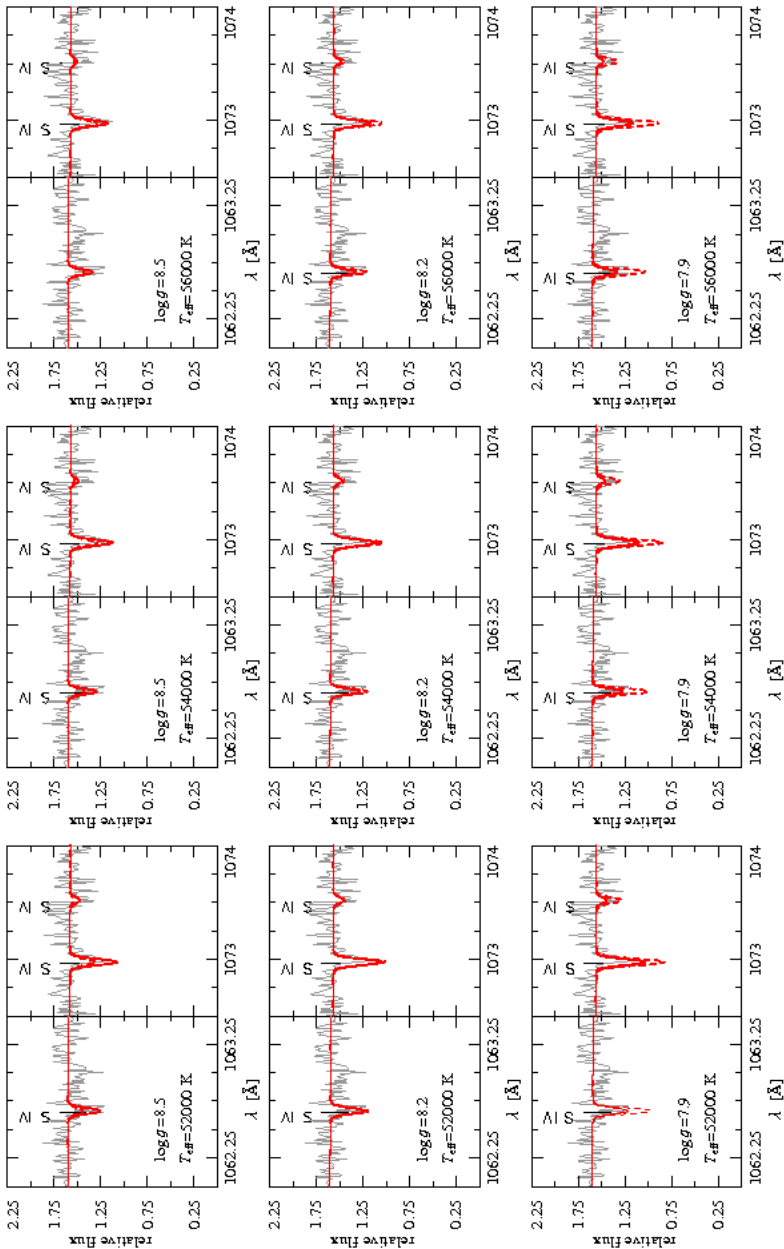


Figure B.9: S IV triplet in the *FUSE* spectra of LB 1919 (thin lines) with overplotted homogeneous (thick line) and stratified models (dashed lines).

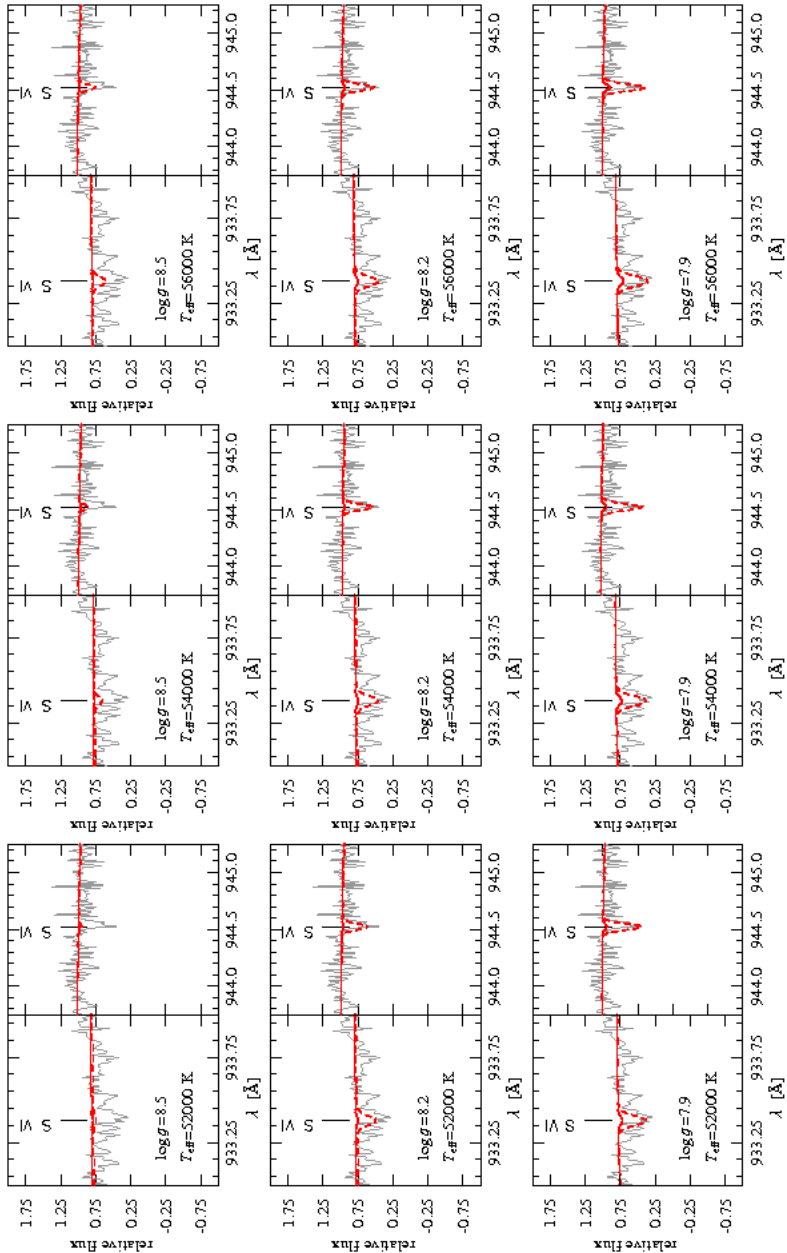


Figure B.10: S VI doublet in the *FUSE* spectra of LB 1919 (thin lines) with overlotted homogeneous (thick line) and stratified models (dashed lines).

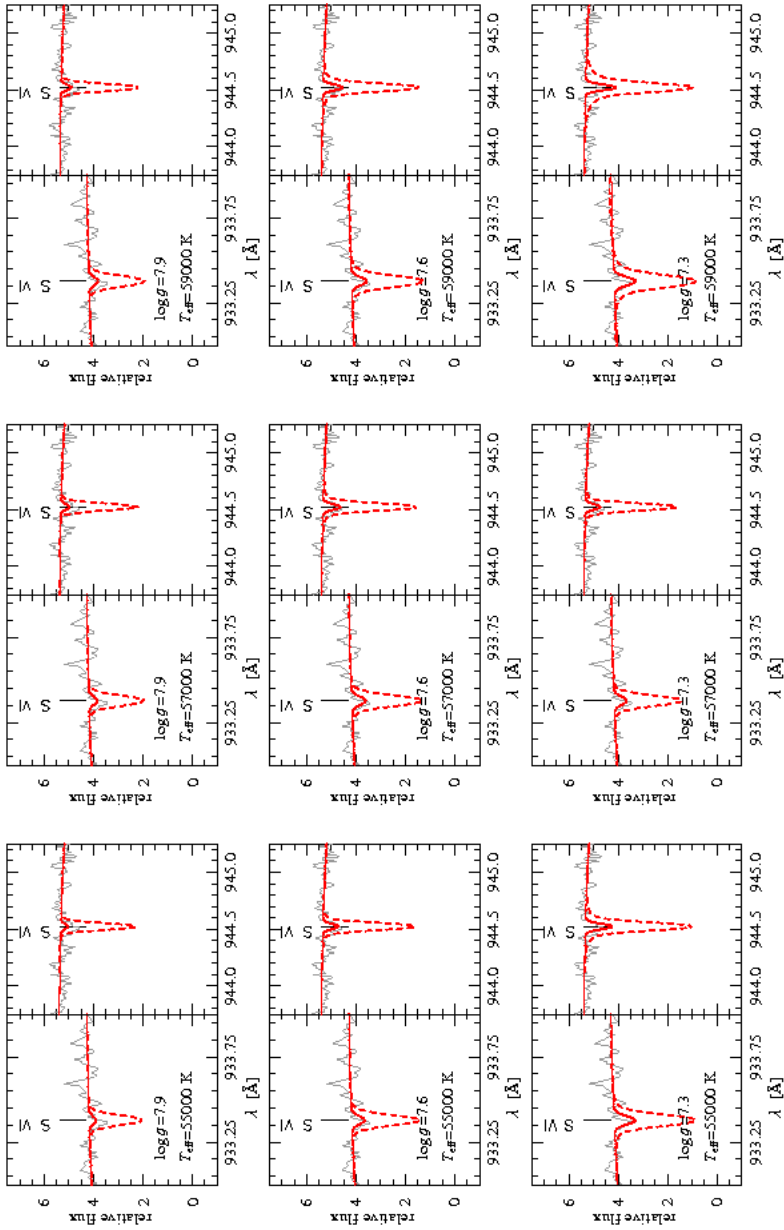


Figure B.11: S VI doublet in the *FUSE* spectra of GD 246 (thin lines) with overplotted homogeneous (thick line) and stratified models (dashed lines).

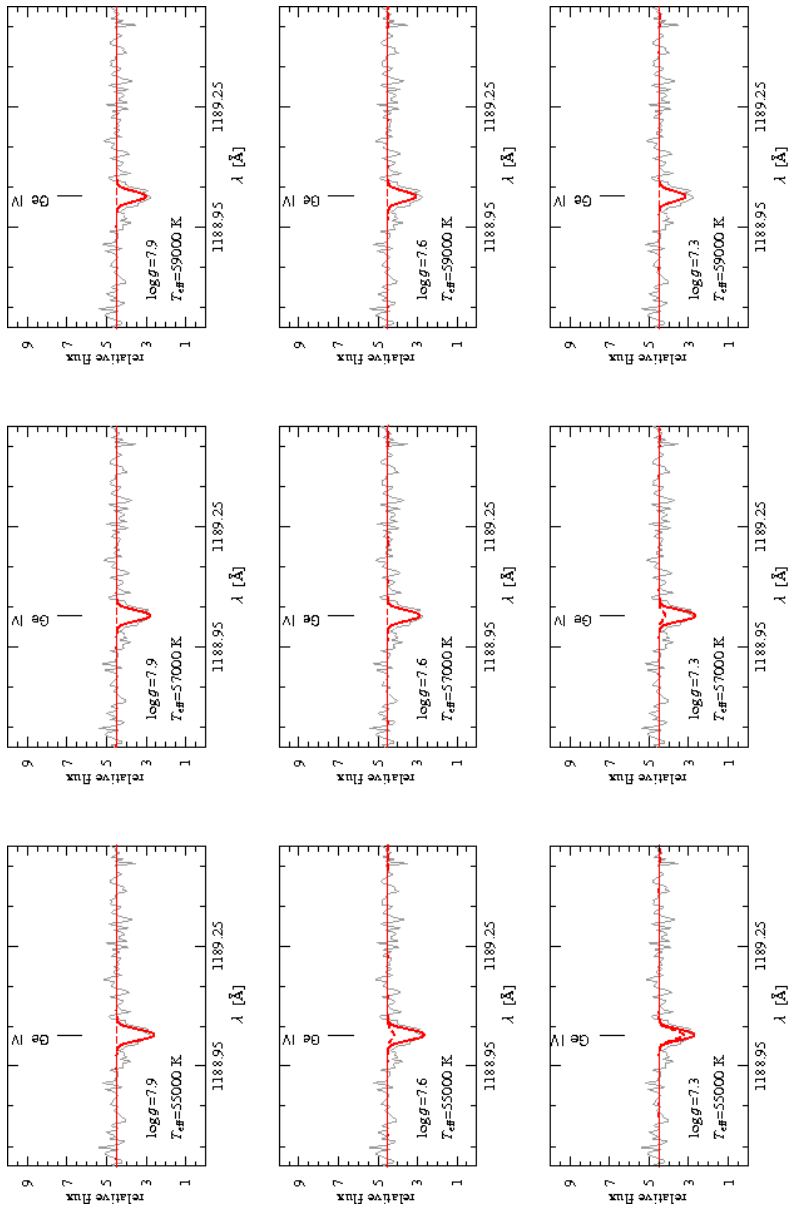


Figure B.12: Ge IV line in the *HST* spectra of GD 246 (thin lines) with overlapped homogeneous (thick line) and stratified models (dashed lines).

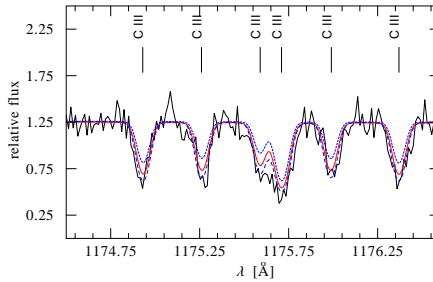


Figure B.13: C III triplet in the *FUSE* spectrum of LB 1919 (thin line). Overplotted homogeneous models are calculated with $T_{\text{eff}} = 54000\text{K}$, $\log g = 8.20$ and varying abundances: $\text{C}/\text{H} = 2.5 \cdot 10^{-7}$ (dotted line), $\text{C}/\text{H} = 4.63 \cdot 10^{-7}$ (thick line), and $\text{C}/\text{H} = 7.5 \cdot 10^{-7}$ (dashed line).

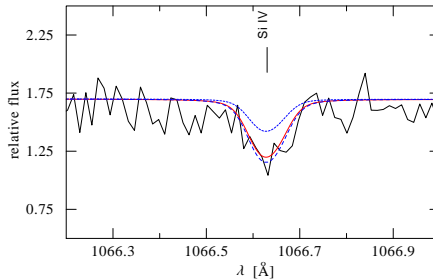


Figure B.14: Si IV line in the *FUSE* spectrum of LB 1919 (thin line). Overplotted homogeneous models are calculated with $T_{\text{eff}} = 54000\text{K}$, $\log g = 8.20$ and varying abundances: $\text{Si}/\text{H} = 5 \cdot 10^{-8}$ (dotted line), $\text{Si}/\text{H} = 1.2 \cdot 10^{-7}$ (thick line), and $\text{Si}/\text{H} = 1.4 \cdot 10^{-7}$ (dashed line).

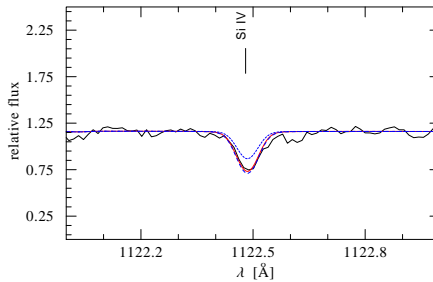


Figure B.15: Si IV line in the *FUSE* spectrum of GD 246 (thin line). Overplotted homogeneous models are calculated with $T_{\text{eff}} = 57000\text{K}$, $\log g = 7.60$ and varying abundances: $\text{Si}/\text{H} = 5 \cdot 10^{-8}$ (dotted line), $\text{Si}/\text{H} = 1.2 \cdot 10^{-7}$ (thick line), and $\text{Si}/\text{H} = 1.4 \cdot 10^{-7}$ (dashed line).

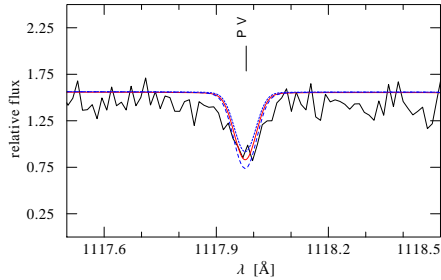


Figure B.16: PV line in the *FUSE* spectrum of LB 1919 (thin line). Overplotted homogeneous models are calculated with $T_{\text{eff}} = 54000\text{K}$, $\log g = 8.20$ and varying abundances: $\text{P}/\text{H} = 2 \cdot 10^{-9}$ (dotted line), $\text{P}/\text{H} = 3 \cdot 10^{-9}$ (thick line), and $\text{P}/\text{H} = 5 \cdot 10^{-9}$ (dashed line).

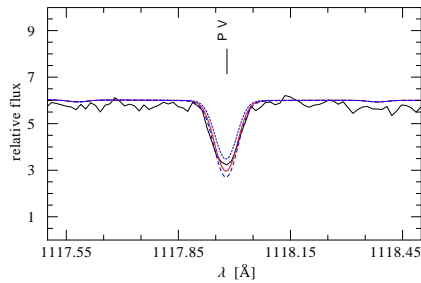


Figure B.17: PV line in the *FUSE* spectrum of GD 246 (thin line). Overplotted homogeneous models are calculated with $T_{\text{eff}} = 57000\text{K}$, $\log g = 7.60$ and varying abundances: $\text{P}/\text{H} = 2 \cdot 10^{-9}$ (dotted line), $\text{P}/\text{H} = 4 \cdot 10^{-9}$ (thick line), and $\text{P}/\text{H} = 6 \cdot 10^{-9}$ (dashed line).

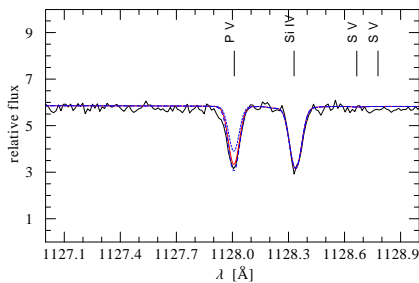


Figure B.18: PV line in the *FUSE* spectrum of GD 246 (thin line). Overplotted homogeneous models are calculated with $T_{\text{eff}} = 57000\text{K}$, $\log g = 7.60$ and varying abundances: $\text{P}/\text{H} = 2 \cdot 10^{-9}$ (dotted line), $\text{P}/\text{H} = 4 \cdot 10^{-9}$ (thick line), and $\text{P}/\text{H} = 6 \cdot 10^{-9}$ (dashed line).

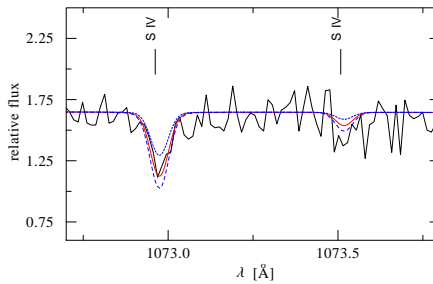


Figure B.19: Two components of the S IV triplet in the *FUSE* spectrum of LB 1919 (thin line). Overplotted homogeneous models are calculated with $T_{\text{eff}} = 52000\text{K}$, $\log g = 8.50$ and varying abundances: $S/H = 5 \cdot 10^{-8}$ (dotted line), $S/H = 1 \cdot 10^{-7}$ (thick line), and $S/H = 1.5 \cdot 10^{-7}$ (dashed line).

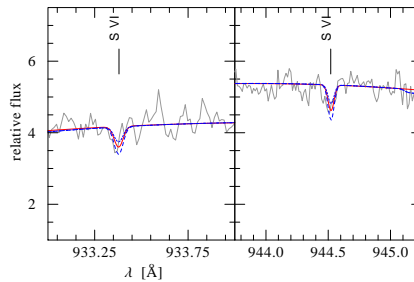


Figure B.20: S VI line in the *FUSE* spectrum of GD 246 (thin line). Overplotted homogeneous models are calculated with $T_{\text{eff}} = 57000\text{K}$, $\log g = 7.60$ and varying abundances: $S/H = 3 \cdot 10^{-9}$ (dotted line), $S/H = 5 \cdot 10^{-9}$ (thick line), and $S/H = 7 \cdot 10^{-9}$ (dashed line).

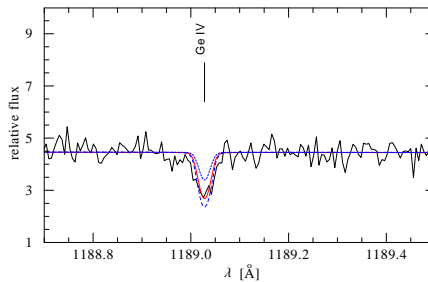


Figure B.21: Ge IV line in the *FUSE* spectrum of GD 246 (thin line). Overplotted homogeneous models are calculated with $T_{\text{eff}} = 55000\text{K}$, $\log g = 7.30$ and varying abundances: $\text{Ge}/H = 5 \cdot 10^{-9}$ (dotted line), $\text{Ge}/H = 2 \cdot 10^{-9}$ (thick line), and $\text{Ge}/H = 8 \cdot 10^{-9}$ (dashed line).

APPENDIX C

***UVES* plots**

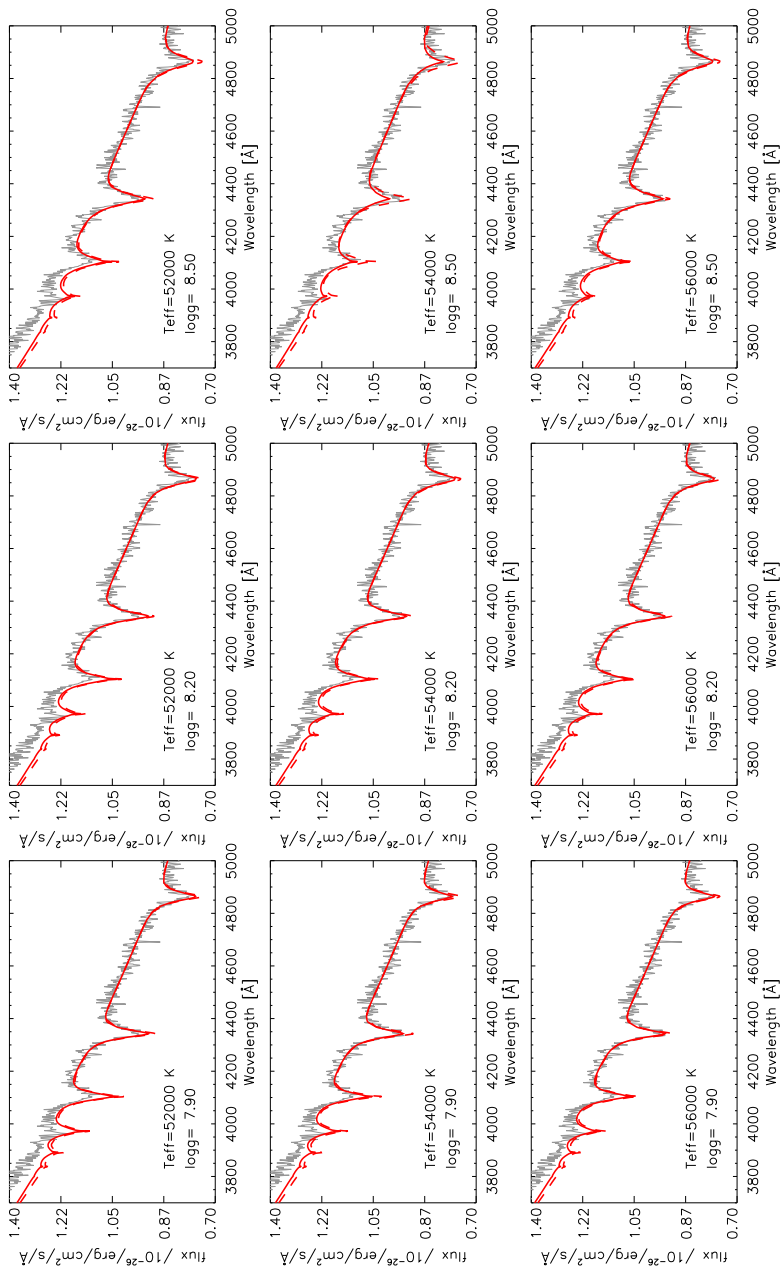


Figure C.1: Balmer lines in the UVES spectrum of LB 1919 (thin line) with overplotted model spectra calculated with H, C, O, Si, P, and S (thick line) and pure H models (dotted line).

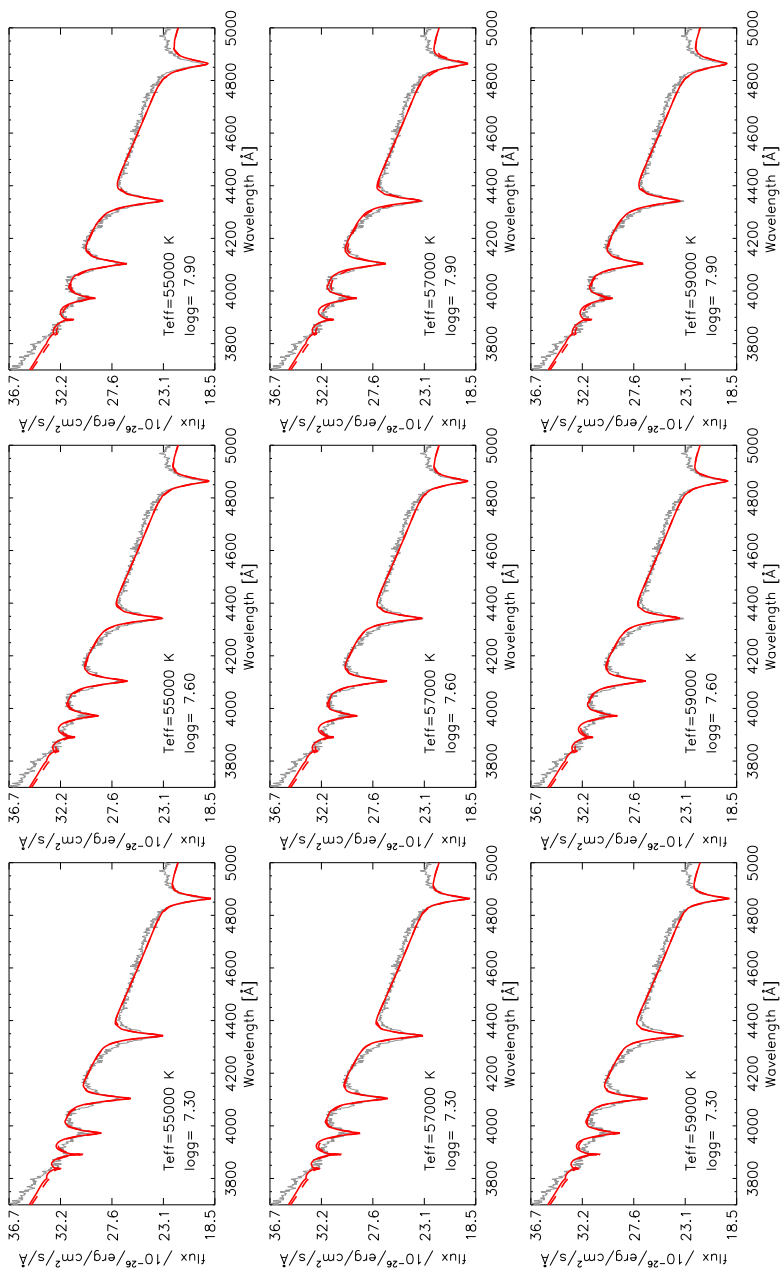


Figure C.2: Balmer lines in the UVES spectrum of GD246 (thin line) with overplotted model spectra calculated with H, C, O, Si, P, S, Ge, Fe, and Ni (thick line) and pure H models (dotted line).

APPENDIX D

Model atoms plots

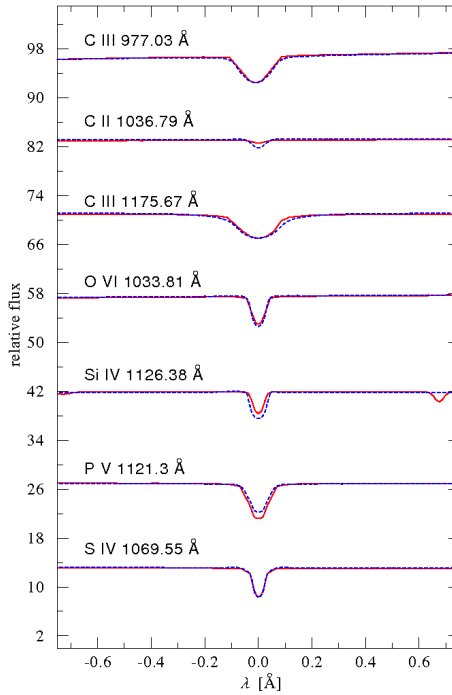


Figure D.1: Effect of big model atoms used in the diffusion calculations on the line profiles of C, O, Si, P, and S in a model atmosphere with $T_{\text{eff}} = 54000\text{K}$ and $\log g = 8.2$. Models are calculated with H and all elements and small model atoms (thick line) and H plus one single element and big model atoms (dotted line).

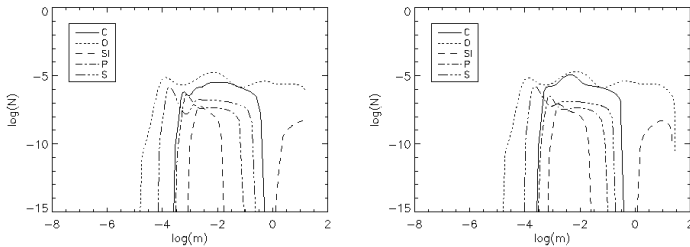


Figure D.2: Comparison between abundance profile of models calculated with different elements, small model atoms, and $T_{\text{eff}} = 54000\text{K}$, $\log g = 8.2$. Left: Element abundances in a model with H, C, O, Si, P, and S. Right: Element abundances in a model computed with the element and H.

Acknowledgments

I would like to thank Klaus Werner for his supervision of this thesis and guidance in any aspect in the last three years. He always offered advice and support to help me with my problems in a friendly and encouraging way.

My thanks go to the stellar atmosphere group at the IAAT. Especially I thank Thorsten Nagel who was always there to discuss any kind of issues. His value for the institute is impossible even to estimate. I thank Thomas Rauch for not hesitating to aid me with all sorts of special requests and TMAP related questions.

I thank the rest of the IAAT, especially all the generous drivers who tolerated my presences in their cars on the way to the *Mensa* and back, the astro-soccer players, and all people who provided cake on various occasions. I also thank Michael Martin for never ending \TeX support.

I am indebted to my office mates Daniel, Dima, and Marc for sharing hot summers and cold winters in limited space and for providing a comforting atmosphere throughout the year.

I thank Sonja Schuh who never tired helping me promptly despite her busy schedule.

I would like to express my gratitudes to my friends and my changing roommates over the years who established a homy environment that helped to relax and unload. In this context I thank my parents, my brother, and my sister-in-law for being the greatest family in the history of mankind (no offense to other families).

Finally, I greatly thank Kristina A. Vaklinova for proof-reading this thesis, for *gemütliche Abende*, and for simply being the wonderful person she is. Ti si gotina, istina e!

Curriculum vitae

- 19.06.1982 born in Marburg, Germany
08.1988 – 06.1992 Elementary school (Grundschule) Kassel
08.1992 – 05.2001 High school (Gymnasium) Kassel
06.2001 High school graduation (Abitur)
08.2001 – 05.2002 Civilian service
10.2002 – 07.2007 Georg August university Göttingen
major: physics
07.2006 – 06.2007 Diploma thesis: “Simulation von Beobachtungen der Milchstraße für den Multi Unit Spectroscopic Explorer der Europäischen Südsternwarte” under the supervision of S. Dreizler at the Georg August Universität Göttingen; Institut für Astrophysik
07.2007 Diploma
08.2007 – 07.2010 Scientific employee, IAAT Tübingen
08.2007 – 07.2010 Preparation of Ph.D. thesis entitled “X-ray spectroscopy of hot white dwarfs” under the supervision of Prof. K. Werner at the Institute for Astronomy and Astrophysics, Tübingen

My academic teachers have been the professors and lecturers:

Applied Physics: H. Hofsäss, R. Ulbrich, A. Tilgner, K. Bahr, A. Quadt,
H.C. Freyhardt, K. Ronning, G. Kaufmann

Astronomy and Astrophysics: S. Dreizler, W. Kollatschny, B. Ziegler, K. Werner
Chemistry: H. Roesky

Experimental Physics: K. Winzer, U. Parlitz, R. Kirchheim

Mathematics: L. Smith, T. Schick

Theoretical Physics: D. Buchholz, K.H. Rehren, G.C. Hegerfeldt

Lebenslauf

- 19.06.1982 geboren in Marburg
08.1988 – 06.1992 Grundschule Kassel
08.1992 – 07.1998 Mittelstufe (Gesamtschule) Kassel
08.1998 – 05.2001 Oberstufe (Gymnasium) Kassel
06.2001 Abitur
08.2001 – 05.2002 Zivildienst
10.2002 – 07.2007 Georg August Universität Göttingen
Abschluss: Physik
07.2006 – 06.2007 Diplomarbeit: “Simulation von Beobachtungen der Milchstraße für den Multi Unit Spectroscopic Explorer der Europäischen Südsternwarte” betreut von S. Dreizler an der Georg August Universität Göttingen; Institut für Astrophysik
07.2007 Diplom
08.2007 – 07.2010 Wissenschaftlicher Angestellter, IAAT Tübingen
08.2007 – 07.2010 Anfertigung der Dissertation “X-ray spectroscopy of hot white dwarfs” betreut von Prof. K. Werner am Institut für Astronomie und Astrophysik, Tübingen

Meine akademischen Lehrer waren die Professoren und Dozenten:

Angewandte Physik: H. Hofsäss, R. Ulbrich, A. Tilgner, K. Bahr, A. Quadt,
H.C. Freyhardt, K. Ronning, G. Kaufmann

Astronomie und Astrophysik: S. Dreizler, W. Kollatschny, B. Ziegler, K. Werner
Chemie: H. Roesky

Experimentalphysik: K. Winzer, U. Parlitz, R. Kirchheim

Mathematik: L. Smith, T. Schick

Theoretische Physik: D. Buchholz, K.H. Rehren, G.C. Hegerfeldt